Correlation functions and fidelity decay in chaotic systems

Dissertation

Presented in Partial Fulfillment
of the Requirements for the Degree of

Doctor of Natural Sciences
(Dr. rer. nat.)

Submitted to the Faculty of Physics
Philipps-University Marburg

by

Rudi Schäfer

Marburg/Lahn 2004

Zusammenfassung

In dieser Arbeit werden verschiedene Aspekte des Quantenchaos untersucht. Die Wellengleichung für flache Mikrowellen-Resonatoren ist mathematisch äquivalent zur Schrödingergleichung in der Quantenmechanik. Daher bieten Mikrowellenmessungen einen experimentellen Zugang zum Quantenchaos. Die Experimente werden mit Hilfe der Streutheorie beschrieben, um die Ankopplung der Antennen, sowie die Dissipation in den Billardwänden zu berücksichtigen.

Im ersten Teil wird die Streumatrix verschiedener Mikrowellen-Resonatoren im Bereich überlappender Resonanzen analysiert. Sowohl die Autokorrelationsfunktionen der selben, als auch die Kreuzkorrelationsfunktionen verschiedener S-Matrixelemente zeigen charakteristische Unterschiede zwischen klassisch regulären und chaotischen Systemen. Im Einklang mit der Literatur zeigen die Kreuzkorrelationen diesen Unterschied deutlicher. Die Absorption in den Resonatorwänden wird dabei mit unendlich vielen schwach gekoppelten Kanälen modelliert.

Im zweiten Teil geht es um die Stabilität der Zeitentwicklung in der Quantenmechanik. Die Fidelity-Amplitude ist dabei eine Standardgröße zur Charakterisierung der Störempfindlichkeit eines Quantensystems. Sie ist definiert als Überlapp-Integral der gestörten und ungestörten Zeitentwicklung des selben Anfangszustands. Exakte theoretische Ergebnisse im Rahmen der Zufallsmatrix-Theorie werden mit numerischen Simulationen und den linear-response Ergebnissen verglichen. Für starke Störungen bildet sich ein lokales Maximum der Fidelity-Amplitude bei der Heisenberg-Zeit aus. Eine intuitive Erklärung für dieses Phänomen bietet die Analogie zum Debye-Waller-Faktor aus der Festkörperphysik. Desweiteren werden im dritten Teil der Arbeit experimentelle Ergebnisse zur Fidelity-Amplitude vorgestellt für zwei Mikrowellen-Resonatoren mit klassisch chaotischer Dynamik. Die Störung wurde dabei durch das Verschieben einer Wand bewerkstelligt. Die Ergebnisse lassen sich im Rahmen der linear-response Theorie beschreiben.

Im vierten Teil werden Mikrowellen-Messungen an dielektrischen Quadrupolbillards mit gemischtem Phasenraum vorgestellt. Die interne Dynamik wird mit Hilfe von Husimi-Verteilungen analysiert, während im Außenbereich der Poynting-Vektor das Abstrahlverhalten liefert. Dieses ist bei Quadrupolbillards stark von den Strukturen des klassischen Phasenraums geprägt.

Abstract

In this work several aspects of quantum chaos are studied in the time domain. The wave equation for flat microwave cavities is equivalent to the Schrödinger equation in quantum mechanics. Therefore microwave measurements provide an experimental approach to quantum chaos. The experiments are described in terms of scattering theory, to take the coupling of the antennas to the system as well as the dissipation in the cavity walls into account.

In the first part the scattering matrix of several microwave cavities is analyzed in the regime of overlapping resonances. The difference between regular and chaotic systems can be observed both in the autocorrelation functions of the same S-matrix elements, and in the cross-correlation functions of different S-matrix elements. In accordance with literature, this difference is more pronounced in the cross-correlation functions. To describe the experimental correlation functions, the absorption in the cavity walls is modeled by an infinite number of weak decay channels.

In the second part the focus is shifted to the stability of quantum time-evolution. The fidelity amplitude is a standard benchmark for the stability of a quantum system against a change of the Hamiltonian. It is defined as the overlap of the perturbed and unperturbed time-evolution of the same initial state. Exact theoretical results for a random matrix model are compared with numerical simulations and the linear-response results. For strong perturbations a partial recovery of the fidelity amplitude is found, and an intuitive explanation for this behavior is given in terms of a spectral Debye-Waller factor. Further, in the third part, experimental results for the fidelity amplitude are presented for two microwave cavities with classically chaotic dynamics. The perturbation of the systems is realized by applying small changes to their geometry. The results are well described by the linear-response expression, and the perturbation strength can be related to the change of the geometry of the cavities.

In the fourth part microwave measurements on dielectric quadrupole billiards with mixed phase space are discussed. The internal dynamics is analyzed by means of Husimi distributions, while for the outer region the Poynting vector is determined to obtain the emission pattern. The emission pattern of the quadrupole billiard is strongly influenced by the structures of its mixed phase space.

Contents

List of Figures

Chapter 1

Introduction

In classical mechanics the stability of a system with respect to the initial conditions determines whether we call the dynamics regular or chaotic [Sch84]. For chaotic systems the difference in initial conditions grows exponentially with time, while for regular systems this difference grows much slower, often only linearly with time.

However, completely regular or chaotic systems are only the extreme cases. In general a system can show both regular and chaotic dynamics depending on the initial conditions. In this case the phase space is *mixed*, since it contains both regular and chaotic regions. A trajectory starting near a stable fix-point in phase space will stay in its vicinity for all time, while a trajectory starting in a chaotic part of phase space will cover this chaotic part completely. In a fully chaotic system almost every trajectory (apart from periodic orbits which are of measure zero) will cover the whole phase space - this is called ergodicity.

For the study of regular and chaotic motion one often considers two-dimensional billiard systems, where the motion of a point-like particle is confined by elastic reflection on the billiard walls. The dynamics of these systems is thus completely determined by the shape of the billiard boundary. The study of billiard systems is quite popular, because they are very simple on the one hand, but still complex enough to show all the features of interest.

In the field of quantum chaos, which emerged in the early 1980s, one investigates how these notions of chaotic and regular motion can be transferred to quantum mechanics. This is not straightforward, since the time-dependence

of the Schrödinger equation is linear. Therefore quantum dynamics is always stable against small variations of the initial state [Cas86]. However, there are many statistical quantities of quantum systems that show signatures of whether the dynamics of the corresponding classical system is regular or chaotic. Spectral properties that are often studied include the distribution of the distance between neighboring eigenenergies and the number variance, i. e. the variance of the number of eigenenergies in intervals of a given length. In the statistics of wavefunctions, e. g. the distributions of amplitudes and intensities, one also finds signatures of the underlying classical dynamics of the system.

According to a conjecture by Bohigas, Giannoni and Schmit [Boh84] (BGS-conjecture) the statistical properties of quantum systems with chaotic classical dynamics can be described by random matrix theory (RMT), which has been developed in the 1950s and 60s by Wigner, Dyson, Mehta and others to describe the statistical properties of the spectra of complex nuclei [Por65].

The basic idea of RMT is that the statistical properties of complex systems are universal and solely determined by the symmetries of the system [Meh67]. The elements of the considered matrix ensembles are Gaussian distributed and uncorrelated. Three universality classes of chaotic systems are distinguished: The Gaussian orthogonal ensemble (GOE) describes time-reversal invariant systems without spin-interactions; its matrices are real symmetric. The Gaussian unitary ensemble (GUE) describes systems which are not invariant with respect to time-reversal; its matrices are complex unitary. Finally, the Gaussian symplectic ensemble (GSE) describes time-reversal invariant systems with spin interaction.

To allow a comparison with regular systems, the Poisson orthogonal ensemble (POE) is often used. It combines random, statistically independent eigenvalues [Ber77b] with orthogonally invariant eigenvectors [Dit91]. Regular systems behave very *individualistic*, especially the statistics of the wavefunctions, thus the POE does not have the universal implications of the Gaussian ensembles.

The BGS-conjecture has been substantiated by many numerical [Boh84, Ber86] and experimental results, e. g. for microwave billiards [Stö90, Alt95]. The study of quantum chaos in microwave systems is possible, since the Helmholtz equation for flat microwave cavities is equivalent to the corresponding Schrödinger equation with Dirichlet boundary conditions [Stö99]. In this work, microwave systems are treated as scattering systems to take the influence of the antennas and wall absorption into account.
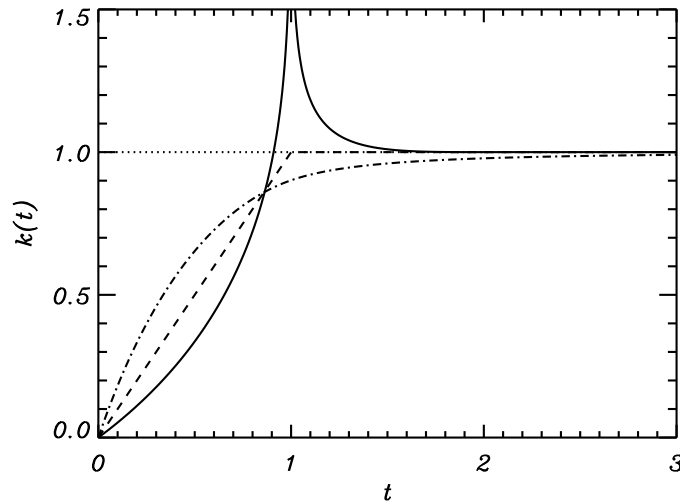
Figure 1.1: Spectral form factor $k(t) = 1-b_2(t)$ for the GOE (dashed-dotted), the GUE (dashed), the GSE (solid) and the Poisson spectrum (dotted). The time t is in units of the Heisenberg time.

One of the important fluctuation measures in quantum chaos studies is the two-point form factor $b_2(t)$ [Meh91]. Many statistical quantities like the number variance and the spectral rigidity can be expressed in terms of the two-point form factor, and we shall see that this is also true for correlation functions and fidelity decay.

The spectral form factor $k(t) = 1-b_2(t)$ can be obtained directly by a Fourier transform of the discrete spectrum. While the form factor is 1 for Poisson spectra, the correlations of the Gaussian ensembles cause the form factor to start from zero. This difference to the uncorrelated spectra is called the *correlation hole*. It is illustrated in figure 1.1.

In experiments one cannot study a closed system, but instead has to open the system for the measurement. This leads to a finite width of the resonances and thus to continuous intensity spectra.

Gorin and Seligman studied the correlation functions of intensity spectra using scattering theory [Gor02], and found that the correlation hole can also be observed in open systems, even in the regime of overlapping resonances. Their work was the starting point for the experiments presented in chapter 2. The scattering matrix was measured for microwave cavities with two antennas. It was analyzed in the regime of overlapping resonances. The

theoretical description in terms of a statistical scattering matrix (S-matrix) and the rescaled Breit-Wigner approximation has been applied to this regime.

The correlation hole could be observed both in the autocorrelation functions of the same S-matrix elements, and in the cross-correlation functions of different S-matrix elements. As predicted in reference [Gor02], the cross-correlation functions display a more pronounced difference between regular and chaotic systems.

The absorption in the cavity walls was modeled by additional decay channels. For a finite number of channels scattering theory predicts an algebraic decay, while our experimental results clearly suggest an exponential decay. This behavior can be described by infinitely many weakly coupled channels.

The major part of chapter 2 has already been published [Sch03]. In addition to the results of this paper, a generalization of the autocorrelation function to additional channels and the GUE case is given in appendix 2.A.

In chapters 3 and 4 the focus is shifted to the stability of quantum time-evolution. While the stability of a classical system is usually analyzed with respect to a change of the initial conditions, Peres proposed to study the stability of a quantum system against a change of the Hamiltonian [Per84], i. e. the underlying dynamics. As a simple benchmark for the stability of quantum motion, he proposed the overlap of the perturbed and unperturbed time-evolution of the same initial state.

The fidelity amplitude for some initial state $\psi(0)$ is defined as

$$f(t) = \langle \psi(0) | \exp(2\pi i H t) \exp(-2\pi i H' t) | \psi(0) \rangle \qquad (1.1)$$

and the fidelity by $F(t) = |f(t)|^2$, where H is the Hamiltonian of the unperturbed system, and H' the Hamiltonian of the perturbed one.

In the 1990s spin-echo experiments by H. Pastawski *et al* [Pas95] spawned a lot of interest in this field. T. Prosen formulated a general linear-response approach to calculate the fidelity [Pro02a, Pro03], and a semi-classical treatment was published both by Prosen and Žnidarič [Pro02b] and by Cerruti and Tomsovic [Cer02] in 2002.

The linear-response approach was later used by T. Gorin *et al* [Gor04a] to calculate the Gaussian average of the fidelity amplitude in the regime of small perturbation strengths,

$$f(t) = e^{-4\pi^2\lambda^2 C(t)} . \qquad (1.2)$$

where λ is the perturbation parameter, and $C(t)$ is given by

$$C(t) = \frac{t^2}{\beta} + \frac{t}{2} - \int_0^t \int_0^\tau b_2(\tau')\mathrm{d}\tau'\mathrm{d}\tau \,. \qquad (1.3)$$

β is the universality index, i.e. $\beta = 1$ for the GOE, $\beta = 2$ for the GUE, and $\beta = 4$ for the GSE. Equation (1.2) describes correctly the change from Gaussian to exponential decay with increasing perturbation strength.

It also shows that the fidelity decay is governed by the two-point form factor. And in particular, we see directly that for regular systems with $b_2(t) = 0$ the decay is much faster than for chaotic ones. As pointed out in reference [Pro02b], this has important implications for quantum information processing, where a high fidelity is crucial.

In chapter 3 the exact results of the Gaussian average are compared with numerical random matrix simulations and the linear-response results. For strong perturbations a partial recovery of the fidelity amplitude is found, and an intuitive explanation for this behavior is given in terms of a spectral Debye-Waller factor. Again the two-point form factor is important to fully explain this phenomenon. This chapter is based on a letter submitted for publication; a preprint [Stö04a] is already available.

In chapter 4 the fidelity amplitude has been studied experimentally. The scattering matrix was measured for two flat microwave cavities with classically chaotic dynamics, one with and one without marginally stable orbits. The perturbation of the systems was realized by a small shift of one wall.

The experience with correlation functions discussed in chapter 2 leads to a definition of the fidelity amplitude for scattering systems, which approaches the fidelity amplitude of the closed system under certain conditions.

The experimental results for the fidelity amplitude are in good agreement with the linear-response results (1.2). The perturbation strength extracted from the fidelity decay is in accordance with that obtained from the variance of level velocities. In the system with bouncing-ball orbits we observe strong variations of the perturbation strength, which can be directly associated with the marginally stable orbits. This chapter is based on a draft for a paper which has not been submitted yet [Sch04a].

In chapter 5 microwave measurements on dielectric billiards with mixed phase space are presented. Dielectric billiards with quadrupolar shape have received a lot of attention because of their highly directed emission patterns [Nöc97] which is a welcome effect in the design of microdisc lasers.

In the microwave experiment transmission spectra were measured from a fixed antenna inside the billiard to a moveable antenna, thus scanning both the inside and outside region of the billiard. A Fourier transfrom of the transmission spectra yields the pulse propagation, which was used to study the long-time dynamics of the system.

The Poynting vector, which describes the energy flow of the microwaves, was obtained from the measurement for each time step of the pulse propagation. Close to the boundary of the billiard it reveals a characteristic directionality of the microwave emission, which is in accordance with measurements of the far-field intensities of microdisc lasers [Sch04c].

To achieve a direct comparison to the internal dynamics of the classical system, the Husimi distributions of the pulse propagation were calculated. Averaging the Husimi distributions for the long-time dynamics provided a very clear picture of the internal dynamics in phase space. The results show very good agreement with classical simulations.

Since each chapter of this work is largely based on a paper already published, submitted or close to submission, there are some repetitions, in particular of introductory explanations and the description of the experimental technique. These were not eliminated to keep each chapter comprehensible on its own.

Chapter 2

Correlation functions of scattering matrix elements

2.1 Introduction

The correlation hole as seen in the Fourier transform of the stick spectrum of a closed Hamiltonian quantum system is particularly sensitive to long range spectral correlations, typical for random matrix models. This behavior in turn is indicative of chaos in the classical equivalent of the system via the quantum chaos conjecture [Cas80, Boh84]. Extensive work on the detection of such correlations using the correlation hole has been done in molecular physics [Lev86, Lom91, Lom93], nuclear physics [Lom94], and in the analysis of spectra from microwave cavities [Alt97] and optical resonators [Din02]. As the energy spectrum often is not available, Jost and Lombardi have early focused attention on the analysis of intensity spectra (see e. g. [Jos86]).

The Fourier transform $\hat{\sigma}_\alpha(t)$ of the intensity spectrum $\sigma_\alpha(E) = \sum_i \alpha_i^2 \, \delta(E - E_i)$ for a system with eigenenergies E_i and a state with amplitudes α_i yields

$$\hat{c}_A(t) = |\hat{\sigma}_\alpha(t)|^2 = \sum_i \alpha_i^4 + \sum_{i \neq j} \alpha_i^2 \, \alpha_j^2 \, \mathrm{e}^{2\pi \mathrm{i}\,(E_i - E_j)\,t} \ . \qquad (2.1)$$

The inverse participation ratio $\sum_i \alpha_i^4$ is $3/(N+2)$ for a random state. Averaging over a Gaussian orthogonal ensemble (GOE) in the large N-limit leads to $N\,\hat{c}_A(t) = 3 - b_2(t)$. Here N is the dimension of the matrices and $b_2(t)$ is the two-point form factor of the GOE [Meh91]. For the corresponding stick spectrum $1 - b_2(t)$ is obtained instead. For intensity spectra the cor-

relation hole is thus reduced to 1/3 of its full value. This reduction makes the detection of the correlation hole difficult. Reference [Alt97] discusses different ways to overcome this basic problem, which becomes more acute if cross sections are considered. Indeed, in the case of cross sections, the use of autocorrelation functions was shown to be of very limited efficiency.

The cross-correlations of independent intensity spectra, by contrast, display the full correlation hole. Indeed, performing the GOE average we find, instead of an inverse participation ratio, the product of two vector norms, i. e.

$$\hat{c}_C(t) = \hat{\sigma}_1^*(t)\,\hat{\sigma}_2(t) = \sum_i \alpha_i^2\,\beta_i^2 + \sum_{i \neq j} \alpha_i^2\,\beta_j^2\,e^{2\pi i\,(E_i - E_j)\,t}\,, \qquad (2.2)$$

where β_i refers to the component of the second state. Therefore the cross correlation behaves as $1 - b_2(t)$.

This simple fact has led to a detailed study of the possibility to observe the correlation hole in correlation functions of total and partial cross sections [Gor02]. To allow a comparison with regular systems, the Poisson orthogonal ensemble (POE) was used. It combines random, statistically independent eigenvalues [Ber77b] with orthogonally invariant eigenvectors [Dit91]. The POE does not have the universal implications of the GOE, both because the assumptions about spectral statistics are less well founded, and because we easily may encounter situations of preferred coordinate systems. Nevertheless, it is the best random matrix model for integrability that is available. Indeed cross-correlations prove to be the tool of choice to detect the correlation hole. Clearly the main interest of such an analysis results when the total absorption, i. e. the sum over all transmission coefficients, is fairly large, which implies that the average total width Γ is large compared to the mean level spacing d.

In this chapter we analyze the total cross sections of several normal-conducting microwave resonators with two antennas, obtained from measurements of the scattering matrix (S-matrix) via the optical theorem. The spectra of the studied systems exhibit different types of statistics, ranging from POE to GOE behavior. The wall absorption is significant and either comparable to or much larger than the transmission of the antennas. This leads us from resonances with small overlap to such with very strong overlap. Absorption channels are not directly accessible to experiments.

Our experiments address two interesting and quite general questions: On one hand, we test the use of cross-correlation functions to identify the effect of correlations in the spectrum of a chaotic Hamiltonian in the case of

overlapping resonances. The results of reference [Gor02] are compared with the data. On the other hand, we investigate whether absorption has to be included in terms of many weak or few strong channels, or whether the two cases cannot be distinguished. For this purpose we extend the results of [Gor02] to include an infinite number of weak channels, which we shall show to cause an exponential decay of the correlation functions.

In section 2 we recall some basics of random matrix scattering theory and some results of [Gor02] that are essential to our analysis, and we discuss the effect of a large number of channels with small absorption. In the following section the experimental setup and the studied billiards are explained. In sections 4 and 5 we shall see that the signatures of chaos are more pronounced in the cross-correlation than in the autocorrelation. Further we show that a description of absorption in terms of many channels is essential to obtain agreement with the experiment even in cases where the total absorption is of order one.

2.2 Basics of scattering theory and theoretical developments for absorption channels

There is an exact correspondence between the stationary classical wave equation of an ideal quasi-two-dimensional microwave cavity and the stationary Schrödinger equation for a two-dimensional quantum billiard of the same shape. This correspondence includes the scattering situation, by taking the antennas explicitly into account [Stö99], and ultimately even absorption phenomena.

The S-matrix for this situation is frequently used to describe resonant scattering arising e. g. in nuclear, atomic or mesoscopic systems [Guh98]:

$$S(E) = 1 - iV^T \frac{1}{E - H_{\text{eff}}} V , \quad H_{\text{eff}} = H_{\text{int}} - \frac{i}{2} V V^T . \qquad (2.3)$$

Here, H_{int} is the Hamiltonian describing the closed billiard, and V is a $N \times M$ matrix, which couples the N interior wave functions to M decay channels. For each antenna we need one channel or column vector, where the components V_{ja} are proportional to the amplitude of the billiard eigenfunction at the position of the antenna,

$$V_{ja} \propto \Psi_j(\vec{r}_a) , \qquad (2.4)$$

provided that the diameter of the antennas is small compared to the wavelength. This approximation may only be used in regions far from any thresholds, and the proportionality "constant" typically varies slowly with frequency [Stö02]. If symmetry-equivalent positions of the antennas are avoided, then typically the column vectors of V are approximately orthogonal to each other. Though not essential, this assumption simplifies the theoretical analysis.

It is convenient to work in the eigenbasis of the closed system H_{int}. Then the scattering matrix depends on the eigenvalues of H_{int} and on the coupling amplitudes, defined in equation (2.4). The analysis of the experiment is carried out in the framework of random matrix theory, where chaos is represented by a GOE and integrability by a POE. The two ensembles differ only in the distributions of the eigenvalues, while orthogonal invariance implies in both cases that the columns of the matrix V are distributed according to the invariant measure of the orthogonal group. In practice we use independent random Gaussian variables for the matrix elements, an approximation which becomes valid for large N.

We first present some elementary results of scattering theory using the notation of [Gor02]. From equation (2.3) the cross sections are derived as

$$\sigma_{ab}(E) = |\delta_{ab} - S_{ab}(E)|^2 \ . \tag{2.5}$$

Note that the experimental setup allows to measure S_{ab} directly. This avoids the difficulties related to the measurement of total cross sections. The optical theorem establishes a linear relation between the S-matrix elements and the total cross sections:

$$\sigma_{\text{tot}}^{(a)}(E) = 2 \left(1 - \text{Re} \, S_{aa}\right) . \tag{2.6}$$

The first quantity to study is the average S-matrix. The average can be a spectral average (denoted by $\langle \ldots \rangle$), an ensemble average ($\overline{\ldots}$), or a combination of both. For the average S-matrix all these averages must coincide. In [Mel85] it has been shown that

$$\overline{S_{aa}(E)} = \frac{1 - \kappa_a}{1 + \kappa_a} \ , \tag{2.7}$$

if $\overline{S(E)}$ is real and diagonal in the block of observable channels. The κ_a are real and positive parameters and relate to the coupling constants V_{ja} and the transmission coefficients T_a, respectively, via

$$\kappa_a = \frac{\pi}{2\,d}\langle V_{ja}^2 \rangle \ , \quad T_a = \frac{4\,\kappa_a}{(1 + \kappa_a)^2} \ . \tag{2.8}$$

The analysis will be performed in terms of correlation functions in the time domain,

$$\hat{C}[\sigma_{\mathrm{tot}}^{(a)}, \sigma_{\mathrm{tot}}^{(b)}](t) = \frac{1}{L} \left\{ \left\langle \hat{\sigma}_{\mathrm{tot}}^{(a)}(-t)\, \hat{\sigma}_{\mathrm{tot}}^{(b)}(t) \right\rangle - \left\langle \hat{\sigma}_{\mathrm{tot}}^{(a)}(-t) \right\rangle \left\langle \hat{\sigma}_{\mathrm{tot}}^{(b)}(t) \right\rangle \right\} , \quad (2.9)$$

where $\hat{\sigma}$ are Fourier transforms of the cross sections. The Fourier transforms are taken over a window of size L. It should be large compared to the average level distance d but sufficiently small so that the average S-matrix may be assumed constant.

Note that due to the optical theorem (2.6) the correlation function between total cross sections is equal to the correlation function between the corresponding S-matrix elements:

$$\hat{C}[\sigma_{\mathrm{tot}}^{(a)}, \sigma_{\mathrm{tot}}^{(b)}](t) = \hat{C}[S_{aa}, S_{bb}^*](|t|) . \quad (2.10)$$

For the GOE the correlation function can be calculated exactly, as will be shown below. For the general case we rely on the rescaled Breit-Wigner approximation (RBWA) [Gor02].

The rescaling is necessary, as soon as the transmission coefficients are not extremely small. In the standard Breit-Wigner approximation, the average width of the resonances is given by:

$$\langle \Gamma \rangle = \frac{2\,d}{\pi} \sum_{c=1}^{M} \kappa_c . \quad (2.11)$$

Yet Ericson showed that in the limit of many channels of comparable coupling strength, the correlation function of S-matrix elements or cross sections is proportional to $\exp(-\Gamma_C\, t)$. According to this derivation [Eri66, Bro81] Γ_C should be equal to $\langle \Gamma \rangle$, but actually

$$\Gamma_C = \frac{d}{2\pi} \sum_{c=1}^{M} T_c \quad (2.12)$$

gives the correct value for the correlation width. The two expressions coincide only in the limit where $\sum_{c=1}^{M} T_c \ll 1$. Thus the standard Breit-Wigner approximation is not valid in the range we are interested in. Fortunately, it turns out that the rescaling $\kappa_c \to T_c/4$ compensates for this defect up to rather strong overlaps [Gor02]. The rescaled Breit-Wigner approximation has already been applied in the regime of non-overlapping resonances [Alh98], but without mentioning the difference to the usual Breit-Wigner result.

In the case of the correlation functions (2.10), we first write the S-matrix elements (2.3) in terms of the standard Breit-Wigner approximation. Then we plug this into equation (2.9) and average over the spectrum of H_0. At last we perform the rescaling to obtain

$$\hat{C}[\sigma_{\text{tot}}^{(a)}, \sigma_{\text{tot}}^{(b)}](t) = T_a T_b \left\{ \left\langle g_a g_b \, \mathrm{e}^{-G\,t} \right\rangle - \left\langle g_a \, \mathrm{e}^{-G\,t/2} \right\rangle \left\langle g_b \, \mathrm{e}^{-G\,t/2} \right\rangle b_2(t) \right\} ,$$
(2.13)

with $G = \sum_{c=1}^{M} T_c \, g_c$. The normalized squared amplitudes $V_{ia}^2/\langle V_{ia}^2 \rangle$ are replaced by random variables g_c. Due to the orthogonal invariance of the ensembles considered, these variables are assumed to be Porter-Thomas distributed [Bro81]. Note that different situations may occur in the case of symmetries or integrable dynamics.

We account for wall absorption by introducing M_W additional channels. The transmission summed over all of them must equal the wall absorption,

$$T_W = \sum_{c=1}^{M_W} T_{M_A+c} ,$$
(2.14)

where $M_A = 2$ is the number of antennas. If M_W is small, the correlation functions depend on all transmission coefficients individually, and no simplification is possible. However, if M_W is large, we may use that asymptotically

$$\hat{C}[S_{ab}, S_{cd}^*](t) \to \mathrm{e}^{-T_W\,t} \, \hat{C}[\tilde{S}_{ab}, \tilde{S}_{cd}^*](t) \quad \text{as} \quad M_W \to \infty , \quad \max_{c > M_A}(T_c) \to 0 ,$$
(2.15)

where $\tilde{S}_{ab}$ describes the scattering system with only M_A channels, obtained by eliminating the last M_W columns in the coupling matrix V (see equation (2.3)). For the rescaled Breit-Wigner result (2.13) this proposition follows from the central limit theorem.

For later use we produce the result for the correlation function in the case of two antennas with equal transmission coefficients $T_1 = T_2 = T_A$. If the absorption in the walls is taken into account in the many channel limit via equation (2.15), the ensemble averages in equation (2.13) involve two random variables g_1 and g_2 only. Assuming that both are uncorrelated Porter-Thomas variables, and using that $G = T_A\,(g_1+g_2)+T_W$, one can evaluate the ensemble integrals analytically. This yields

$$\hat{C}[\sigma_{\text{tot}}^{(a)}, \sigma_{\text{tot}}^{(b)}](t) = T_A^2 \, \mathrm{e}^{-T_W\,t} \left\{ (1 + 2\delta_{ab}) \, (1 + 2T_A\,t)^{-3} - (1 + T_A\,t)^{-4} \, b_2(t) \right\} .$$
(2.16)

In appendix 2.A the autocorrelation function is calculated for a more general case, both for the GOE and the GUE.

In the GOE case, expression (2.15) can also be verified for the VWZ integral [Ver85], which gives an analytical expression for the exact correlation function in equation (2.10). The Fourier transform of the VWZ integral reads [Gor02]:

$$
C[S_{ab}, S_{cd}^*](t) = \frac{1}{4} \int_{\max(0,t-1)}^{t} \mathrm{d}r \ (t-r)(r+1-t) \prod_{e=1}^{M} [1 - T_e(t-r)] \ U(r) \,,
$$
(2.17)

where

$$
U(r) \;=\; 2 \int_0^{r^2} \mathrm{d}x \ \frac{\delta_{ab}\delta_{cd} \, \Delta_a \Delta_c \;+\; (\delta_{ac}\delta_{bd} + \delta_{ad}\delta_{bc}) \, \Pi_{ab}}{(t^2 - r^2 + x)^2 \, \sqrt{x(x+2r+1)} \, \sqrt{\prod_{e=1}^{M}(1 + 2T_e r + T_e^2 x)}} \,,
$$
(2.18)

$$
\Delta_a \;=\; 2T_a\sqrt{1 - T_a} \left(\frac{r + T_a x}{1 + T_a(2r + T_a x)} + \frac{t - r}{1 - T_a(t - r)} \right) \,,
$$
(2.19)

$$
\Pi_{ab} \;=\; 2T_a T_b \left(\frac{T_a T_b x^2 + [T_a T_b r + (T_a + T_b)(r+1) - 1]x + r(2r+1)}{(1 + 2T_a r + T_a^2 x)(1 + 2T_b r + T_b^2 x)} \right.
$$
$$
\left. + \frac{(t - r)(r + 1 - t)}{[1 - T_a(t - r)] \, [1 - T_b(t - r)]} \right) \,.
$$
(2.20)

We split the products occurring in expressions (2.17) and (2.18) and consider that part running over the absorption channels. In the asymptotic limit of equation (2.15), we find

$$
\prod_{c=1}^{M_W} [1 - T_{M_A+c}(t - r)] \to \mathrm{e}^{-T_W \, (t-r)}
$$
(2.21)

$$
\prod_{c=1}^{M_W} [1 + 2\, T_{M_A+c}\, r + T_{M_A+c}^2\, x]^{-1/2} \to \mathrm{e}^{-T_W \, r} \,,
$$
(2.22)

The r-dependent exponentials cancel, which proves our conjecture for the GOE case.

It will be useful to investigate the effect of the number of absorption channels M_W on the correlation function. For this purpose, we assume the total wall absorption to be fixed, $T_W = 1$, and distributed equally among the absorption channels $T_{M_A+c} = T_W/M_W$. Figure 2.1(a) shows the behavior of the autocorrelation function for the case of two antennas with $T_A = T_1 = T_2 = 0.26$ for different values of M_W. Note the significant changes in the shapes of the curves when M_W is varied. There are two previous microwave
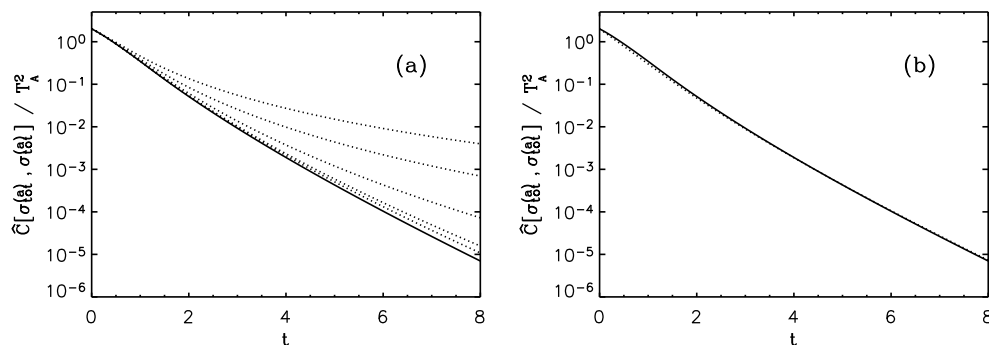
Figure 2.1: Autocorrelation functions for the GOE case with two accessible channels (antennas) with equal transmission coefficients $T_A = 0.26$ and total transmission for the wall absorption: $T_W = 1$, where the wall absorption is equally distributed over M_W channels. In (a) the VWZ result is shown as dotted lines for $M_W = 1, 4, 16, 64, 128$, and as a solid line for $M_W = \infty$. In (b) we compare the exact VWZ result (solid line) with the rescaled Breit-Wigner result (dotted line) for $M_W = \infty$.

experiments where the channel number dependence of the autocorrelation function was studied. The first one by Doron et al. [Dor90] failed to see any difference between exponential and algebraic decay behavior [Lew92]. However, in the more recent work by Alt et al. [Alt95] an algebraic decay of the autocorrelation function was observed.

In figure 2.1(b) we compare the exact result with the result from the rescaled Breit-Wigner approximation for $M_W = \infty$ using the same values for T_A and T_W as in figure 2.1(a). The difference between the RBWA and the exact result is very small. This permits us to use the much simpler and more flexible RBWA in the analysis of our experimental data. For larger values of T_A the RBWA is less accurate than in the example above, but it can still be used to determine T_W reliably from the autocorrelation function. The accuracy of the RBWA is discussed in detail in reference [Gor02].

2.3   Experiment

Since the experiment is described in detail elsewhere [Kuh00], we concentrate on the aspects relevant in the present context. Reflection and transmission measurements have been performed in microwave cavities of various shapes.

All cavities are flat, with top and bottom plate parallel to each other. The cavities are quasi-two-dimensional for frequencies $\nu < \nu_{max} = c/(2h)$ (h: height of the billiard). In this regime there is a complete equivalence between the stationary wave equation and the corresponding stationary Schrödinger equation, where the z component of the electric field corresponds to the quantum mechanical wave function,

$$\Delta \ \Psi(x,y) + E \ \Psi(x,y) = 0 \ , \quad E = \left(\frac{2\pi \ \nu}{c} \right)^2 \ , \qquad (2.23)$$

with Dirichlet boundary conditions. The antennas consisted of copper wires with a diameter of $1\,\mathrm{mm}$, projecting $l_p = 2$ or $4\,\mathrm{mm}$ into the resonator. An Agilent 8720ES vector network analyzer was used to determine the complete S-matrix. Measurements were taken in the frequency range from 1 to $16\,\mathrm{GHz}$ with a resolution of $0.5\,\mathrm{MHz}$.

The unwanted contribution of the cables to the S-matrix was removed by standard calibration procedures. It was not possible, however, to get rid of the contribution of connectors and antennas in this way. This posed a problem in particular for the reliable determination of the phase, which is vital for the cross-correlation measurements. Therefore, the phase shift from the antennas was determined from a reference measurement, where the cavity was removed, and only the antennas and the supporting top plate were present. We checked that the average S-matrix is in good approximation real and diagonal.

Four different cavities were used, which are presented in table 2.1. The rectangular and the Robnik billiard both have fixed geometries. Therefore, no ensemble average can be taken for these systems. Instead, we performed 10 measurements with different antenna positions on each system. By this we obtained 10 spectra of essentially the same system (it is slightly altered by the change of the antenna positions), but with different intensities for each of the resonances.

The billiard with threefold symmetry has been discussed in detail in [Sch02]. It is composed of an outer part and an insert, both with C_{3v} symmetry. By rotating the insert we get an ensemble of systems all displaying C_3 symmetry. However, configurations with C_{3v} symmetry have been avoided. We performed 30 measurements with different rotation angles and fixed antenna positions. The two antenna positions were in symmetry equivalent or nonequivalent positions, alternatively.

The fully chaotic billiard is a variant of the C_3 billiard, where the insert was
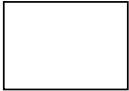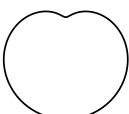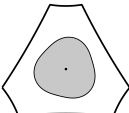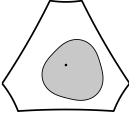
billiard type	shape	material	A/cm^2	L/cm	h/mm	l_p/mm
rectangle $34 \times 24\,\mathrm{cm}^2$		brass	816	116.0	8	2
Robnik billiard $\lambda = 0.4$		brass	474	77.5	8	2
billiard with C_3 symmetry		aluminum	2580	358.5	10	4
fully chaotic billiard		aluminum	2580	358.5	10	4

Table 2.1: Details of the studied billiards, with A: area, L: circumference, h: height of the billiard, and l_p: the projection length of the antennas into the billiards.

placed out of the center avoiding any symmetry. We performed 50 measurements for different positions of the insert. The classical dynamics for the latter two billiards is completely chaotic.

As described in section 2.2, the transmission coefficients T_A of the antennas are obtained from the average S-matrix (see equations (2.7) and (2.8)). In figure 2.2 the results for T_A as a function of frequency are shown for the rectangular and the fully chaotic billiard. One notices a strong frequency dependence of the coupling. Such a behavior is typical for wire antennas. For each system, the two antennas yield approximately the same transmission coefficients. In view of the frequency dependence of T_A and a comparable one of T_W to be discussed in section 2.4, we examined frequency intervals with a width of $1\,\mathrm{GHz}$ to assure that the average S-matrix and the total absorption are approximately constant.

The frequency dependence of the wall absorption is mainly due to the skin effect [Jac62]. The additional width acquired by the resonances is

$$\Gamma_W(\alpha) = \frac{8\pi^2}{c^2}\,\nu^2\,\frac{\delta(\nu)}{h}\left(1 + \frac{h\,L}{2A}\,\xi(\alpha)\right)\ ,\quad \delta(\nu) = \frac{1}{\sqrt{\pi\mu_0\sigma\nu}}\ ,\qquad (2.24)$$

where $\delta(\nu)$ is the so-called skin depth, and μ_0 and σ are the susceptibility and
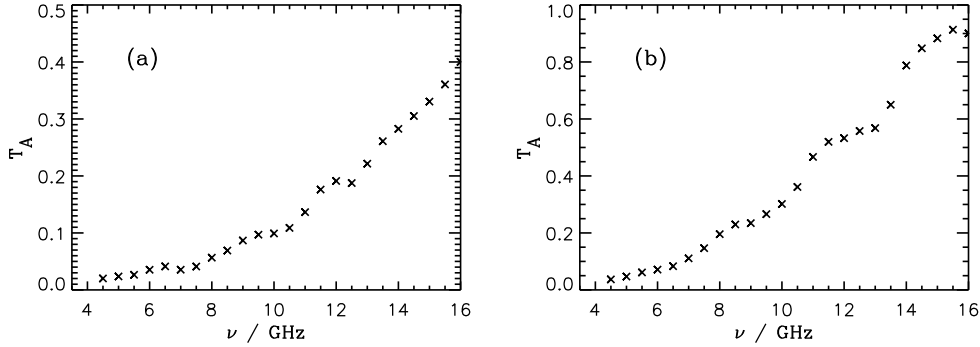
Figure 2.2: Transmission coefficient T_A obtained from the average S-matrix for (a) the rectangular and (b) the fully chaotic billiard.

the conductance of the cavity walls, respectively. The dimensionless quantity $\xi(\alpha)$ is of order one. It depends on the particular resonances, indexed by α.

To describe the wall absorption within our statistical model, we consider the average $\bar{\Gamma}_W$ and the variance $(\Delta\Gamma_w)^2$ of the absorption width. The number of absorption channels M_W^{eff} (with equal transmission coefficients) can be determined taking into account that in the statistical model Γ_W is the sum of M_W^{eff} random Porter-Thomas variables. In order to reproduce the average absorption width and its variance, it must hold:

$$\frac{1}{M_W^{\text{eff}}} = \frac{(\Delta\Gamma_W)^2}{\bar{\Gamma}_W^2} \approx \left(\frac{h\,L}{2A}\right)^2 (\Delta\xi)^2 \,, \tag{2.25}$$

where $(\Delta\xi)^2$ is the variance of $\xi(\alpha)$ as it fluctuates for different resonances. As $\xi(\alpha)$ is of order one, its variance cannot be larger. Therefore, $M_W^{\text{eff}} \gtrsim [2A/(hL)]^2$, which is greater than 200 for the studied cavities. This is certainly indistinguishable from an infinite number of channels.

2.4   Autocorrelation function

In this section we examine the Fourier transform of the autocorrelation function $\hat{C}[\sigma_{\text{tot}}^{(a)}, \sigma_{\text{tot}}^{(a)}](t)$ as given in equation (2.9). Figure 2.3 shows logarithmic plots of the autocorrelation functions for the rectangular and the fully chaotic billiard together with the rescaled Breit-Wigner approximation for GOE and POE - assuming an infinite number of weakly coupled channels for the absorption in the walls (see equation (2.16)). The results for the rectangular
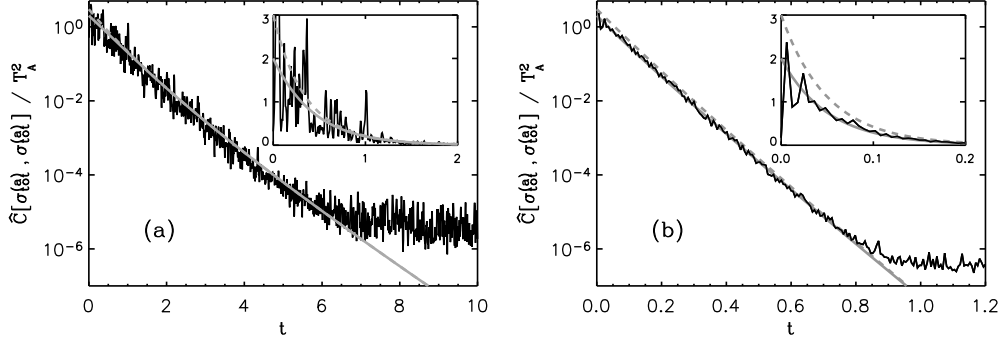
Figure 2.3: Logarithmic plot of $\hat{C}[\sigma_{tot}^{(a)}, \sigma_{tot}^{(a)}]/T_A^2$ for (a) the rectangular and (b) the fully chaotic billiard obtained from Fourier transforms over the frequency ranges 13 to 14 GHz and 14 to 15 GHz, respectively. The insets show the corresponding linear plots for small times t. The theoretical prediction from the RBWA is shown for the GOE (solid line) and the POE (dashed line). The parameters were $T_A = 0.261$, $T_W = 1.38$ for the rectangle, and $T_A = 0.848$, $T_W = 14.92$ for the fully chaotic billiard.

billiard do not allow us to distinguish between GOE and POE behavior due to their large fluctuations. At most we can see a hint of the fact that the autocorrelation function for rectangular billiards tends to 2.25 instead of 3 as $t \to 0$. For rectangular billiards the squared amplitudes (entering into equation (2.13)) are not Porter-Thomas distributed, leading to an autocorrelation function that is closer to the prediction for GOE than to the one for POE.

The ensemble averaged autocorrelation function of the fully chaotic billiards shows much smaller fluctuations, of course, and we observe a very good agreement with the GOE prediction. The correlation hole can be seen in particular in the linear plot shown in the inset of figure 2.3(b). However, the correlation hole is reduced to 1/3 of its full value (see section 2.1), and the difference to integrable systems may be even smaller.

The experimental autocorrelation function follows the theoretical curve for an infinite number of absorption channels over five orders of magnitude. Then the autocorrelation deviates from the theoretical curve. This is a consequence of the finite frequency interval used in the Fourier transform. The long-time behavior is dominated by the Welch filter applied. Comparison with figure 2.1 shows that more than 100 weakly coupled channels have to be assumed to explain this behavior, but the simplifying assumption of infinitely many channels is in accordance with the experiment as well. Further, we observe
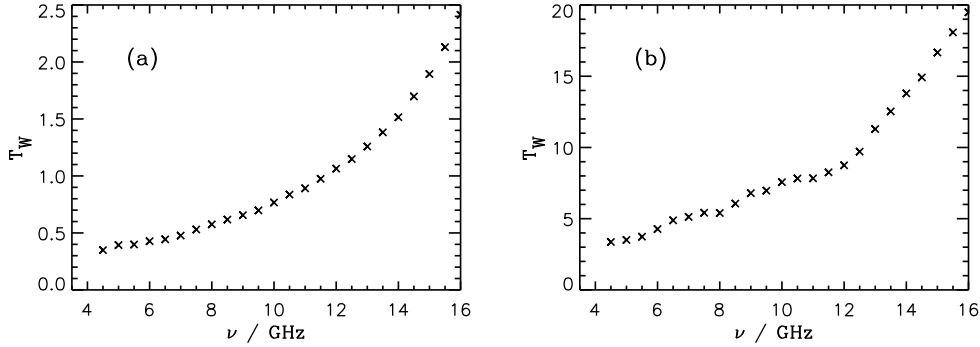
Figure 2.4: Transmission T_W into the walls, obtained from a fit to the auto-correlation function for (a) the rectangular and (b) the fully chaotic billiard.

that the rescaled Breit-Wigner approximation is sufficient to describe the experimental results.

As the antenna transmission T_A has been obtained independently, the wall transmission T_W can be determined by fitting the experimental autocorrelation function with the corresponding rescaled Breit-Wigner expression. This procedure works well for a large frequency range, and all results presented in this chapter have been obtained in this way. In the low frequency regime, however, a two-parameter fit of the autocorrelation function, treating both T_W and T_A as free parameters, yielded somewhat better results. Figure 2.4 shows the frequency dependence of T_W, as determined from the autocorrelation function, both for the rectangular and for the fully chaotic billiard.

2.5   Cross-correlation function

We now present cross-correlation functions $\hat{C}[\sigma_{\text{tot}}^{(a)}, \sigma_{\text{tot}}^{(b)}](t)$ of the total cross sections, which are equivalent to the ones of the respective diagonal S-matrix elements, see equation (2.10). Figure 2.5 shows $\hat{C}[\sigma_{tot}^{(a)}, \sigma_{tot}^{(b)}]/T_A^2$ for the fully chaotic billiard. The dotted and the dashed lines correspond to the expectation from the rescaled Breit-Wigner approximation.

Even after averaging over 50 realizations, the fluctuations are still quite strong. Therefore we apply a smoothing over an interval of size $\ln 2/T_W$, leading to the smooth behavior displayed in figure 2.5(b). All results presented below are smoothed in this way.
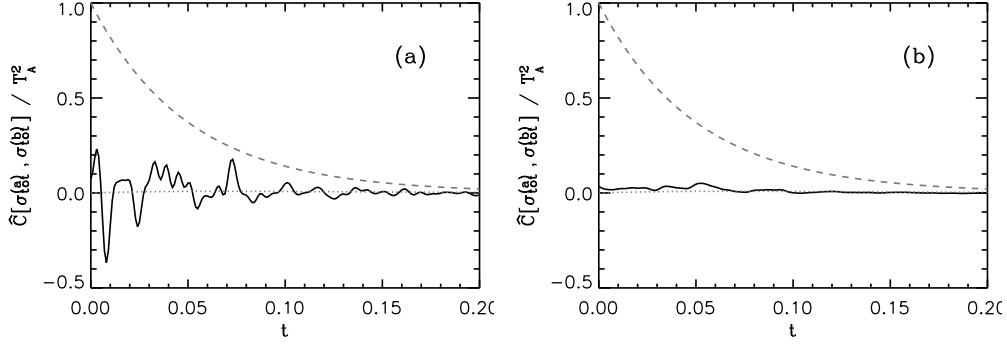
Figure 2.5: Cross-correlation function $\hat{C}[\sigma_{tot}^{(a)}, \sigma_{tot}^{(b)}]/T_A^2$ for the fully chaotic billiard, averaged over 50 realizations, (a) before smoothing and (b) after smoothing. The Fourier transform was taken over the frequency range of 14 to 15 GHz. The RBWA is shown for the GOE (dotted line) and for the POE (dashed line) with $T_A = 0.848$ and $T_W = 14.92$.

Figure 2.6 shows the smoothed results for the fully chaotic billiard both in linear and logarithmic plots for three different frequency regimes. In contrast to the expectation for integrable systems, the cross correlation is suppressed for small times t. The measurement thus clearly exhibits the correlation hole expected for chaotic systems. In particular the logarithmic plots demonstrate that the experimental results are in good agreement with the rescaled Breit-Wigner approximation for the GOE over several orders of magnitude, and clearly distinguishable from the POE expectations. For higher frequencies the absorption increases, resulting in a higher value for T_W and thus a sharper decline of the cross-correlation.

As an example for an integrable system, we present the cross-correlation function for the rectangular billiard in figure 2.7(a) together with the rescaled Breit-Wigner approximation for the GOE and the POE. The difference to chaotic systems is clearly seen. The discrepancy of our results from the POE is not surprising, because the antennas disturb the system, leading to a shift of resonance positions and thus to correlations in the spectrum. The intermediate situation is shown in figure 2.7(b) for the Robnik billiard with mirror symmetry and non-symmetric antenna positions. For $\lambda = 0.4$ the classical phase space of the Robnik billiard is chaotic [Rob83], apart from possible tiny stability islands [Dul01]. Additionally, the theoretical result for the superposition of two GOE is plotted as dash-dotted line. In this case the two-point form factor $b_2(t)$ for the GOE in equation (2.16) has to be replaced by $b_2(2t)$.
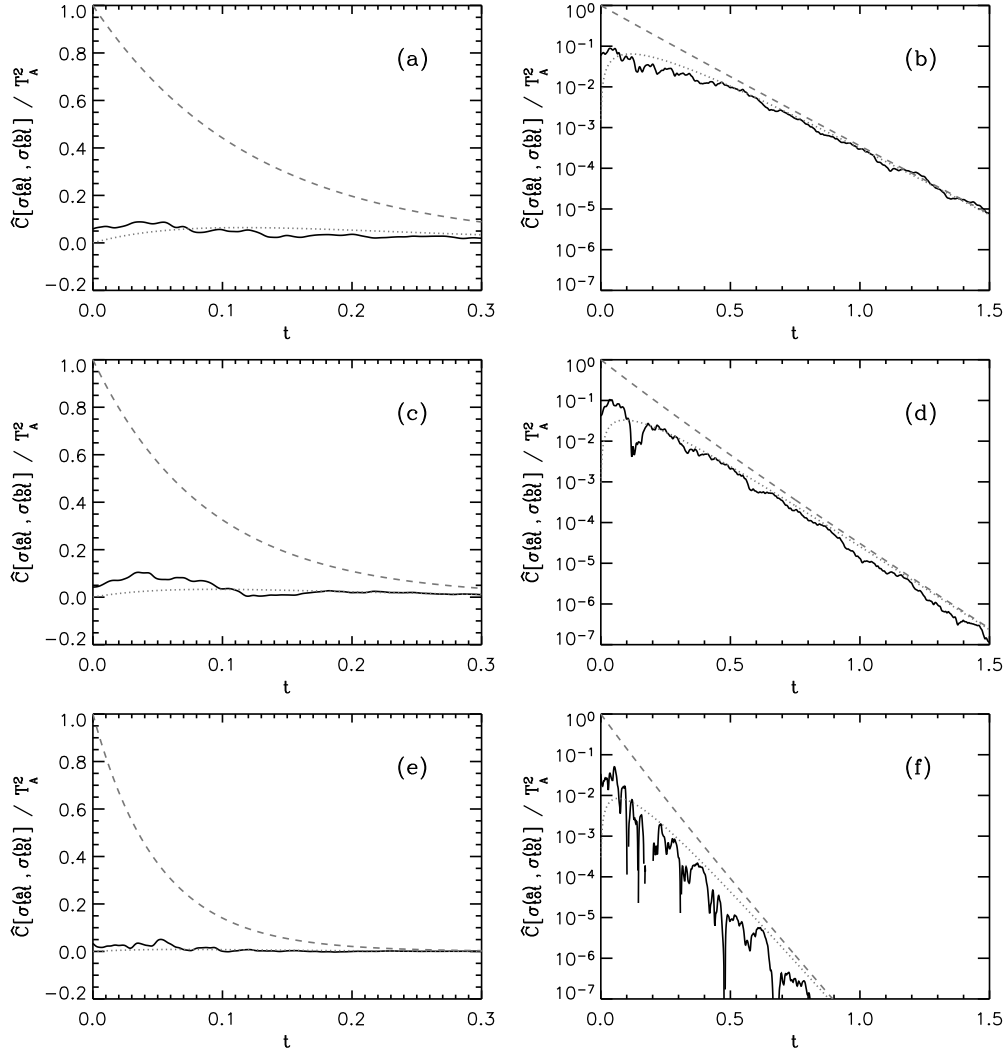
Figure 2.6: Cross-correlation function $\hat{C}[\sigma_{tot}^{(a)}, \sigma_{tot}^{(b)}]/T_A^2$ for the fully chaotic billiard, plotted linearly (left column) and logarithmically (right column), where the Fourier transform was taken over three different frequency regimes. (a), (b): ν=8.5 to 9.5 GHz, $T_A = 0.234$, $T_W = 6.79$; (c), (d): ν=11 to 12 GHz, $T_A = 0.52$, $T_W = 8.26$; (e), (f): ν=14 to 15 GHz, $T_A = 0.848$, $T_W = 14.92$. The RBWA is shown for the GOE (dotted line) and for the POE (dashed line).
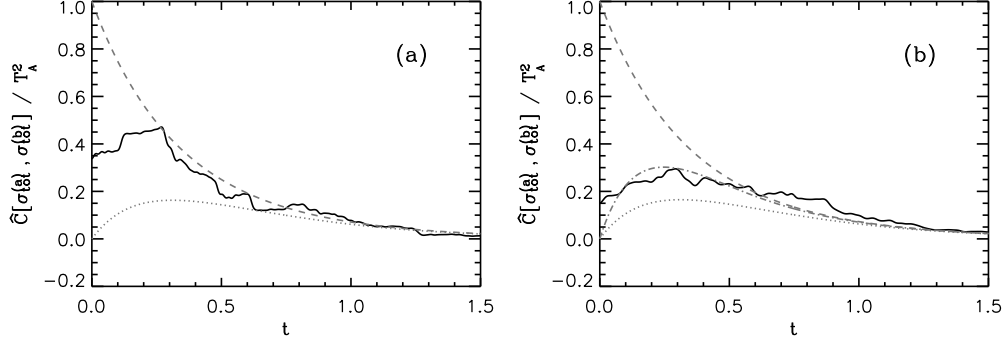
Figure 2.7: Cross-correlation function $\hat{C}[\sigma_{tot}^{(a)}, \sigma_{tot}^{(b)}]$ for (a) the rectangular and (b) the Robnik billiard with the Fourier transform taken over the frequency range 13 to 14 GHz. Dotted and dashed lines are the RBWA results for GOE and POE, respectively. The dash-dotted line in (b) corresponds to the RBWA for two GOE (see text). The parameters were $T_A = 0.261$, $T_W = 1.38$ for the rectangular, and $T_A = 0.254$, $T_W = 1.39$ for the Robnik billiard.
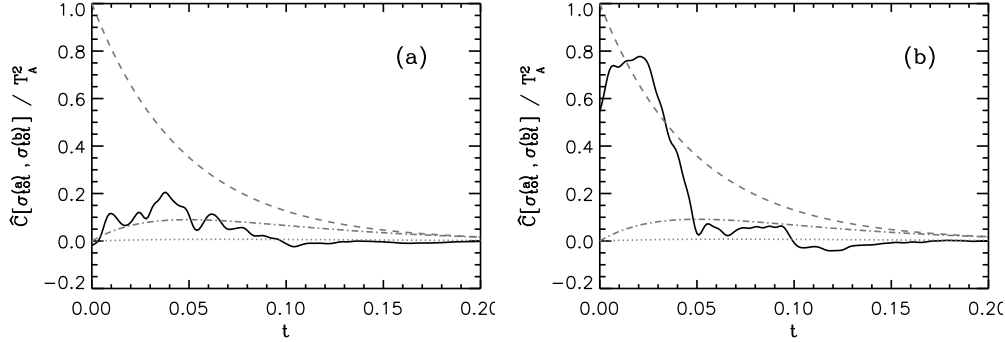
Figure 2.8: Cross-correlation function $\hat{C}[\sigma_{tot}^{(a)}, \sigma_{tot}^{(b)}]$ for the C_3 billiard with (a) asymmetric and (b) symmetric antenna positions, with the Fourier transform taken over the frequency range 14 to 15 GHz. Dotted and dashed lines are the RBWA results for GOE and POE, respectively. The dash-dotted line in (b) corresponds to the RBWA for the C_3 billiard (see text). The parameters were $T_A = 0.877$, $T_W = 15.84$ for (a), and $T_A = 0.860$, $T_W = 15.61$ for (b).

In systems with point symmetries caution is commanded with respect to the antenna positions, because the amplitudes at symmetric antenna positions are strongly correlated. This is illustrated in figure 2.8 showing the cross-correlation for the billiard with C_3 symmetry both for symmetric and asymmetric antenna positions. In addition to the POE and GOE curves, the rescaled Breit-Wigner expectation for the C_3 billiard is shown. For the two-point form factor in equation (2.16) the results from reference [Sch02] are used:

$$b_2^{C3}(t) = \frac{1}{3}\left(b_2^{GOE}(3t) + 2b_2^d\left(\frac{3t}{2}\right)\right) , \qquad (2.26)$$

where $b_2^{GOE}(t)$ is the two-point form factor for the singlet GOE spectrum and

$$b_2^d(t) = -e^{-8\pi^2\Delta t^2} + 2e^{-4\pi^2\Delta t^2}b_2^{GUE}(t) \qquad (2.27)$$

is the one for the doublet GUE spectrum. The parameter $\Delta = 0.125$ accommodates the splitting of the doublet spectrum due to symmetry breaking.

For asymmetric antenna positions, a good correspondence between experiment and theory is found, but for symmetric positions there are dramatic deviations. In the ideal case one would expect a result which is much closer to the autocorrelation function, but small deviations from symmetry induce uncontrollable variations.

2.6 Summary and Outlook

We have measured the diagonal S-matrix elements of two channels as a function of frequency for a variety of different microwave cavities with and without symmetries, and with integrable or chaotic classical dynamics. They displayed different amounts of resonance overlap and antenna coupling. Via the optical theorem the diagonal S-matrix elements contain the same information as the total cross sections.

We discuss the experimental results in terms of autocorrelation and cross-correlation functions in the time domain. The wall absorption of the billiards is expressed in terms of unmeasurable channels. We find that an exponential decay of correlations, corresponding to infinitely many channels, describes the experimental results adequately. Comparison with the rescaled Breit-Wigner approximation for random matrix models shows good agreement with experiment, if we use the wall absorption as a fit parameter. The cross-correlation was expected to display the difference between integrable and chaotic systems

more clearly than the autocorrelation. Indeed, our experiments confirm that the correlation hole is more pronounced in the cross-correlation function.

Due to the optical theorem, total cross sections are accessible via the measurement of reflection matrix elements for microwave cavities. This is in contrast to particle scattering experiments, where total cross sections can only be measured in exceptional cases and their measurement in two different entrance channels is even more difficult. In these experiments only partial cross sections are available. Theory [Gor02] suggests that the correlation hole should be best observable in correlations between cross sections without any coinciding channel indices. The simplest case of this type is the cross-correlation function of different elastic cross sections.

2.A   Autocorrelation for additional channels

The result for the autocorrelation function, given in equation (2.16), holds for the case of two channels with the same transmission coefficients and an absorbing wall. This can easily be generalized to an arbitrary number of channels.

Starting with expression (2.13) for the correlation functions in the rescaled Breit-Wigner approximation, we are going to calculate the Gaussian average of the autocorrelation function for additional channels. To this end we set

$$G = \sum_{c=1}^{M} T_c\, g_c = T_a g_a + \sum_{c=2}^{M} T_c\, g_c\,, \qquad (2.28)$$

where the index a corresponds to the antenna used for the measurement, and the indices $2,\ldots,M$ to additional antennas or other decay channels. Inserting this into equation (2.13) yields

$$\hat{C}[\sigma_{\mathrm{tot}}^{(a)}, \sigma_{\mathrm{tot}}^{(a)}](t) \;=\; T_a^2 \left\{ \left\langle g_a^2\, \mathrm{e}^{-T_a g_a\, t} \right\rangle \prod_{c=2}^{M} \left\langle \mathrm{e}^{-T_c g_c\, t} \right\rangle \right.$$
$$\left. - b_2(t) \left\langle g_a\, \mathrm{e}^{-T_a g_a\, t/2} \right\rangle^2 \prod_{c=2}^{M} \left\langle \mathrm{e}^{-T_c g_c\, t/2} \right\rangle^2 \right\}\,. \quad (2.29)$$

As mentioned in section 2.2 the variables g_a and g_c are Porter-Thomas distributed in the GOE case. Thus the averages in equation (2.29) can be

calculated analytically, yielding

$$
\hat{C}[\sigma_{\text{tot}}^{(a)}, \sigma_{\text{tot}}^{(a)}](t) = T_a^2 \left\{ \frac{3}{(1 + T_a t)^{5/2}} \prod_{c=2}^{M} \frac{1}{(1 + 2T_c t)^{1/2}} \right.
$$
$$
\left. - \frac{b_2^{\text{GOE}}(t)}{(1 + T_a t)^3} \prod_{c=2}^{M} \frac{1}{1 + T_c t} \right\} . \tag{2.30}
$$

This result can be used to explore the effect of a finite number of additional absorption channels as shown in figure 2.1(a) in section 2.2, but it can also be used to describe cases where the antenna transmissions are not equal or where there is only one antenna involved.

In the GUE case the variables g_a and g_c are exponentially distributed. This leads to the following result

$$
\hat{C}[\sigma_{\text{tot}}^{(a)}, \sigma_{\text{tot}}^{(a)}](t) = T_a^2 \left\{ \frac{2}{(1 + T_a t)^3} \prod_{c=2}^{M} \frac{1}{1 + T_c t} \right.
$$
$$
\left. - \frac{16\, b_2^{\text{GUE}}(t)}{(2 + T_a t)^4} \prod_{c=2}^{M} \frac{4}{(2 + T_c t)^2} \right\} . \tag{2.31}
$$

Chapter 3

Fidelity recovery in chaotic systems and the Debye-Waller factor

3.1   Introduction

The concept of fidelity has been developed by Peres as a tool to characterize the stability of a quantum-mechanical system against perturbations [Per84]. It was introduced as the squared modulus of the overlap integral of a wave packet with itself after developing forth and back under the influence of two slightly different Hamiltonians [Per84]. Very similar concepts had been applied already in the old spin-echo experiments of nuclear magnetic resonance half a century ago (see reference [Abr61] for a review). The renewed interest in the topic results from the idea to realize quantum computers by means of spin systems, where stability against quantum-mechanical perturbations obviously is of vital importance [Fra04].

Roughly speaking there are three regimes. In the perturbative regime, where the strength of the perturbation is small compared to the mean level spacing, the decay of the fidelity is Gaussian. As soon as the perturbation strength becomes of the order of the mean level spacing, exponential decay starts to dominate, with a decay constant obtained from Fermi's golden rule [Cer02, Van03]. For very strong perturbations the decay becomes independent of the strength of the perturbation. Here, in the Loschmidt regime, the decay is still exponential, but now the decay constant is given by the classical Lyapunov

exponent [Jal01]. Exactly such a behavior had been observed experimentally in a spin-echo experiment on isolated spins coupled weakly to a bath of surrounding spins [Pas95].

Gorin et al. [Gor04a] calculated the fidelity decay within random matrix theory in the regime of small perturbations and could correctly describe the change from Gaussian to exponential behavior with increasing perturbation strength. The Lyapunov regime is non-universal and thus not accessible in a random matrix model.

Intuitively, one would expect that in chaotic systems the fidelity decay is stronger than in integrable ones. The opposite is true. Prosen et al. [Pro02b] showed that a chaotic system is much more *fidèle* than a regular one, and suggested to use chaotic systems in quantum computing to suppress chaos.

It will be shown here that the situation is even more favorable, and that for chaotic systems there is a partial recovery of the fidelity at the Heisenberg time. This work extends the results by Gorin et al. [Gor04a] to the regime of strong perturbations using supersymmetry techniques. It is stressed that our result is generic and not restricted to random matrix systems. E. g. in a spin-chain model the fidelity recovery has been observed recently [Pin].

Using the Brownian-motion model for the eigenvalues of random matrices introduced by Dyson many years ago [Dys62], it will be shown that this behavior has its direct analogue in the Debye-Waller factor of solid state physics. We shall sketch the calculation for the GUE only, and will just cite the result for the GOE. More details will be presented in a forthcoming paper [Stö04b].

3.2 Exact results

Let H_0 be the unperturbed Hamiltonian and

$$H_\epsilon = H_0 + \frac{\sqrt{\epsilon}}{2\pi} V \tag{3.1}$$

the perturbed one. This somewhat unusual definition of the perturbation strength ϵ has been applied for later convenience. The fidelity amplitude is given by

$$f_\epsilon(\tau) = \langle \psi(0)| \exp(2\pi \imath H_\epsilon \tau) \exp(-2\pi \imath H_0 \tau)|\psi(0)\rangle \ , \tag{3.2}$$

where $\psi(0)$ is the wave function at the beginning. It is assumed that H_0 has a mean level spacing of one, that the variance of the off-diagonal elements of V is one, and that ϵ is of the order of one. This guarantees that the shift of the levels due to the parameter variation is of the order of the mean level spacing. The squared modulus of $f_\epsilon(\tau)$ yields the fidelity $F_\epsilon(\tau)$, originally introduced by Peres [Per84]. The calculation of the average of $F_\epsilon(\tau)$, however, is technically more involved, and therefore not considered here.

In the paper by Gorin et al. [Gor04a] the Gaussian average of the fidelity amplitude was calculated in the regime of small perturbation strengths, correct up to $\mathcal{O}(\epsilon)$,

$$f_\epsilon(\tau) \sim e^{-\epsilon\,C(\tau)}\,. \tag{3.3}$$

where $C(\tau)$ is given by

$$C(\tau) = \frac{\tau^2}{\beta} + \frac{\tau}{2} - \int_0^\tau \int_0^t b_2(t')\mathrm{d}t'\mathrm{d}t\,, \tag{3.4}$$

and $b_2(\tau)$ is the two-point form factor. β is the universality index, i. e. $\beta = 1$ for the Gaussian orthogonal ensemble (GOE), $\beta = 2$ for the Gaussian unitary ensemble (GUE), and $\beta = 4$ for the Gaussian symplectic ensemble (GSE). Equation (3.3) describes correctly the change from Gaussian to exponential decay with increasing perturbation strength.

It is a disadvantage of the Hamiltonian (3.1) that its mean density of states changes with ϵ. The more it is somewhat inconvenient that the variances of the matrix elements of H_0 and V differ. We therefore adopt a slightly different parameter variation,

$$H_\phi = H_0 \cos\phi + H_1 \sin\phi \tag{3.5}$$

where the Hamiltonians are truncated to a finite rank N. We assume that the matrix elements of H_0 and H_1 have zero average, are uncorrelated, and are Gaussian distributed with a variance given by

$$\left\langle |(H_n)_{kl}|^2 \right\rangle = \frac{N}{\pi^2} \left\{ \begin{array}{ll} 1\,, & k \neq l \\ \frac{2}{\beta}\,, & k = l \end{array} \right. \qquad n = 0, 1\,. \tag{3.6}$$

It follows that the mean density of states in the band center is one, independent of ϕ [Meh91]. The transition from equation (3.1) to equation (3.5) is achieved by means of the substitutions

$$H_0 \to \cos\phi\, H_0\,, \qquad V \to \frac{\pi}{\sqrt{N}} \cos\phi\, H_1\,, \tag{3.7}$$

where $\tan\phi = \sqrt{\frac{\epsilon}{4N}}$. ϕ is thus of $\mathcal{O}(\frac{1}{\sqrt{N}})$, and ϵ is given in the limit of large N by

$$\epsilon = 4N\phi^2 \tag{3.8}$$

The fidelity is invariant to a shift of ϕ as is easily seen. This can be used to get an expression that does not dependent on the sign of ϕ. The average of the fidelity amplitude may then be written as

$$f_\epsilon(\tau) = \frac{1}{N} \left\langle \text{Tr}\left[e^{2\pi\imath(cH_0+sH_1)\tau}e^{-2\pi\imath(cH_0-sH_1)\tau}\right]\right\rangle, \tag{3.9}$$

where $c = \cos(\phi/2)$, $s = \sin(\phi/2)$.

Equation (3.9) may now be transformed into

$$f_\epsilon(\tau) = \int dE_1\,dE_2 e^{2\pi\imath(E_1-E_2)\tau}\,R_\phi\left(E_1,E_2\right) \tag{3.10}$$

where

$$R_\phi\left(E_1,E_2\right) \sim$$
$$\frac{1}{N}\left\langle\text{Tr}\left(\frac{1}{E_{1-}-cH_0-sH_1}\frac{1}{E_{2+}-cH_0+sH_1}\right)\right\rangle, \tag{3.11}$$

with $E_\pm = E \pm \imath\eta$. Using standard supersymmetry techniques [Ver85], this can be written as

$$R_\phi\left(E_1,E_2\right) \sim$$
$$\frac{1}{N}\int d[x]\,d[y]\sum_{n,m}(x_n^*x_m - \xi_n^*\xi_m)(y_m^*y_n - \eta_m^*\eta_n)$$
$$\times e^{-\imath\left[\mathbf{x}^\dagger E_1\mathbf{x}-\mathbf{y}^\dagger E_2\mathbf{y}\right]}$$
$$\times \left\langle e^{\imath c\left[\mathbf{x}^\dagger H_0\mathbf{x}-\mathbf{y}^\dagger H_0\mathbf{y}\right]}\right\rangle \left\langle e^{\imath s\left[\mathbf{x}^\dagger H_1\mathbf{x}+\mathbf{y}^\dagger H_1\mathbf{y}\right]}\right\rangle, \tag{3.12}$$

where $\mathbf{x} = (x_1,\xi_1,\ldots,\xi_N)^T$, $\mathbf{y} = (y_1,\eta_1,\ldots,\eta_N)^T$, and

$$d[x] = \prod_n dx_n\,dx_n^*\,d\xi_n\,d\xi_n^*, \quad d[y] = \prod_n dy_n\,dy_n^*\,d\eta_n\,d\eta_n^*.$$

We adopt the usual convention using latin letters for commuting, and greek ones for anticommuting variables, respectively. Now the Gaussian average over the matrix elements of H_0 and H_1 can be performed elementary.

The subsequent steps (Hubbard-Stratonovich transformation, integration over the x, y variables, saddle point integration etc.) are essentially the same ones as for the calculation of the spectral form factor (see e. g. chapter 10 of reference [Haa01] for the GUE case). Details will be presented in our forthcoming publication [Stö04b]. In the limit $N \to \infty$ all integrations can be performed for the GUE and lead to the particularly simple result

$$f_\epsilon(\tau) = \begin{cases} e^{-\frac{1}{2}\epsilon\tau}\left[s(\frac{1}{2}\epsilon\tau^2) - \tau s'(\frac{1}{2}\epsilon\tau^2)\right], & \tau \leq 1 \\ e^{-\frac{1}{2}\epsilon\tau^2}\left[s(\frac{1}{2}\epsilon\tau) - \frac{1}{\tau}s'(\frac{1}{2}\epsilon\tau)\right], & \tau > 1 \end{cases}, \tag{3.13}$$

where

$$s(x) = \frac{\sinh(x)}{x} . \tag{3.14}$$

We have thus obtained an analytic expression for the GUE average of the fidelity amplitude for arbitrary perturbation strengths. In the limit of small perturbations it is in complete accordance with the result obtained by Gorin et al. [Gor04a].

The calculation for the GOE is done in exactly the same way. It is technically much more involved, but fortunately most of the work for this case has already been done by Verbaarschot, Weidenmüller, and Zirnbauer in their disseminating work [Ver85]. In this way we get for the GOE average of the fidelity amplitude

$$\begin{aligned} f_\epsilon(\tau) &= 2 \int\limits_{\text{Max}(0,\tau-1)}^{\tau} du \int\limits_0^u \frac{v\,dv}{\sqrt{[u^2 - v^2][(u+1)^2 - v^2]}} \\ &\times \frac{(\tau - u)(1 - \tau + u)}{(v^2 - \tau^2)^2} \\ &\times [(2u+1)\tau - \tau^2 + v^2]e^{-\frac{1}{2}\epsilon[(2u+1)\tau - \tau^2 + v^2]} . \end{aligned} \tag{3.15}$$

3.3   Comparison with linear-response and numerical simulations

In this section we present random matrix simulations to affirm the analytical findings for the Gaussian orthogonal and unitary ensembles. Further we show numerical results for the Gaussian symplectic ensemble which has not been treated analytically.

In our simulations the Hamiltonians H_0 and H_1 are random matrices of dimension $N \times N$ with variances of the diagonal and off-diagonal elements given by equation (3.6). To calculate the fidelity amplitude, we write expression (3.9) as

$$
\begin{aligned}
f_\epsilon(\tau) &= \frac{1}{N} \left\langle \mathrm{Tr} \left[R_\phi \mathrm{e}^{2\pi \iota H_\phi^D \tau} R_\phi^{-1} R_0 \mathrm{e}^{-2\pi \iota H_0^D \tau} R_0^{-1} \right] \right\rangle \\
&= \frac{1}{N} \left\langle \mathrm{Tr} \left[\mathrm{e}^{2\pi \iota H_\phi^D \tau} R \mathrm{e}^{-2\pi \iota H_0^D \tau} R^{-1} \right] \right\rangle \\
&= \frac{1}{N} \left\langle \sum_{kl} \mathrm{e}^{2\pi \iota \tau (E_k^{(\phi)} - E_l^{(0)})} |R_{lk}|^2 \right\rangle ,
\end{aligned}
\tag{3.16}
$$

where $H_0^D = R_0^{-1} H_0 R_0$ and $H_\phi^D = R_\phi^{-1} H_\phi R_\phi$ are diagonal, and $R = R_\phi^{-1} R_0$.

In the numerical simulations the trace in equation (3.16) was restricted to 20 percent of the eigenvalues in the center of the spectrum where the mean level density is still about constant. The average was taken over up to 8000 random matrices for H_0, and for each of them over 50 random matrices for H_1. For larger values of the perturbation strength ϵ it became more and more important to choose the dimension N of the matrices large enough to avoid finite-size effects. $N = 500$ proved to be sufficient for $\epsilon \leq 10$. The influence of the finite dimension N on the fidelity amplitude is discussed in appendix 3.B.

The results are shown in Figure 3.1. For the GOE and the GUE the numerical simulations are in perfect agreement with the analytical results for all ϵ values shown. For comparison, the fidelity amplitudes in the linear response approximation (3.3) are presented as well. For small perturbation strengths or small values of τ the linear response result is a good approximation, but the limits of its validity are also clearly illustrated.

For small perturbation strengths ϵ the decay of the fidelity is predominantly Gaussian which changes into a behavior showing a cross-over from an exponential to a Gaussian decay at $\epsilon \approx 1$, in accordance with literature. The most conspicuous result of this chapter, however, is the partial recovery of the fidelity at the Heisenberg time $\tau = 1$ which has not been reported previously to the best of our knowledge. This recovery is most pronounced for the GSE and least for the GOE. This is illustrated in Figure 3.2 showing a direct comparison of the fidelity amplitudes of the Gaussian ensembles for $\epsilon = 30$.

The way the recovery emerges with increasing perturbation strength is illustrated in figure 3.3 for the GOE and the GUE.
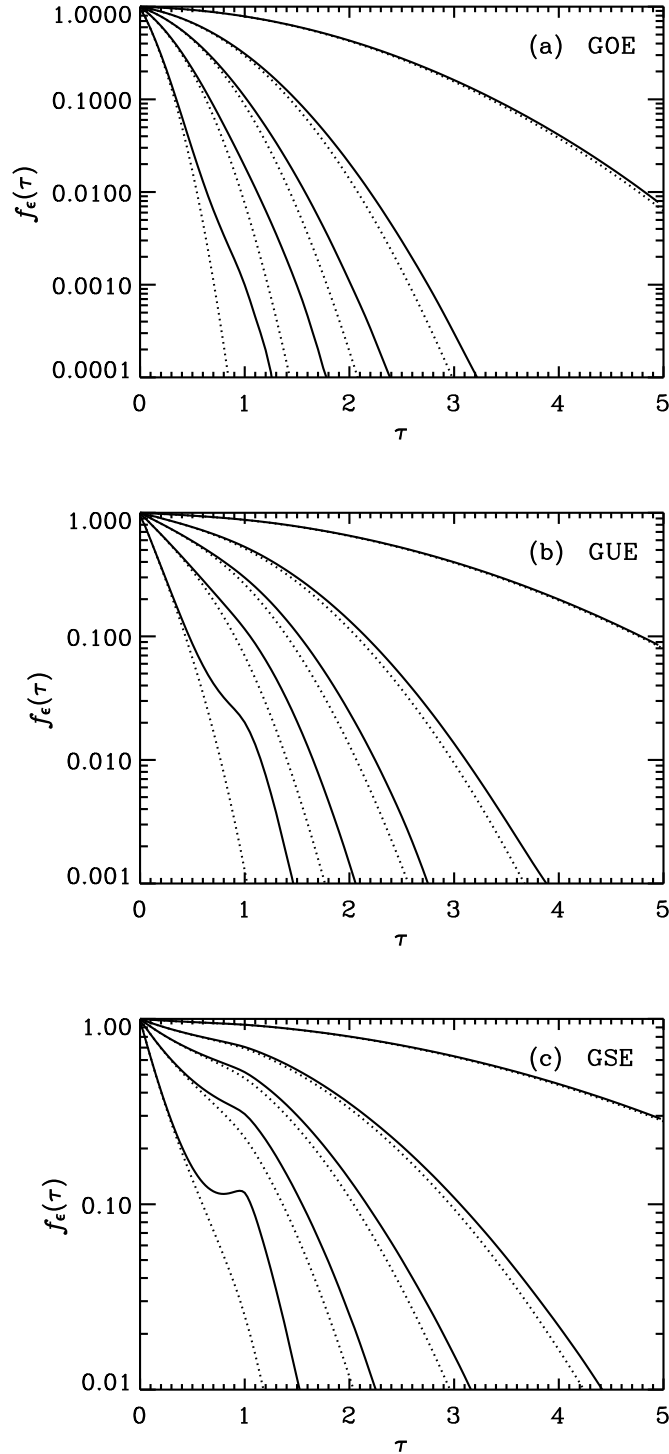
Figure 3.1: Fidelity amplitude $f_\epsilon(\tau)$ for the GOE (a), the GUE (b), and the GSE (c) for $\epsilon = 0.2$, 1, 2, 4 and 10. The solid lines show the results of the numerical simulations, and the dotted lines those of the linear response approximation. For the GOE and the GUE the numerical results are in agreement with the analytical results within the limits of the line strength.
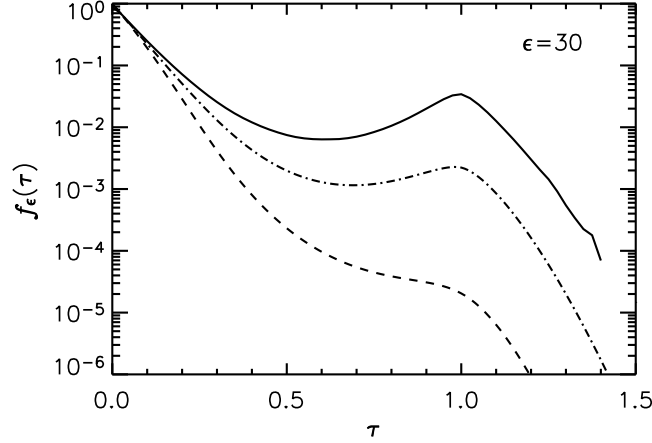
Figure 3.2: Fidelity amplitude $f_\epsilon(\tau)$ for $\epsilon = 30$. The dashed and dashed-dotted lines show the analytical results for the GOE and the GUE, respectively. The solid line corresponds to the numerical simulations for the GSE, reliable up to 10^{-3}. For the GOE and the GUE there is again a perfect agreement with the numerical results (not shown).

3.4 Debye-Waller factor

What is the origin of the surprising recovery? We believe that there is a simple intuitive explanation in terms of Dyson's Brownian motion model [Dys62]. Since the mean density of states is kept constant during the parameter change, the eigenvalues of H_ϕ may be written as $E_k^{(\phi)} = k + \delta_k^{(\phi)}$, where $\delta_k^{(\phi)}$ fluctuates about zero. A corresponding expression is obtained for the eigenvalues of H_0. Let us assume for the sake of simplicity that for strong perturbations the eigenvectors of the perturbed and unperturbed system are uncorrelated; details about this assumption are discussed in appendix 3.C. In this case we obtain from equation (3.16) for the ensemble average of the fidelity amplitude

$$f_\epsilon(\tau) \sim \frac{1}{N} \sum_{kl} \left\langle |R_{lk}|^2 \right\rangle e^{2\pi i \tau(k-l)} W \,, \tag{3.17}$$

where W is given by

$$W = \left\langle e^{2\pi i \tau(\delta_k^{(\phi)} - \delta_l^{(0)})} \right\rangle \approx e^{-(2\pi\tau)^2 \left\langle \delta^2 \right\rangle} \,. \tag{3.18}$$
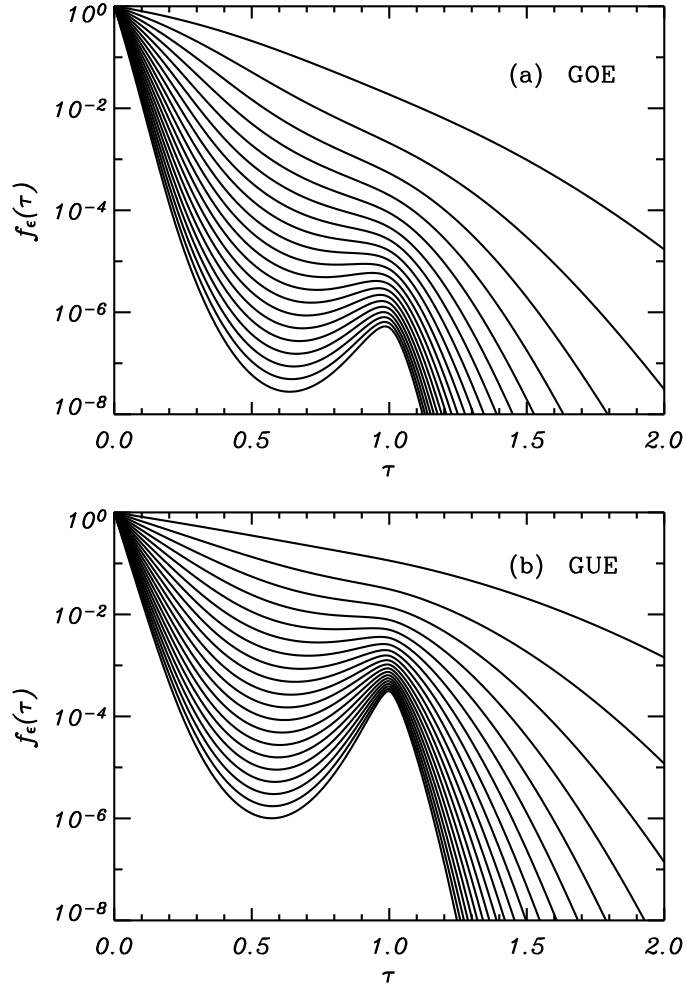
Figure 3.3: Fidelity amplitude $f_\epsilon(\tau)$ for perturbation strengths ϵ = $2, 4, \ldots, 40$ for (a) the GOE and (b) the GUE.

In the second step a Gaussian approximation was applied. Within the framework of the Brownian motion model $\langle \delta^2 \rangle$ is interpreted as the mean squared displacement of an eigenvalue from its equilibrium position. It is proportional to "temperature" T, which is just the reciprocal universality factor β, whence follows

$$W = e^{-\alpha \tau^2 T} \tag{3.19}$$

with some constant α. It follows from equation (3.17) that there is a revival of the fidelity at the Heisenberg time $\tau = 1$ decreasing with "temperature" proportional to $e^{-\alpha T}$. This is exactly the behavior illustrated in Figure 3.2.

There is a perfect analogy to the temperature dependence of X-ray and neutron diffraction patterns in solid state physics. Caused by lattice vibrations the v. Laue interference maxima decrease with increasing temperature according to the Debye-Waller factor

$$W_{\mathrm{DW}} = e^{-\beta g^2 T} , \tag{3.20}$$

where β is another constant, and g is the modulus of the reciprocal lattice vector characterizing the reflex (see e.g. appendix A of reference [Kit96]). This is our justification to call W a spectral Debye-Waller factor.

One may argue that due to equation (3.17) there should be revivals for all integer multiples of the Heisenberg time, which are not observed. This can be understood by considering the analogy between the spectral form factor

$$K(\tau) = \frac{1}{N} \sum_{n,m} e^{2\pi i (E_n - E_m)\tau} \tag{3.21}$$

and the structure factor in condensed matter,

$$S(\vec{k}) = \frac{1}{N} \sum_{n,m} e^{2\pi i \vec{q} \cdot \left(\vec{R}_n - \vec{R}_m \right)} \tag{3.22}$$

where the $\vec{R}_n$ are the positions of the atoms, and $\vec{q}$ is a point in the reciprocal lattice. (The factor 2π, absent in the usual definition of $S(\vec{q})$, has been introduced to be in accordance with the conventions used in this chapter.) For a perfect crystal $S(\vec{q})$ consists just of an array of delta functions at the positions of the reciprocal lattice vectors $\vec{g}$. In liquids and glasses these peaks are smeared out, and the structure factor depends only on the modulus q of $\vec{q}$. The typical liquid structure factor $S(q)$ is shown in figure 3.4; it starts at zero for $q = 0$, climbs up to two to three at the q value corresponding to the reciprocal atomic distance, oscillates about one with decreasing amplitude
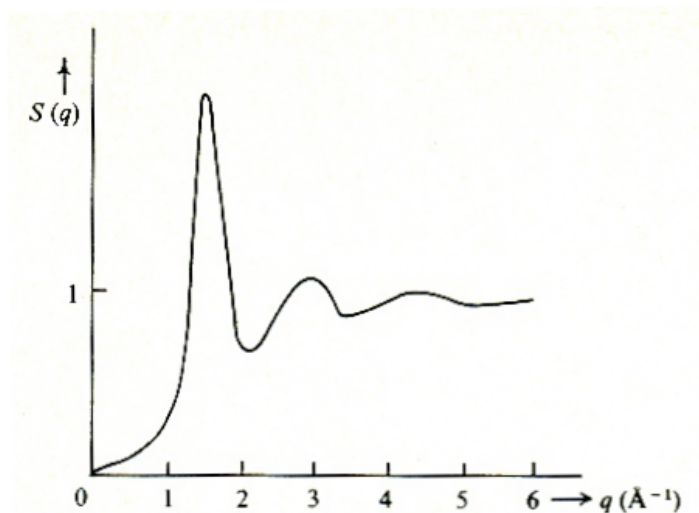
Figure 3.4: Typical liquid structure factor $S(q)$.
From Ziman: Models of disorder [Zim79]. Copyright 1979 by Cambridge University Press.

for larger q values, and approaches one in the limit $q \to \infty$ [Zim79]. There is a striking similarity with the spectral form factor $k(\tau)$ for the GSE, the eigenvalue "crystal" with the lowest available temperature (see figure 1.1). $k(\tau)$, too, starts at zero for $\tau = 0$, has a logarithmic singularity at the Heisenberg time $\tau = 1$, and approaches one for $\tau \to \infty$. The oscillatory behavior found in the structure factor, however, is absent in the spectral form factor. With increasing temperature the similarities disappear. Whereas for the structure factor the oscillations are just weakly damped with increasing temperature, for the spectral form factor the peak at the Heisenberg time vanishes completely for higher "temperatures", and only a slope continuity remains for the GUE, and an unstructured increase for the GOE.

Both spectral Debye-Waller factor and spectral form factor have thus in common that they do not show any structure at multiple integers of the Heisenberg time, in contrast to the corresponding condensed-matter quantities. The explanation is straightforward: Pauli's principle prevents the atoms from approaching too closely, whereas in the eigenvalue "crystal" a lower limit for the closest approach does not exit. Real crystals, even liquids, are just much more rigid than an eigenvalue "crystal". This is supported by calculations of the fidelity amplitude in the picket-fence model, where the eigenvalues of H_0 are equidistant and H_1 is taken from the GOE. For this system the similarity to a one-dimensional crystal is much closer than for the

Gaussian ensembles, and consequently fidelity recoveries have been observed for all integer multiples of the Heisenberg time [Gor04a].

This is also illustrated in appendix 3.A, where the fidelity amplitude of a picket-fence spectrum with a GUE perturbation is studied numerically.

3.A The picket-fence spectrum

The fidelity amplitude of the picket-fence spectrum with a GOE perturbation has been studied already in reference [Gor04a]. To evaluate the correlation integral (3.4) the authors also derived the two-point form factor for the picket-fence spectrum:

$$b_2^{\mathrm{pf}}(t) = 1 - \sum_{n \neq 0} \delta(t - n) \qquad (3.23)$$

Inserting this result and $\beta = 2$ for a GUE perturbation into the linear-response expression for the fidelity amplitude (3.3) yields

$$f_\epsilon(\tau) = \exp\left(-\epsilon \frac{\tau^2}{2} - [\tau]\left(\tau - \frac{[\tau] + 1}{2}\right)\right) \qquad (3.24)$$

In figure 3.5 the results of the random matrix simulations are shown for the picket-fence spectrum with GUE perturbation. They are compared with the exact results for the GUE (equation (3.13)) shown in the left column, and with the corresponding linear-response results.

As a direct consequence of the form factor $1 - b_2^{\mathrm{pf}}$, which is a sum of delta functions just like the structure factor of a perfect crystal, the fidelity amplitude shows kinks for all integer multiples of the Heisenberg time.

For small perturbation strengths ($\epsilon = 0.2$) the numerical results are still in good agreement with the linear-response approximation. With increasing perturbation strength we observe stronger and stronger deviations from this approximation, comparable to the deviations of the exact GUE result from the corresponding linear-response approximation. Only for small times τ we still observe a good agreement with linear response.

A conspicuous feature of the results is the fact that the fidelity amplitude of the picket-fence with GUE perturbation is always above the GUE curve with the same perturbation strength. In the linear-response approximation

the relative deviation can be written as

$$f_\epsilon^{\text{pf+GUE}}(\tau)/f_\epsilon^{\text{GUE}}(\tau) - 1 = \exp\left(-\epsilon \int_0^\tau \int_0^t \left(b_2^{\text{pf}}(t') - b_2^{\text{GUE}}(t')\right) \mathrm{d}t'\mathrm{d}t\right) - 1$$

$$(3.25)$$

This quantity is plotted in figure 3.6 for three different perturbation strengths. Again we see deviations for larger perturbation strengths. In particular the periodicity of the linear-response result is not reproduced exactly. In the numerical simulations we made sure that this deviation is no finite-size effect.

3.B   Finite-size effects

The exact expressions for the fidelity amplitude are valid in the limit $N \to \infty$. In this appendix we shall illustrate the deviations due to finite dimension N of the matrices.

This finite-size effect also depends on the strength of the perturbation. For small perturbation strengths ($\epsilon \ll 1$) it is sufficient to consider matrices of dimension $N = 100$. However, for larger perturbation strengths it becomes increasingly difficult to achieve good agreement with the asymptotic result.

Figure 3.7 shows the results of numerical random matrix simulations for the GUE, where the dimension of the matrices was varied from $N = 20$ to $N = 100$.

For $\epsilon = 10$ we find quite reasonable agreement with the asymptotic curve for $N = 100$, while for $\epsilon = 20$ the deviations are still quite noticeable for this size of the matrices, and we have to go to $N = 1000$ (not shown) to achieve an agreement within the limits of the line width.

3.C   Perturbation of eigenvectors

In section 3.4 we gave a simplified expression for the fidelity in the case of strong perturbations (see equation (3.17)). However, we had to make the assumption that the eigenvectors are so strongly affected by the perturbation that the matrix R as defined in equation (3.16) is basically a full random
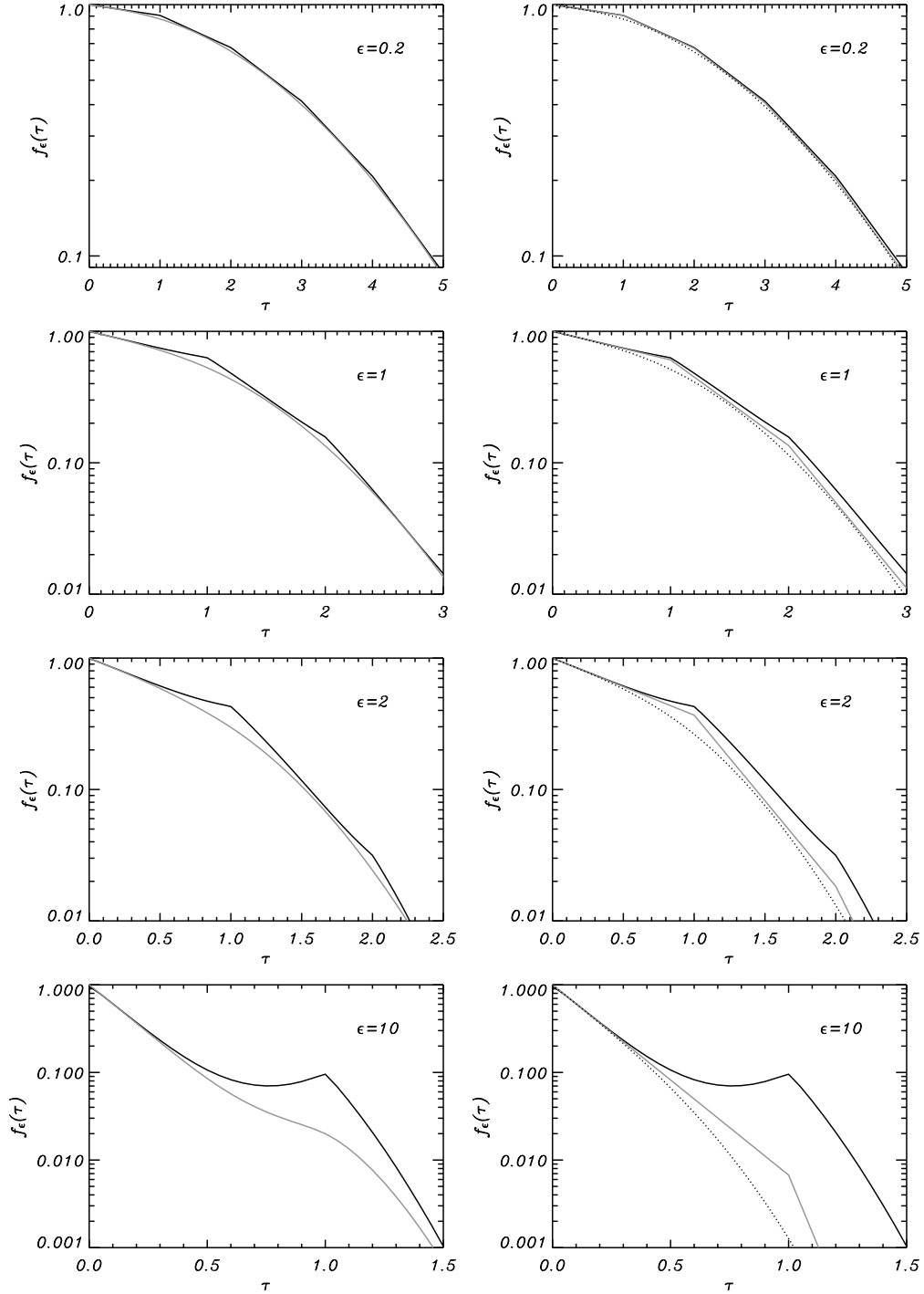
Figure 3.5: Fidelity amplitude for the picket-fence spectrum with GUE perturbation (black line). Left column: comparison with the exact result for the GUE (grey line). Right column: comparison with linear-response results for picket-fence + GUE (grey line) and GUE (dotted).

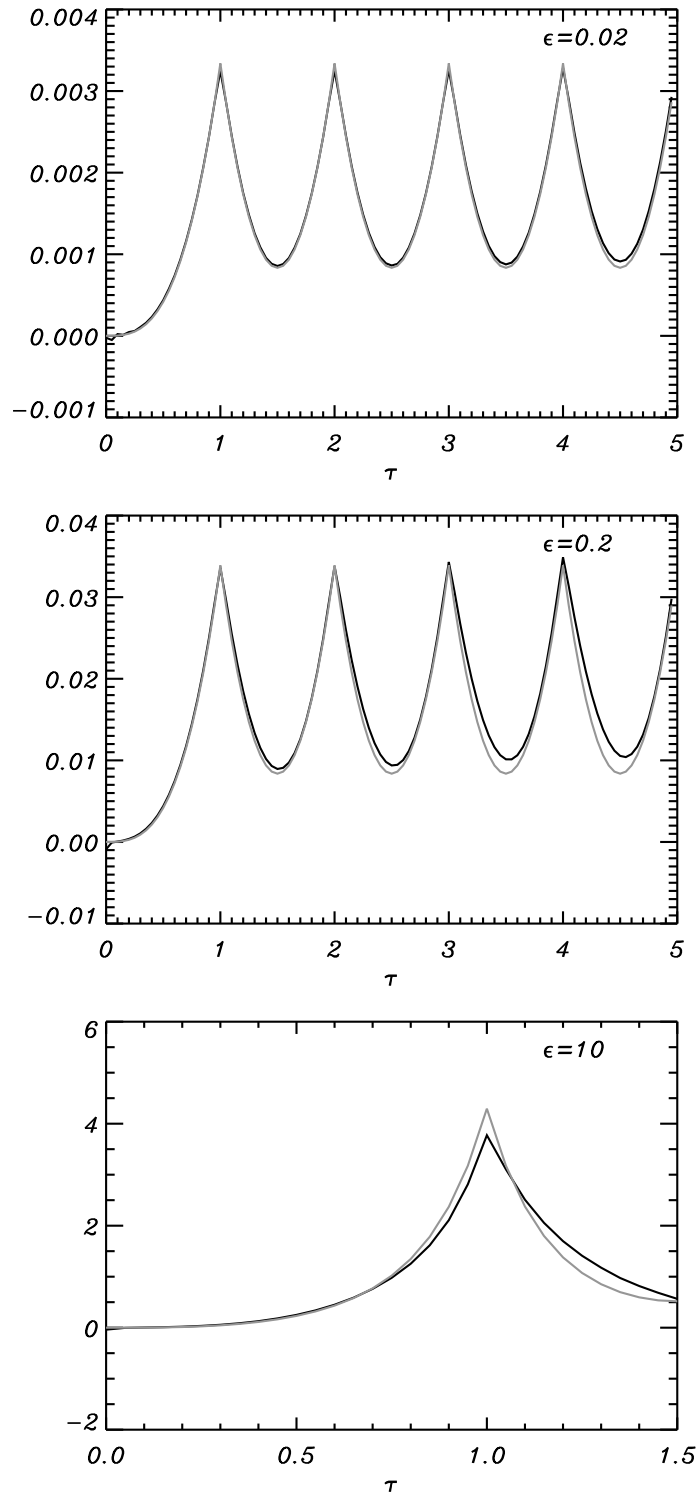Figure 3.6: Relative deviation of the fidelity amplitude for the picket-fence spectrum from the one for the GUE: $f_\epsilon^{\mathrm{pf+GUE}}(t)/f_\epsilon^{\mathrm{GUE}}(t) - 1$. Black line: numerical simulation for the picket-fence and analytical expression for the GUE. Grey line: linear-response result.

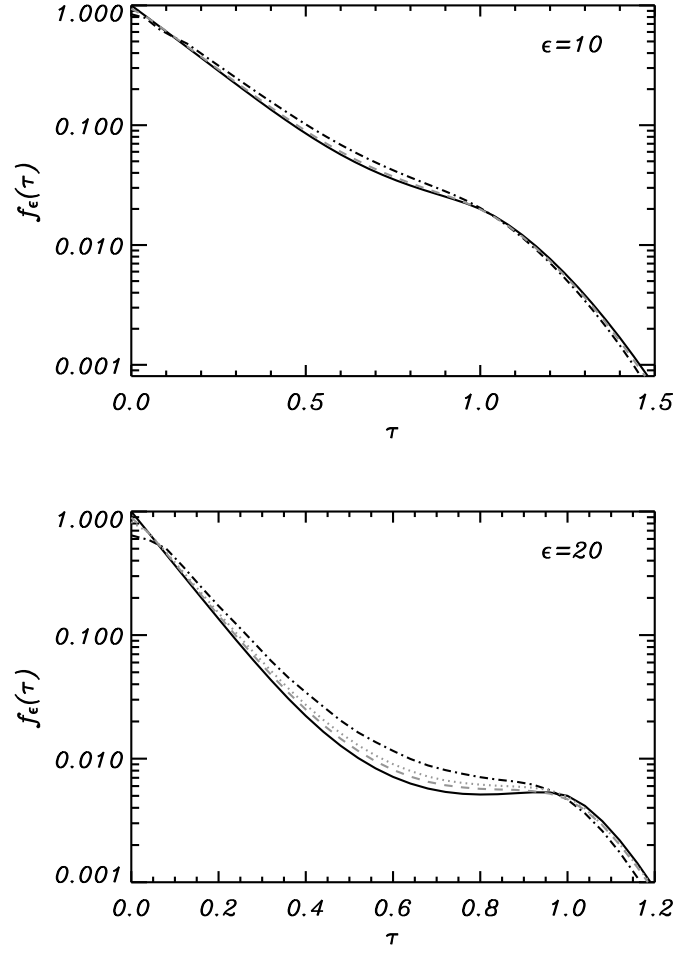Figure 3.7: Finite-size effect of the fidelity amplitude for the GUE. The solid line shows the exact result for $N \to \infty$. The dashed-dotted line corresponds to $N = 20$, the dotted line to $N = 50$ and the dashed line to $N = 100$.

matrix. Only in this case we can average separately over the $|R_{lk}|^2$ in equation (3.16).

To study under which conditions this assumption is valid, we calculated the matrix R for different perturbation strengths. The dimension of the Hamiltonians was $N = 200$.

Figure 3.8 shows a visualization of the results for $\epsilon = 10$, 20, 100, 200, 1000 and 2000. The grey-scale of the plots corresponds to the values of $|R_{lk}|^2$, white for zero and black for the maximal value.

In the perturbative regime the eigenvectors are only weakly affected by the perturbation, and thus the matrix R is close to the unit matrix. In this regime equation (3.17) does not describe the fidelity amplitude, but instead yields the form factor, multiplied by a Gaussian decay due to the fluctuations of the spectrum.

For larger perturbation strengths the matrix R becomes a banded matrix, which is illustrated in figure 3.8. For a given finite dimension N of the Hamiltonians, we can indeed reach the point, where the matrix R becomes a full matrix.

Instead of going to such huge perturbation strengths, we can also restrict the double sum in equation (3.17) to the center of the spectrum, and thus stay within the bandwidth of R. This was done for $N = 100$ and $\epsilon = 10$ to see whether equation (3.17) does indeed reproduce the recovery of the fidelity amplitude. The results are presented in figure 3.9. There was no exact agreement with the GUE results to be expected, because the double sum was not restricted to the extend necessary to stay within the bandwidth of R. Nevertheless, the simulations are able to reproduce the fidelity recovery at $\tau = 1$, which is even more pronounced than for the exact result.
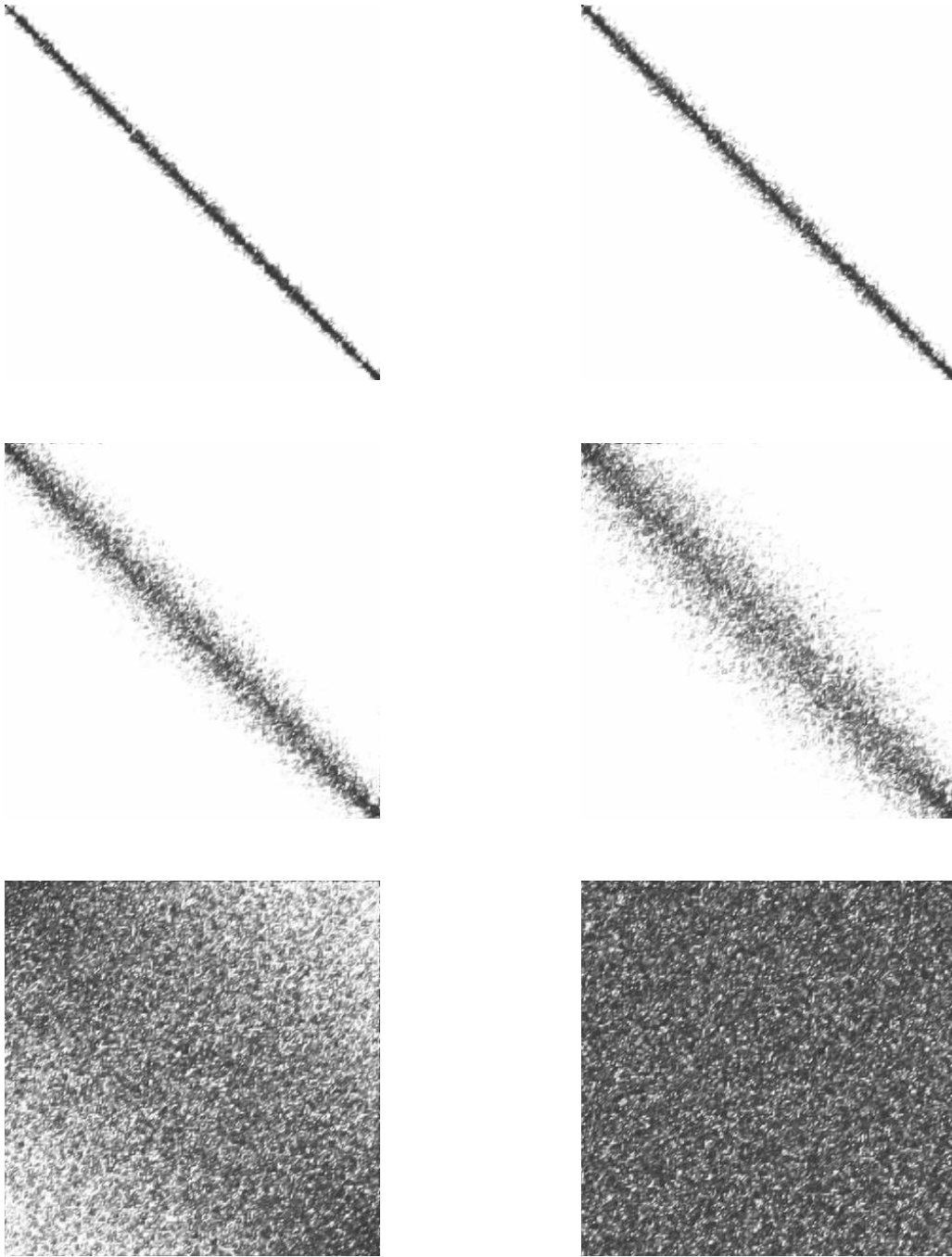
Figure 3.8: Visualization of the matrix R for $\epsilon = 10$, 20, 100, 200, 1000 and 2000. The grey-scale of the plots corresponds to the values of $|R_{lk}|^2$, white for zero and black for the maximal value.
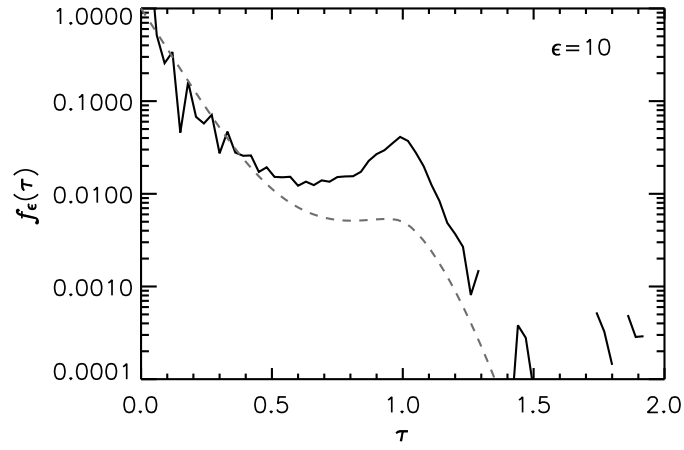
Figure 3.9: Simulation of equation (3.17) for $N = 100$ and $\epsilon = 10$. For comparison, the dashed line shows the exact result for the GUE.

Chapter 4

Fidelity amplitude of the scattering matrix in microwave cavities

4.1 Introduction

The analysis of the stability of dynamics under perturbations of initial conditions or the laws of motion was a central concern in a controversy between Loschmidt and Boltzmann [Los70]. A brief summary of these arguments can be found in [Žni04]. In quantum mechanics attention is usually focused on perturbations of the dynamics, as the evolution under the Schrödinger equation is always globally stable. The overlap of the perturbed and unperturbed time-evolution has become a benchmark for the reliability of quantum information processing, as well as for the stability analysis of integrable and chaotic motion [Per84]. Following the overview [Pro03] we shall use the term echo dynamics and define two unitary time evolution operators $U'(t)$ and $U(t)$ for the perturbed and unperturbed time evolution, respectively. The fidelity amplitude for some initial state $\psi(0)$ is defined as

$$f(t) = \langle \psi(0)| \, U^\dagger(t) \, U'(t) \, |\psi(0)\rangle \ , \tag{4.1}$$

and the fidelity by $F(t) = |f(t)|^2$. In other words, the fidelity amplitude is the cross-correlation function of an initial state $\psi(0)$ evolving under two different Hamiltonians.

The first realization of a quantum Loschmidt echo is due to Hahn [Hah50]. In

this key experiment the unperturbed dynamics is simply the free precession of an ensemble of nuclear spins in a not very homogeneous magnetic field. Hahn showed (and more clearly Carr and Purcell [Car54]) that it is possible to revert the dynamics by an appropriate short radio frequency pulse. However, the longer one waits with the application of the refocussing pulse, the weaker is the echo signal one obtains. This is due to residual interactions which are not reverted by the radio frequency pulse, the most prominent one being the spin-spin coupling. About forty years later Zhang *et al* [Zha92] demonstrated that it is also possible to revert the dynamics due to free precession and spin-spin coupling. This was a much more surprising achievement, because at the time the reversion is initiated one has a truly many body system which for many purposes can be considered as a thermally equilibrated gas. This success triggered many more experiments in NMR [Pas95, Lev98] as well as a series of experiments with classical waves [Der95, Ler04]. Finally there are some proposals [Gar97, Gor04b, Sch] and first experiments on trapped atoms [And03, Kuh03].

The purpose of this chapter is to present experiments for the stability of echo dynamics in flat electromagnetic cavities, using the equivalence of Helmholtz and stationary Schrödinger equation [Stö99]. We shall use two chaotic billiards, one with and the other without bouncing-ball states. The systems are perturbed by slightly changing one length in the billiards.

In the determination of the fidelity from equation (4.1) we face one problem. To map the wave function, an antenna has to be moved through the system (see e.g. chapter 2 of [Stö99]). This gives rise to another perturbation which may be of the same order of magnitude as the one caused by the shift of the wall. Thus a direct experimental determination of the fidelity amplitude is not feasible, or at least difficult. The situation is very common and has been encountered in previous experiments on NMR [Pas95, Lev98] and ultrasound propagation [Der95] as well. We therefore take a scattering point of view from the very beginning, and analyze the stability of the scattering matrix under perturbation of the time evolution. At the very end we ask ourselves, under which circumstances the result approximates standard fidelity.

Since the scattering matrix $S(E)$ is a time-independent quantity, we use its Fourier transform $\hat{S}(t)$ to obtain a time dependent signal, i.e. we consider $\hat{S}(t)$ as an evolution operator in the Hilbert space of the open channels of the system. Then, the obvious candidates for constructing signals analogous to the fidelity amplitude for closed systems, are cross-correlation functions of the same scattering matrix element of the perturbed and the unperturbed

system:

$$\hat{C}[S_{ab}, S_{ab}'^{*}](t) = \left\langle \hat{S}_{ab}(t) \, \hat{S}_{ab}'^{*}(-t) \right\rangle \, , \qquad (4.2)$$

where the brackets denote an average over an energy window, or an ensemble, or both. This quantity has the drawback, that it is dominated by the decay of the autocorrelations. We therefore define the scattering fidelity amplitude with the heuristic normalization as

$$f_{ab}(t) = \frac{\hat{C}[S_{ab}, S_{ab}'^{*}](t)}{\sqrt{\hat{C}[S_{ab}, S_{ab}^{*}](t)\hat{C}[S_{ab}', S_{ab}'^{*}](t)}} \, . \qquad (4.3)$$

In chaotic billiards this definition approaches the usual fidelity amplitude in the weak-coupling limit as we shall see later.

Here, we restrict ourselves to the measurement of $f_{ab}(t)$ for chaotic billiards, comparing our results with the linear response theory for closed systems developed by Prosen and coworkers [Pro03, Gor04a]. As it turns out, in our experiment we cannot reach situations where linear response theory would cease to be valid. In fact, we are restricted to the perturbative and the golden rule regime, but we are not able to go beyond that or approach the Lyapunov regime [Jal01] (this regime is known to be difficult to reach [ref Prosen]). Recently, the linear-response results by Gorin et al. have been extended to arbitrary perturbation strengths using supersymmetry techniques, predicting a revival of the fidelity at the Heisenberg time (see chapter 3 and reference [Stö04b]). But we shall see that for the interpretation of all experimental results presented in this chapter the linear-response approximation is completely sufficient.

In the next section we shall present the experimental setup, to proceed to a discussion of the relevant correlation functions of S-matrix elements in the third section. We then discuss the experimental results combined with an extensive discussion of the parameter characterizing our perturbation. The scaling properties of this parameter follow theoretical expectations very well, and interesting results about the effects of bouncing-ball states are found. We finally summarize our results and give an outlook on the perspectives of sensitivity of the S-matrix.
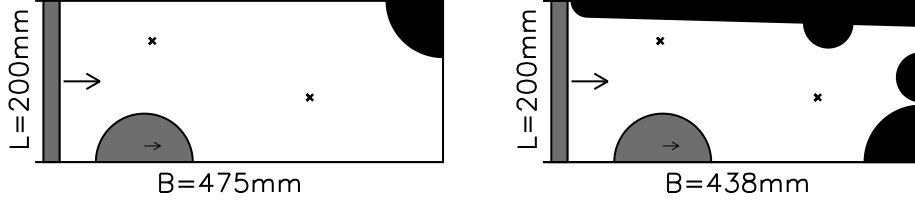
Figure 4.1: Geometry of the billiards. In the right billiard bouncing balls have been avoided by inserting additional elements (see text for dimensions).

4.2 Experimental setup

Since a detailed description of the general experimental technique can be found e. g. in [Kuh00], we concentrate on the aspects relevant in the present context. Reflection and transmission measurements have been performed in a flat microwave cavity, with top and bottom plate parallel to each other. The cavity is quasi-two-dimensional for frequencies $\nu < \nu_{max} = c/(2h)$, where h is the height of the billiard. In this regime there is a complete equivalence between the stationary wave equation and the corresponding stationary Schrödinger equation, where the z component of the electric field corresponds to the quantum mechanical wave function,

$$(\Delta + E)\,\Psi(x,y) = 0\;,\quad E = \left(\frac{2\pi\,\nu}{c}\right)^2\;,\tag{4.4}$$

with Dirichlet boundary conditions.

There were two antennas at fixed positions consisting of copper wires with a diameter of $1\,\text{mm}$, projecting $3\,\text{mm}$ into the resonator. An Agilent 8720ES vector network analyzer was used to determine the complete S-matrix. Measurements were taken in the frequency range from 3 to $17\,\text{GHz}$ with a resolution of $0.5\,\text{MHz}$.

The geometries of the billiards studied in this chapter are shown in figure 4.1. One billiard consisted of a rectangular cavity of length $L = 475\,\text{mm}$, width $B = 200\,\text{mm}$ and height $h = 8\,\text{mm}$, a quarter-circle insert of radius $R_1 = 70\,\text{mm}$, and a half-circle insert of radius $R_2 = 60\,\text{mm}$ placed at the lower boundary. The position of the latter was changed in steps of $20\,\text{mm}$ to get 15 different systems for the ensemble average. The perturbation of the system was achieved by moving the left wall in steps of $0.2\,\text{mm}$. For each of the 15 positions of the half-circle we performed 11 measurements for different

perturbation strengths.

The other billiard consisted of the same rectangular cavity, but with length $L = 438$ mm. It also shares the quarter-circle insert of radius $R_1 = 70$ mm, and on the lower boundary the half-circle insert of radius $R_2 = 60$ mm, which again was moved to realize an ensemble of 15 systems. Additional elements were inserted into the billiard to avoid bouncing-ball resonances: two half-circle inserts with radius $R_3 = 30$ mm, and a wedge on the upper boundary. Again the perturbation of the system was realized by moving the left wall in 10 steps of 0.2 mm.

The classical dynamics for the geometry of the billiards is dominantly chaotic, and since these are time-reversal invariant systems, we are going to compare the experimental results with random matrix predictions for the Gaussian orthogonal ensemble.

4.3 Measuring fidelity in a scattering setup

To describe the experiments adequately, it is essential to take into account that the microwave system is in fact an open system. The microwave field in the cavity has been constantly fed via one of the antennas, while the second antenna and, most importantly, the non-ideal billiard wall act as sinks. Scattering theory, originally developed in nuclear physics [Mah69], can be applied directly to open microwave billiards as well [Stö99, Sch03]. With H_{int} being the Hamiltonian of the closed billiard, and two antennas projecting into the resonator at the positions $\vec{r}_1$ and $\vec{r}_2$, the scattering matrix for the quantum equivalent can be written as:

$$S_{ab}(E) = \delta_{ab} - V^{(a)\dagger} \frac{1}{E - H_{\text{eff}}} V^{(b)} \qquad H_{\text{eff}} = H_{\text{int}} - (\text{i}/2) \, V \, V^\dagger \,, \qquad (4.5)$$

where $V^{(a)}$ is the column vector of V corresponding to the antenna at position $\vec{r}_a$. For antenna diameters small compared to the wavelength the matrix elements V_{ja} are proportional to $\psi_j(\vec{r}_a)$, the wave functions of the unperturbed system at the antenna positions.

We are now going to construct time dependent echo signals from appropriate correlation functions of scattering matrix elements obtained from stationary measurements. We shall define the "scattering fidelity" and discuss its relation to the usual fidelity of closed billiard systems. Consider a one parameter

family of closed billiard systems with the Hamiltonian $H_{\mathrm{int}}(\lambda)$. Let us denote two slightly different Hamiltonians by $H_{\mathrm{int}} = H_{\mathrm{int}}(\lambda_1)$ and $H'_{\mathrm{int}} = H_{\mathrm{int}}(\lambda_2)$, and the corresponding S-matrices as defined in (4.5) by S_{ab} and S'_{ab}. Their Fourier transforms read:

$$\hat{S}^*_{ab}(t) = \int \mathrm{d}E \; \mathrm{e}^{-2\pi\mathrm{i}\,E\,t} \; V^{(b)\dagger} \; \frac{1}{E - H^{\dagger}_{\mathrm{eff}}} \; V^{(a)} = 2\pi\mathrm{i} \; \theta(-t) \; V^{(b)\dagger} \; \mathrm{e}^{-2\pi\mathrm{i}\,H^{\dagger}_{\mathrm{eff}}\,t} \; V^{(a)}$$

$$\hat{S}'_{ab}(t) = \int \mathrm{d}E \; \mathrm{e}^{-2\pi\mathrm{i}\,E\,t} \; V^{(a)\dagger} \; \frac{1}{E - H'_{\mathrm{eff}}} \; V^{(b)} = -2\pi\mathrm{i} \; \theta(t) \; V^{(a)\dagger} \; \mathrm{e}^{-2\pi\mathrm{i}\,H'_{\mathrm{eff}}\,t} \; V^{(b)} \;,$$

where $\theta(t)$ is the Heaviside function. The vector $V^{(a)}$ describes the coupling of antenna a. For point-like coupling its matrix elements in the eigenbases of H_{int} and H'_{int} are given by $\sqrt{w_a} \; \langle\psi_j|\vec{r}_a\rangle$ and $\sqrt{w_a} \; \langle\psi'_j|\vec{r}_a\rangle$, respectively. The real parameters w_a give the norm of the channel vector $V^{(a)}$, and measure the strength of the coupling of the antennas to the closed billiard.

Following previous works on correlation functions of scattering matrices [Sch03, Gor02] we write the correlation function of the perturbed and the unperturbed system as

$$\hat{C}[S_{ab}, S'^{*}_{ab}](t) = \left\langle \hat{S}_{ab}(t) \; \hat{S}'^{*}_{ab}(-t) \right\rangle$$

$$= 4\pi^2 \; \theta(t) \left\langle w_a \, w_b \, \langle\vec{r}_b| \mathrm{e}^{2\pi\mathrm{i}\,H_{\mathrm{int}}\,t - \pi V V^{\dagger}\,t} \, |\vec{r}_a\rangle \, \langle\vec{r}_a| \, \mathrm{e}^{-2\pi\mathrm{i}\,H'_{\mathrm{int}}\,t - \pi V V^{\dagger}\,t} \, |\vec{r}_b\rangle \right\rangle \;.$$

$$(4.6)$$

In contrast to the usual definition of the fidelity, the projector $|\vec{r}_a\rangle \langle\vec{r}_a|$ separates forward and backward evolution. In chaotic billiards and if $|\vec{r}_a\rangle$ and $|\vec{r}_b\rangle$ are statistically independent, the energy-window or ensemble average converts the projector $|\vec{r}_a\rangle\langle\vec{r}_a|$ into the unit matrix. An additional average over antenna positions is not needed. We then obtain

$$\hat{C}[S_{ab}, S'^{*}_{ab}](t) = 4\pi^2 \; \theta(t) \; w_a \, w_b \, \langle\vec{r}_b| \, U_{\mathrm{eff}}(t) \, U'_{\mathrm{eff}}(t)^{\dagger} \, |\vec{r}_b\rangle \;, \qquad (4.7)$$

where $U_{\mathrm{eff}}(t)$ and $U'_{\mathrm{eff}}(t)$ are the sub-unitary propagators for H_{eff} and H'_{eff}, respectively. This formally looks like a fidelity amplitude for the effective Hamiltonians of the system. However, for vanishing perturbation, $\lambda = 0$, this quantity is not constant, it yields the autocorrelation function instead. This is the motivation to define the scattering fidelity f_{ab} for both diagonal and off-diagonal S-matrix elements via the relation

$$\hat{C}[S_{ab}, S'^{*}_{ab}](t) = f_{ab}(t) \, \hat{C}[S_{ab}, S^{*}_{ab}](t) \;. \qquad (4.8)$$

The thus defined scattering fidelity approaches the well known fidelity of the closed system in the limit of weak coupling to the antennas. In this case the wall absorption is the dominant effect leading to a resonance width Γ, which is approximately constant. As shown in chapter 2, the operator $VV^\dagger$ may then be replaced by the scalar Γ. Hence, we obtain from equation (4.7):

$$
\begin{aligned}
\hat{C}[S_{ab}, S_{ab}'^*](t) &= 4\pi^2 \,\theta(t)\, w_a\, w_b\, \mathrm{e}^{-2\pi\Gamma t}\, \langle\vec{r_b}|\, U_{\mathrm{int}}(t)\, U_{\mathrm{int}}'(t)^\dagger\, |\vec{r_b}\rangle \\
&= 4\pi^2 \,\theta(t)\, w_a\, w_b\, \mathrm{e}^{-2\pi\Gamma t}\, f(t) \\
&= f(t)\, \langle\hat{C}[S_{ab}, S_{ab}^*](t)\rangle\,.
\end{aligned}
\tag{4.9}
$$

This argumentation assumes that $\langle\psi_j|\vec{r_a}\rangle$ and $\langle\psi_j|\vec{r_b}\rangle$ are uncorrelated, i.e. $a \neq b$. The same result holds, however, for the case $a = b$ as well, provided that the $\langle\psi_j|\vec{r_a}\rangle$ are Gaussian distributed. Equation (4.9) is still true in the perturbative regime, i.e. as long as the perturbation does not change the wave functions. This can be shown in the context of the rescaled Breit-Wigner approximation [Sch03, Gor02], which is also valid for stronger coupling of the antennas. All experimental results presented below have been obtained in this regime.

4.4 Perturbation parameter for shifting of a billiard wall

In billiard systems the parameter variation is not due to a change of the Hamiltonian, but of the boundary condition. It was shown in chapter 5 of reference [Stö99] that both situations are equivalent for the case that the parameter variation in the billiard is due to a shift of a straight wall. In this case the matrix element of the equivalent perturbation is given by

$$
(H_1)_{nm} = l \int_0^L \frac{\partial\psi_n(0,y)}{\partial x} \frac{\partial\psi_m(0,y)}{\partial x} dy\,,
\tag{4.10}
$$

where l is the shift of the wall (in x-direction) and L is the length of the shifted wall. It follows for the perturbation strength:

$$
\begin{aligned}
\lambda^2 &= \left\langle [(H_1)_{nm}]^2 \right\rangle \\
&= l^2 \int_0^L dy_1 \int_0^L dy_2 \left\langle \frac{\partial\psi_n(0,y_1)}{\partial x} \frac{\partial\psi_n(0,y_2)}{\partial x} \right\rangle \left\langle \frac{\partial\psi_m(0,y_1)}{\partial x} \frac{\partial\psi_m(0,y_2)}{\partial x} \right\rangle
\end{aligned}
\tag{4.11}
$$

This is true for $n \neq m$, but again the result can be generalized easily to the case $n = m$. The averages can be calculated by means of Berry's random superposition of plane waves conjecture [Ber77a]. Close to a straight wall with Dirichlet boundary conditions, it yields

$$\langle \psi_n(x_1, y_1) \psi_n(x_2, y_2) \rangle$$
$$= \frac{1}{A} \left[J_0 \left(k \sqrt{(x_1 - x_2)^2 + (y_1 - y_2)^2} \right) - J_0 \left(k \sqrt{(x_1 + x_2)^2 + (y_1 - y_2)^2} \right) \right] \tag{4.12}$$

for the spacial correlation function, where A is the billiard area. Inserting this into equation (4.11) we obtain for the case $n \neq m$:

$$\begin{aligned}
\lambda^2 &= \left\langle [(H_1)_{nm}]^2 \right\rangle \\[2mm]
&= \frac{4k^2 l^2}{A^2} \int_0^L dy_1 \int_0^L dy_2 \frac{1}{(y_1 - y_2)^2} \left[J_0'(k|y_1 - y_2|) \right]^2 \\[2mm]
&= \frac{4k^2 l^2}{A^2} \int_0^L dy_1 \int_{-y_1}^{L - y_1} dy_2 \frac{1}{y_2^2} \left[J_0'(ky_2) \right]^2 \\[2mm]
&\approx \frac{4k^2 l^2}{A^2} \int_0^L dy_1 \int_{-\infty}^{\infty} dy \frac{1}{y^2} \left[J_0'(y) \right]^2 \\[2mm]
&= \frac{4k^2 l^2 L}{A^2} \frac{8}{3\pi}
\end{aligned}$$

The approximation works well for large wave numbers k. Since the mean level distance is normalized to one, we can insert $A = 4\pi$ for the area of the billiard, and finally end up with:

$$\lambda^2 = \frac{2L}{3\pi^3} k^3 l^2 \tag{4.13}$$

The variance of the diagonal matrix elements, $\left\langle [(H_1)_{nn}]^2 \right\rangle$, shows up to be twice as large. Exactly the same expression was obtained by Lebœuf and Sieber in a completely different approach [Leb99] using periodic orbit theory and the ergodicity assumption. It is interesting to note that two seemingly unrelated assumptions, one on the random wave superposition, and the other on the ergodicity of long periodic orbits, yield identical results.

4.5 Experimental results

4.5.1 Correlation function and fidelity amplitude

We start with a discussion of the Fourier transform of the correlation function $\hat{C}[S_{11}, S_{11}'^*](t)$ as given in equation (4.6). Figure 4.2 shows a logarithmic plot of $\hat{C}[S_{11}, S_{11}'^*](t)$ in comparison to the autocorrelation function $\hat{C}[S_{11}, S_{11}^*](t)$. The change of area and surface due to the shift of the billiard wall was taken into account by unfolding the spectra to a mean level distance of one. The frequency window of the Fourier transforms was $1\,\text{GHz}$ wide, and a Welch filter was applied. The correlation functions were averaged over an ensemble of 15 billiard geometries.

The autocorrelation follows the corresponding theoretical curve nicely, where the parameters for the wall absorption and the coupling of the antennas had been determined as described in chapter 2. Minor deviations from the theoretical curve can be attributed to the small number of levels in this frequency interval. Furthermore, small slits between the inserts of the billiards may act as additional decay channels. This is in contrast to the more or less homogenous absorption by the billiard wall, which can be described by infinitely many weak channels (see chapter 2).

With increasing time, the correlation function $\hat{C}[S_{11}, S_{11}'^*](t)$ deviates more and more from the autocorrelation function. This behavior can be described by a product of the autocorrelation function and the fidelity amplitude $f(t)$ of the closed system, thus confirming expression (4.9).

For the fidelity amplitude, we used the linear-response approximation derived by Gorin et al. [Gor04a],

$$f(t) = e^{-4\pi^2\lambda^2 C(t)} \,. \tag{4.14}$$

For the Gaussian orthogonal ensemble $C(t)$ is given by

$$C(t) = t^2 + \frac{t}{2} - \int_0^t \int_0^\tau b_2(\tau')\text{d}\tau'\text{d}\tau \,, \tag{4.15}$$

where $b_2(t)$ is the two-point form factor. Equation (4.14) describes the fidelity amplitude both in the perturbative regime, where the Gaussian decay is dominant, and in the Fermi golden rule regime, showing an initial exponential decay.
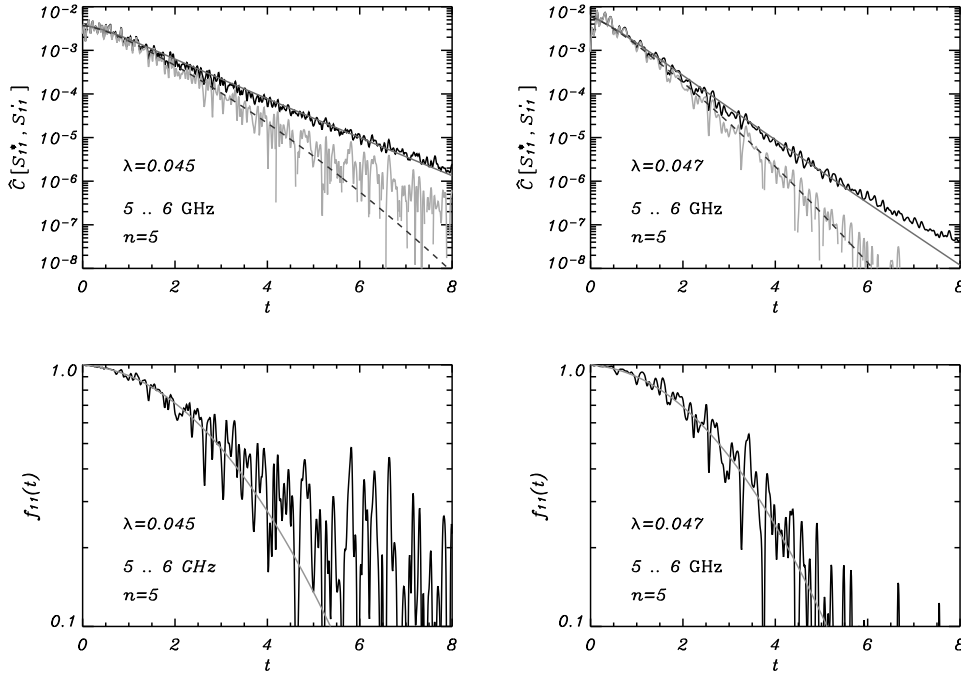
Figure 4.2: (top): Logarithmic plot of the correlation function $\hat{C}[S_{11}, S_{11}'^*]$ for the billiard with bouncing balls (left), and for the one without bouncing-balls (right). The experimental results for the autocorrelation are shown in black, while the correlation of perturbed and unperturbed system are shown in grey. The smooth solid curve corresponds to the theoretical autocorrelation function, and the dashed curve to the product of autocorrelation function and fidelity amplitude. (bottom): Logarithmic plot of the corresponding fidelity amplitudes. The smooth curve shows the linear-response result (4.14), where the perturbation parameter λ was obtained from the variance of the level velocities.

All fidelity amplitudes presented in the following have been obtained by dividing $\hat{C}[S_{ab}, S_{ab}'^*](t)$ by the geometric mean of the corresponding autocorrelation functions using equation (4.3). There are two reasons for dividing by the experimental autocorrelation function: there is no need to fit the autocorrelation function, and the influence of non-generic features in the Fourier transform is reduced.

The plots in the lower row of figure 4.2 show that this procedure works very well. For the frequency range shown in this figure, the perturbation strength was determined directly from the measured spectra via the variance of the level velocities. Thus we can describe the experimental results for the fidelity amplitude by the linear-response expression without any free parameter.

As expected, the billiard with bouncing balls shows systematic deviations from the random matrix prediction. Only at small times t we find good agreement. We therefore concentrate on the results of the billiard without bouncing balls in the following subsections.

4.5.2 Agreement with the linear-response prediction

In our experiment the values for the perturbation parameter λ vary from $\lambda = 0.01$ for $n = 1$ and $\nu = 3$ to $4\,\text{GHz}$ up to $\lambda = 0.5$ for $n = 10$ and $\nu = 17$ to $18\,\text{GHz}$. Figure 4.3 shows the fidelity amplitude for four different frequency windows. The perturbation parameter λ has been fitted to the experimental curves. To improve statistics, experimental results for f_{11}, f_{22} and f_{12} have been superimposed. The individual curves for these quantities were not discernible within the limit of error.

For small perturbation strengths, the linear term in the exponential is still close to one and thus we observe essentially a Gaussian decay of the fidelity amplitude, as seen in figure 4.3 for $\lambda_{\text{exp}} = 0.01$. With increasing perturbation strength the linear term is getting more pronounced, leading to an exponential decay for small times. However, for larger times the Gaussian decay again becomes dominant.

In the range accessible to our experiment (limited by the small ensemble) we find good agreement with the linear-response prediction of the random matrix model. For the strongest perturbation strength realized in our experiment, deviations of the linear-response result from the exact result for the Gaussian ensemble (see equation (3.15) of chapter 3) become noticeable only below
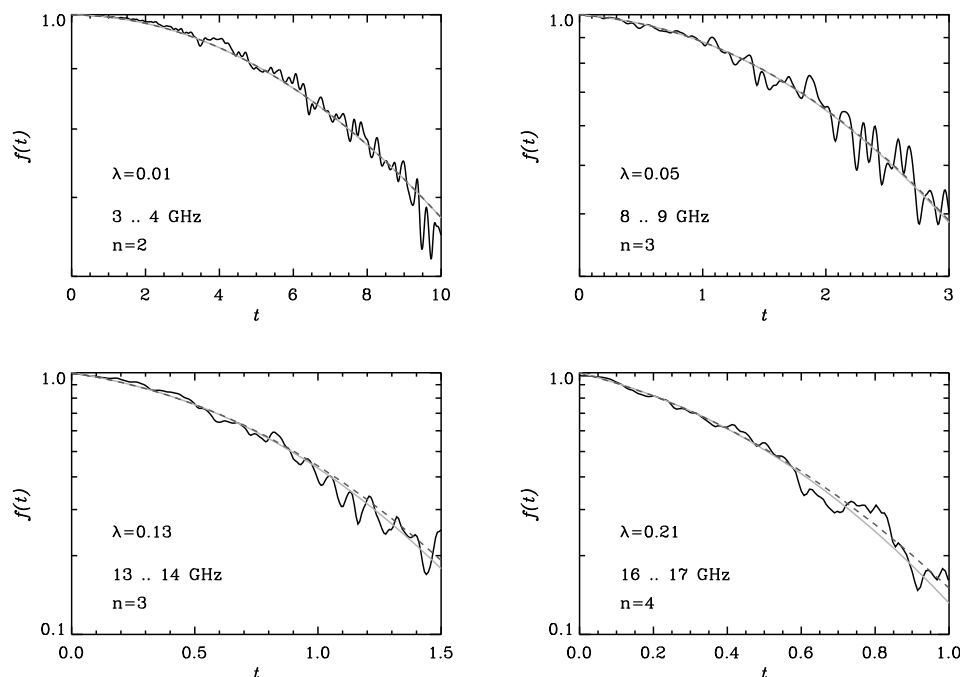
Figure 4.3: Fidelity amplitude of the billiard without bouncing balls, obtained by superimposing results for f_{11}, f_{22} and f_{12}. The smooth solid line shows the linear-response result (4.14), while the dashed line shows the exact result [Stö04b]. The perturbation parameter λ_{exp} has been fitted to each experimental curve.

10^{-1}. These deviations could not be detected by our experiment.

4.5.3   Scaling behavior of the perturbation strength

The experimental fidelity amplitude was studied for 10 different shifts of the billiard wall ($\Delta l = n \cdot 0.2\,\mathrm{mm}$, with $n = 1 \ldots 10$), and a frequency window of width $1\,\mathrm{GHz}$ was moved through the spectrum. The perturbation strength λ^2 entering the fidelity amplitude (4.14) was fitted to the experimental results.

Figure 4.4(a) shows the experimental perturbation strength λ^2_{exp} in dependence of the number of steps n for three different frequency regimes. We observe an excellent agreement with the scaling $\lambda^2 \propto n^2$ as predicted from equation (4.13). The experimental results for λ^2_{exp} in dependence of the frequency range shown in figure 4.4(b) do not look quite as nice as the previous
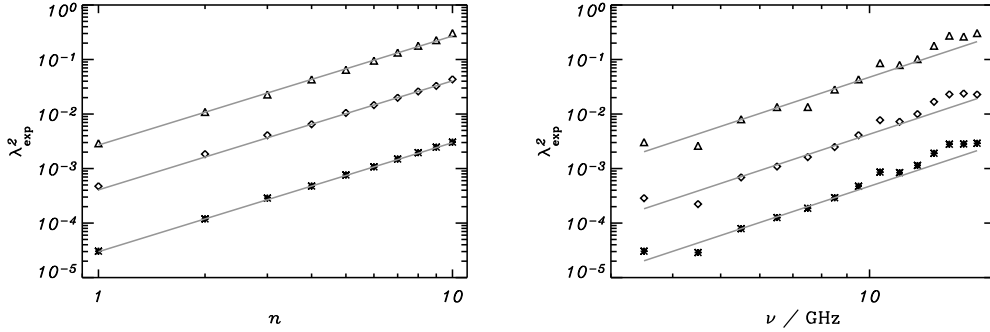
Figure 4.4: Perturbation strength λ^2 as a function of n (left), and as a function of frequency ν (right). The slopes of the straight lines are 2 in the left, and 3 in the right hand figure. The results are shown for the billiard without bouncing balls.

Figure 4.5: Average of the experimental fidelity amplitude on a rescaled axis $x = 4\pi^2\lambda^2 C(t)$. The solid line corresponds to $g(x) = \exp(-\alpha x)$ with $\alpha = \lambda^2_{\mathrm{exp}}/\lambda^2 = 0.36$.
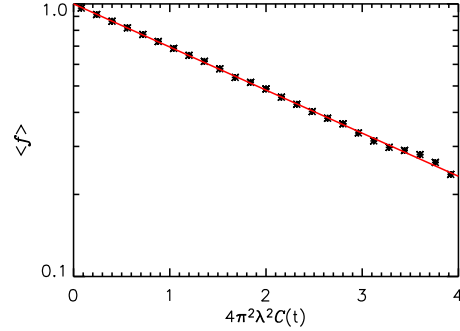
results, but they still confirm the scaling $\lambda^2 \propto \nu^3$.

The scaling of the perturbation strength works perfectly well over the whole parameter-space. This is illustrated in figure 4.5, where we averaged the experimental data of the fidelity amplitude on a rescaled axis $4\pi^2\lambda^2 C(t)$. However, the slope of the resulting curve is not in accordance with the prediction and yields a λ^2_{exp} deviating from the theoretical expectation of equation (4.13) by a factor of 0.36.

This deviation is caused by the fact that we are far from the semi-classical limit, for which the expression for λ^2 was derived. This is in accordance with numerical calculations for the Sinai billiard done by H. Schanz in Göttingen [Sch04b]. In cases where we determined the variance of level velocities directly from the measured spectra, we found the same deviation from equation (4.13). This shows that the experiment can be described in a self-consistent
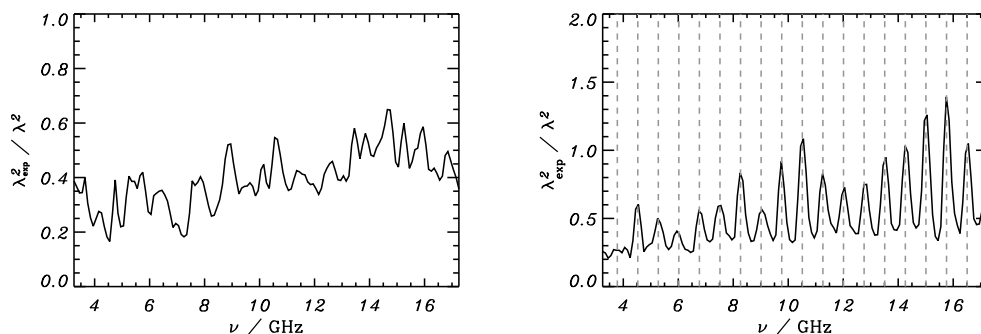
Figure 4.6: Correction factor $\lambda_{\mathrm{exp}}^2/\lambda^2$ as a function of frequency ν. Results are for the billiard without (left) and with bouncing balls (right). The dashed-dotted lines in the right hand figure correspond to the eigenfrequencies of the associated bouncing ball states.

way.

4.5.4   Influence of bouncing-ball modes

To study the frequency dependence of the perturbation strength in some more detail, we took a smaller frequency window of $0.5\,\mathrm{GHz}$ for the Fourier transform and moved it in finer steps through the whole frequency range.

In Figure 4.6 the ratio $\lambda_{\mathrm{exp}}^2/\lambda^2$ is plotted both for the billiard with and without bouncing balls, where λ^2 is the theoretical value of the perturbation strength according to equation (4.13). In the right hand plot, the frequencies of the (vertical) bouncing ball resonances are plotted as vertical lines, revealing the origin of the peaks in the frequency dependence of λ^2. The vertical bouncing ball remains nearly unaffected by the perturbation, but the unfolding of each spectrum takes the change of area into account, and thus introduces a constant drift to these resonances. This leads to a faster decay of the fidelity, thus resulting in the strong peaks visible in the figure.

Note that the result for the billiard without bouncing balls still shows fluctuations. The influence of the eigenmodes in the individual frequency window is thus visible for this billiard as well. However, there are no systematic peaks like the ones for the bouncing-ball modes.

4.6 Conclusions

It was shown in this chapter that the fidelity amplitude $f_{ab}(t)$ of scattering matrix elements S_{ab} is an easily accessible quantity which in the weak-coupling limit approaches the ordinary fidelity amplitude $f(t)$. It is stressed that it is not necessary to vary the antenna position for this purpose. This is essential, since every change of the latter gives rise to additional, hardly controllable perturbations. In integrable systems, however, an average over the antenna positions is indispensable to obtain $f(t)$. Therefore a determination of the fidelity $f(t)$ from the scattering fidelity $f_{ab}(t)$, as illustrated in this work for chaotic systems, is probably not feasible for integrable ones.

All results of this chapter could be described within the limits of the linear-response approximation [Gor04a], allowing a nice scaling of all data onto one single curve. Deviations of the decay constant of the such scaled fidelity from the predicted universal value could be quantitatively traced back to limits of the semiclassical approximation.

It remains an open question, whether the predictions of the exact theory described in chapter 3, in particular the conspicuous revival of the fidelity amplitude at the Heisenberg time, will be verified in a future experiment.

Chapter 5

Dielectric quadrupole billiards

5.1 Introduction

Disc-shaped dielectric cavities are of interest as compact, high-quality optical resonators to be used in micro-lasers and integrated optics applications [Cha96]. The waves can escape the dielectric cavity along its boundary, if the angle of incidence is below the critical angle of total internal reflection, $\sin \chi_c = 1/n$ (n the index of refraction of the dielectric, assumed to be surrounded by air). The modes with the longest lifetime (high-Q modes) are the so-called "whispering gallery modes" which circulate along the boundary and always stay above the critical angle. Actually, the waves can also escape the cavity above the critical angle, since for finite wavelengths the reflection coefficient at a curved interface does not have a critical angle, but instead is a smooth function of the angle [Hen02].

For dielectric discs with a circular boundary the emission pattern of the waves is homogenous in all directions due to the rotational symmetry. However, both for the design of micro-lasers, and for other optical applications, it is desirable to have a directed emission pattern or coupling to the outside. It was shown by Nöckel, Stone and Chang [Nöc94, Nöc97, Nöc00] that smooth deformations of the circular shape lead to anisotropic whispering gallery modes, which have a directional emission pattern with quality factors that are tunable by the degree of deformation.

For an ellipse the strongest emission is expected to be tangential at the points of highest curvature. The situation is more complex and thus more
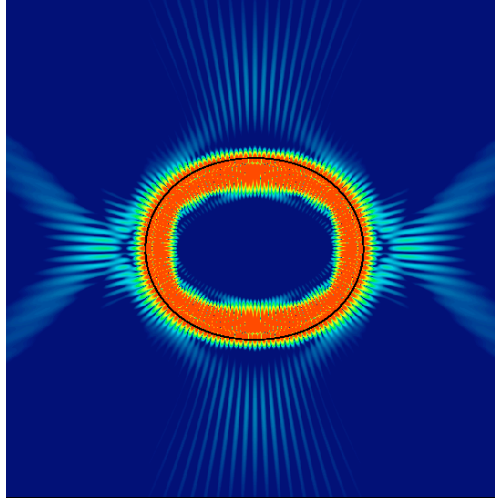
Figure 5.1: Whispering gallery mode[1] for the dielectric quadrupole billiard with $\epsilon = 0.10$, calculated numerically by J. U. Nöckel. The eigenmode shows a highly directional emission pattern.
[1] Published by J. U. Nöckel in the Yearbook of the MPI-PKS 1996-1997 (1998)

interesting for a quadrupolar deformation of the circle, described by

$$r(\phi) = 1 + \epsilon \cos 2\phi \, , \tag{5.1}$$

where ϵ is the deformation parameter. This deformation leads to a mixed phase space, i.e. partly regular and partly chaotic dynamics, which has important consequences for the internal dynamics and the emission behavior of the system.

Figure 5.1 was published by J. U. Nöckel in the Yearbook of the MPI-PKS 1996-1997 (1998) and shows a calculated eigenmode of the dielectric quadrupole billiard for $\epsilon = 0.10$. The index of refraction was $n = 1.55$, which yields for the critical angle $\sin \chi_c = 1/n \approx 0.65$. Obviously, the strongest emission does not occur at the points of highest curvature; still the emission pattern is highly directional.

Nöckel and Stone developed a ray model description for asymmetric resonant cavities, which tries to explain the emission of deformed whispering gallery modes as refractive escape of rays which are initially trapped by total internal reflection. Due to their chaotic dynamics, these rays diffuse chaotically until they reach the critical angle and leave the cavity.

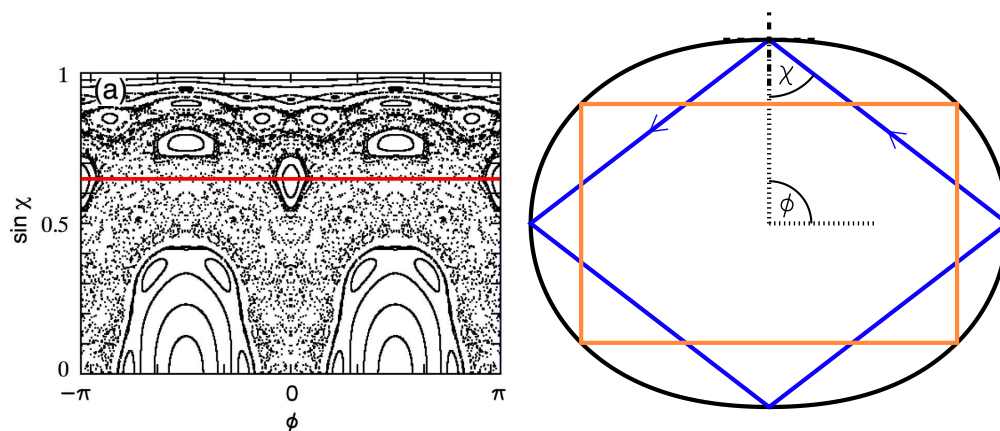Figure 5.2(left) shows the Poincaré section of the classical phase space for

Figure 5.2: (left) Poincaré section[1] for the quadrupole billiard with $\epsilon = 0.10$. (right) Shape of the quadrupole billiard, showing the stable diamond-shaped orbit, and the unstable rectangular orbit. χ is the angle of incidence of a ray with respect to the local normal.
[1] Published by J. U. Nöckel in the Yearbook of the MPI-PKS 1996-1997 (1998)

the corresponding quadrupole billiard. To obtain a Poincaré section only the points of reflection at the boundary are considered instead of the continuous trajectory. For each reflection point its position, parametrized by the angle ϕ, and the sine of the angle of incidence χ are plotted. This is illustrated in figure 5.2(right).

The presence of stable islands intersecting the line of the critical angle for a long time was assumed to be the main reason for the characteristic emission behavior of the quadrupole billiard, because the islands prevent the escape of rays at the points of highest curvature, $\phi = 0$ and $\phi = \pi$. This phenomenon was called "dynamical eclipsing" [Nöc96].

However, Schwefel *et al* found in a detailed study of the classical dynamics [Sch04c] that the characteristic emission behavior persists even for strong deformations, where the stability islands have already vanished. They found that the unstable manifold of the rectangular periodic orbit (see figure 5.2) dominates the short-time dynamics of the system, which determines the emission behavior. In section 5.2 this unstable manifold is discussed in detail.

Discussions with J. U. Nöckel have initiated our microwave experiments on dielectric quadrupole billiards, where the dielectric micro-disc is substituted by a teflon disc with $n = 1.44$. The experimental setup is described in section 5.3. We measured transmission spectra using two antennas, and obtained the

pulse propagation by a Fourier transform of these transmission spectra.

For each time step of the pulse propagation we determined the Poynting vector in the near-field. Thus we were able to study the directionality of the emission behavior. In laser experiments one usually examines the light intensity in the far-field to extract the same information.

To achieve a direct comparison to the internal dynamics of the classical system, we determined the Husimi distributions of the pulse propagation (see section 5.5). By averaging the Husimi distributions over four periods of the circulating wave-packets, we achieve a very clear picture of the internal dynamics in phase space. The results are presented in section 5.7. They show very good agreement with classical simulations for the long-time dynamics, and illustrate the importance of the unstable manifold for the emission behavior.

5.2 Hyperbolic fix-point

It is convenient to analyze the dynamics in terms of the Poincaré surface of section; then the dynamics from one reflection at the boundary to the next one can be described by a discrete map. We denote position and direction by $(s, u) = (\phi, \sin \chi)$, then the map which propagates the ray to the next position and direction is defined by

$$T : (s, u) \rightarrow (s_1, u_1) \, . \tag{5.2}$$

A point (s_p, u_p) of the surface of section is called a fixed point of order N, if it satisfies

$$T^N(s_p, u_p) = (s_p, u_p) \, . \tag{5.3}$$

It corresponds to a periodic orbit in real space.

The motion in the vicinity of a fixed point can be described by the monodromy or stability matrix M, which is a linearization of the map T^N around the fixed point:

$$M = \begin{pmatrix} \frac{\partial s_N(s,u)}{\partial s} & \frac{\partial u_N(s,u)}{\partial s} \\ \frac{\partial s_N(s,u)}{\partial u} & \frac{\partial u_N(s,u)}{\partial u} \end{pmatrix} \, , \tag{5.4}$$

where $(s_N, u_N) = T^N(s, u)$.

For Hamiltonian flows M is always an area-preserving map, i.e. $\det M = 1$. The eigenvalues of M can be either in complex conjugate pairs on the unit

circle or they are purely real and reciprocal to each other. If the eigenvalues of the monodromy matrix M are complex, the fixed point is stable (elliptic) and nearby points oscillate around the fixed point. The modulus of the eigenvalues is 1 in this case.

In the case of real eigenvalues the fixed point is unstable (hyperbolic). The eigenvector corresponding to the eigenvalue larger than 1 describes the unstable direction; in this direction deviations from the fixed point grow exponentially. The eigenvector belonging to the eigenvalue smaller than 1 describes the stable direction; in this direction deviations relax exponentially towards the fixed point. This behavior can be inverted by reversing time. Then deviations in the unstable directions relax towards the fixed point and deviations in the stable direction will increase.

By iterating a set of points on the unstable eigenvector (but still very close to the fixed point), we can visualize the unstable manifold of the fixed point which is defined as the set of points that approaches the fixed point arbitrarily closely as $t \to -\infty$. As the unstable manifold deviates further from the fixed point, it begins to have larger and larger oscillations. This is necessary to preserve phase space area while at the same time have exponential growth of deviations.

The short time dynamics in the vicinity of a hyperbolic fixed point is dominated by its unstable manifold, because a generic deviation will have at least some component along this unstable manifold. This was demonstrated e. g. in reference [Sch04c] for the quadrupole billiard.

While the quadratically-shaped periodic orbit in the circle billiard is stable, the quadrupolar deformation of the circle leads to the creation of a stable diamond-shaped orbit, and an unstable rectangular orbit (see figure 5.2).

Figure 5.3(top) shows the unstable manifold for the rectangular orbit in the quadrupole billiard with $\epsilon = 0.08$. The four fixed points (of order 4) are located at $\phi_p \approx 0.2\pi$, 0.8π, 1.2π and 1.8π, respectively. Their angle of incidence is $\chi_p = \pi/4$, yielding $\sin \chi_p \approx 0.707$. Thus they are just above the critical line of total internal reflection, $\sin \chi_c \approx 0.69$. The manifold encloses the stability islands of the diamond-shaped orbit.

For a larger deformation, $\epsilon = 0.13$, the stability islands of the diamond-shaped orbit have shrunk considerably, while the unstable manifold of the rectangular orbit has become very dominant (see figure 5.3(bottom)). The positions of the fixed-points are in this case $\phi_p \approx 0.18\pi$, 0.82π, 1.18π and

1.82π, respectively. Again, their angle of incidence is $\chi_p = \pi/4$, and thus $\sin \chi_p \approx 0.707$.

In section 5.5 we will compare these results of the classical billiard with the dynamics of the microwave system by means of Husimi distributions.
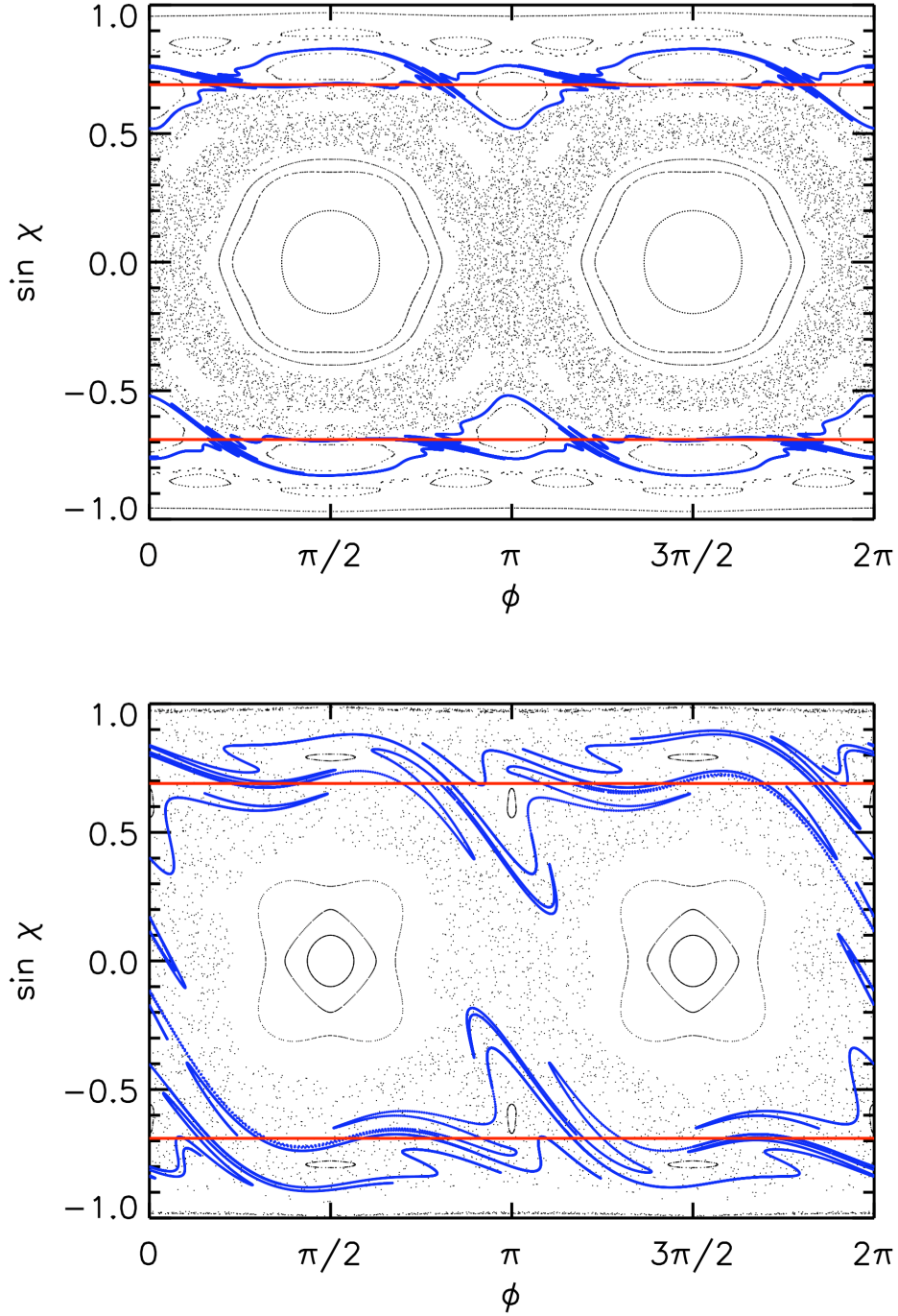
Figure 5.3: Poincaré section of the quadrupole billiard for $\epsilon = 0.08$ (top), and $\epsilon = 0.13$ (bottom). The unstable manifold of the rectangular orbit is shown as the dark curve. The horizontal line denotes the critical angle at $|\sin \chi_c| \approx 0.69$.

5.3 Microwave measurement

The microwave systems studied in this chapter consisted of a ground plate made of brass with rounded corners and dimensions $380 \times 260\,\text{mm}$. On this ground plate the teflon discs were fixed with an adhesive (see figure 5.4(left)). Teflon has an index of refraction of $n = 1.44$ and is particularly well suited for microwave studies, since it does not attenuate the microwaves noticeably. The height of the discs was $h = 8\,\text{mm}$, and their shape is given by equation 5.1, scaled with the mean radius $\bar{R} = 100\,\text{mm}$. We are going to present the results for two deformation parameters, $\epsilon = 0.08$ and $\epsilon = 0.13$.

The upper part of the system consisted of a brass plate supporting an antenna which could be moved with respect to the ground plate, thus allowing to scan the system. The top plate was large enough to cover the whole bottom plate for any position of the scanning antenna. In order to scan the system in the region of the teflon disc, we had to cut the antenna flush with the top plate (see figure 5.4(right)). This led to a noticeable reduction in the signal-to-noise ratio, but it was still possible to obtain reasonable results. More details on the set-up and the technique can be found in references [Kuh00, Sch01].

Figure 5.5 shows a typical transmission spectrum from the fixed antenna in the bottom plate ($x_a = -15\,\text{mm}$ and $y_a = -76.5\,\text{mm}$) to the movable antenna in the top plate. Up to $13\,\text{GHz}$ the spectrum shows a very regular spacing of resonances, because only the whispering gallery modes have long life-times. All other eigenmodes are not bound by total internal reflection and leave the teflon rather rapidly. At the edge of the ground plate the microwaves are reflected only very weakly.

The situation is different for frequencies above $13\,\text{GHz}$, where we observe a rich spectrum of sharp resonances. The reason is the difference in the index of refraction inside and outside the teflon disc. For frequencies below $\nu_c = c/(2nh)$ only TM_0 modes without z-dependence can be excited, because the wavelength is too large. In this case the billiard is called quasi-two-dimensional. For higher frequencies also TM_1 modes with one node in z-direction are allowed. Due to the higher index of refraction of teflon, this is already possible above $\nu_c \approx 13\,\text{GHz}$, while in air the cut-off frequency is $\nu_c \approx 18.75\,\text{GHz}$. Since in this intermediate frequency range between 13 and $18.75\,\text{GHz}$ the TM_1 modes in the teflon cannot couple to equivalent modes in the outside region, they are trapped inside the teflon irrespective of the angle of incidence at the teflon-air interface. Therefore the teflon disc acts like a closed system for these modes leading to the spectrum discussed above.

In the following we shall only consider the frequency range below 13 GHz, since we are interested in the teflon disc as an open system.
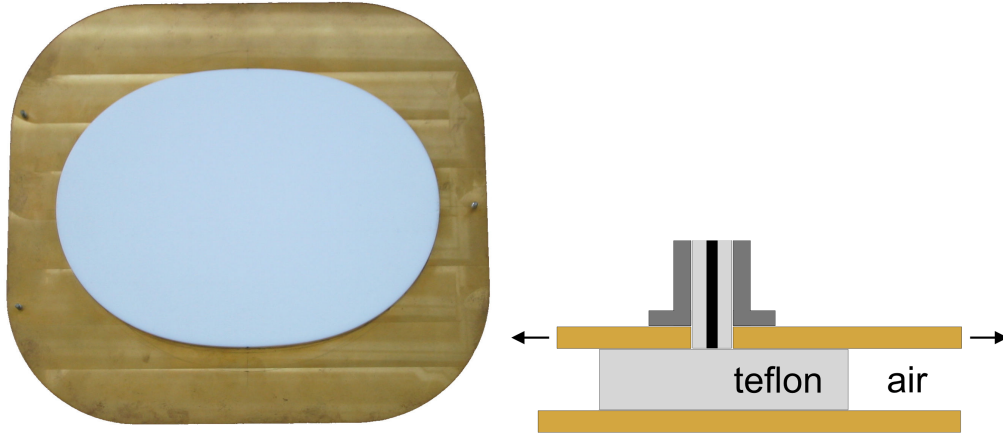

Figure 5.4: (left) Picture of the experimental setup showing a teflon disc mounted on the ground plate. (right) Illustration of the measuring technique showing the antenna that is cut down to the height of the top plate.
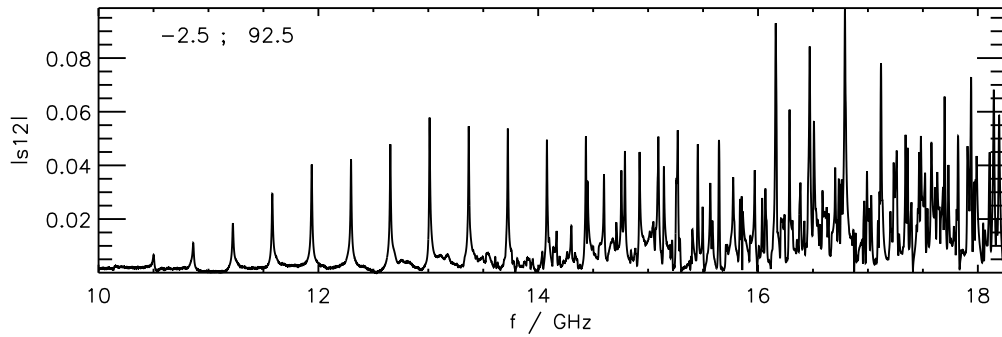

Figure 5.5: Transmission spectrum showing almost equidistant resonances below 13 GHz, which correspond to whispering gallery modes. Above 13 GHz the spectrum shows a multitude of sharp resonances.

5.4 Pulse propagation

The measurements presented in this chapter were done using an Agilent 8720ES vector network analyzer, yielding directly the scattering matrix S of the system. The non-diagonal elements of S are given by the transmission amplitudes S_{ij} between antennas i and j, and the diagonal elements by the reflection amplitudes S_{ii} at antennas i. Scattering theory yields a relation between the scattering matrix S and the Green function G of the billiard (see e. g. chapter 6 of reference [Stö99]):

$$S_{ij} = \delta_{ij} - 2\mathrm{i}\gamma G(r_i, r_j) \ . \tag{5.5}$$

For the case of isolated resonances the Green function can be written as

$$G(r_i, r_j, k) = \sum_n \frac{\psi_n(r_i)\psi_n(r_j)}{k^2 + k_n^2 + \frac{1}{2}\Gamma_n} \ , \tag{5.6}$$

where the complex widths Γ_n lead both to a broadening and to a shift of the resonances due to absorption and coupling to the antenna. Also the wavefunctions $\psi_n(r)$ are not exactly the ones of the closed system, but are slightly perturbed due to the presence of the antenna.

By a Fourier transformation of the transmission spectra $S_{ij}(\nu)$ we directly obtain the electromagnetic propagator

$$K(r_i, r_j, t) = \frac{1}{2\pi\mathrm{i}} \int G(r_i, r_j, k)\mathrm{e}^{\mathrm{i}\omega t}\mathrm{d}\omega \ , \qquad \omega = kc \ . \tag{5.7}$$

It is also possible to calculate the quantum-mechanical propagator by taking the corresponding dispersion relation into account.

Since in our experiment one antenna position was fixed, we did not measure the complete Green function. Thus the Fourier transform yields a pulse propagation with a fixed initial condition, corresponding to a circular wave that is emitted from the fixed antenna.

For each teflon billiard, transmission measurements were performed for altogether 2632 positions of the scanning antenna on a square grid with 5 mm resolution in the frequency range 0.5 to 18.24 GHz. In the following we will discuss in detail the results for the teflon quadrupole billiard with a deformation $\epsilon = 0.13$. Only at the end, we will compare these results with the ones for a smaller deformation, $\epsilon = 0.08$.
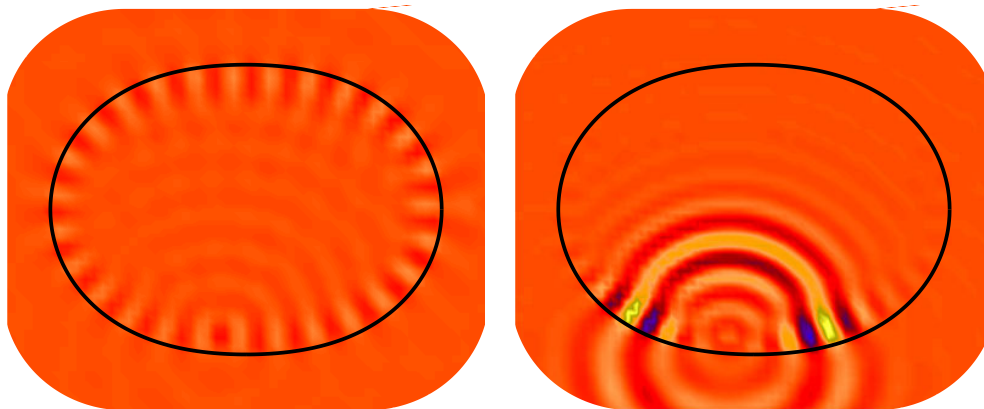
Figure 5.6:   (left) Whispering gallery mode at ν =   10.4 GHz for the quadrupole billiard with $\epsilon = 0.13$. (right) Pulse at $t = 405$ ps for the same billiard, as it spreads from the fixed antenna in the bottom plate.

Figure 5.6(a) shows a whispering gallery mode for the resonance at $\nu = 10.4$ GHz. The plot of the wavefunction has been obtained by averaging the transmission amplitude (including the phase) in a small frequency window for every position of the scanning antenna.

In figure 5.6(b) we present a snapshot of the pulse propagation at an early time $t = 404$ ps, when we still see the emergence of the circular pulse from the fixed antenna. Further we observe the different wavelengths inside and outside of the teflon, caused by the different indices of refraction. And already at this early stage, we see the development of two wave packets supported by the whispering gallery modes, one running clockwise the other counterclockwise along the boundary.

A sequence of snapshots of the pulse propagation is presented in figure 5.7. The first few time steps show a circular wave that is emitted from the fixed antenna. In the second row of the figure we see how most of the initial wave packet escapes the teflon disc due to a very steep angle of incidence. The remaining part of the pulse is almost completely concentrated on the two wave packets described above.
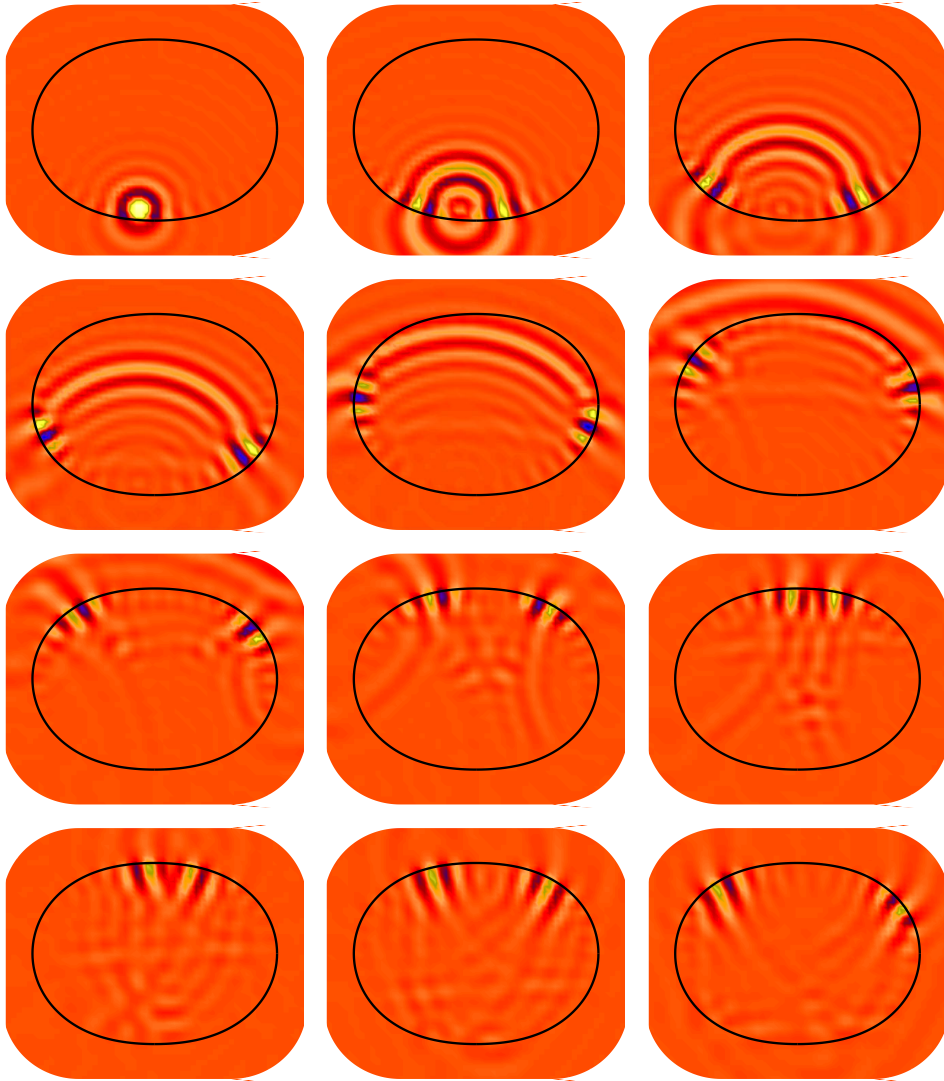
Figure 5.7: Sequence of the pulse propagation for some initial time steps: $t = 162, 324, \ldots, 1944$ ps.
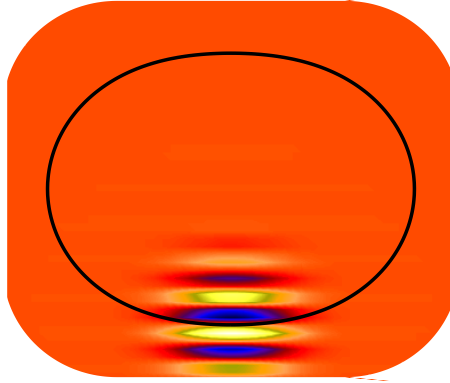
Figure 5.8: Gaussian wave packet for $\phi = \frac{3\pi}{2}$ and $\sin \chi = 0$.

5.5   Husimi distribution

To compare the internal dynamics of the teflon system to the classical Poincaré section, we shall use the Husimi distribution [Hus40, Bäc04, MB02], which is the quantum analogue to the classical phase-space probability density. It is the projection of a given quantum state $|\psi\rangle$ onto a coherent state of minimum uncertainty, i.e. a Gaussian wave packet.

Making the same restrictions on position and momentum as in the Poincaré section, where only reflections on the boundary of the billiard are considered, we can write the Husimi distribution as

$$H(\phi, \chi) = |\langle \phi, \chi | \psi \rangle|^2 \,, \tag{5.8}$$

where $|\phi, \chi\rangle$ denotes the coherent state at the boundary. In figure 5.8 such a coherent state is shown for $\phi = \frac{3\pi}{2}$ and $\sin \chi = 0$.

For the calculation of the Husimi distribution we only consider the region inside the teflon disc by setting the wavefunction on the outside to zero. The Husimi functions at dielectric interfaces have been studied in detail by Hentschel *et al* [Hen03], where they considered both inside and outside regions.

Instead of analyzing the Husimi distribution of eigenmodes, we shall consider the pulse propagation. The time evolution of phase space densities has been studied theoretically by, e.g., Manderfeld *et al* [Man01] and Prosen and Žnidarič [Pro02b].
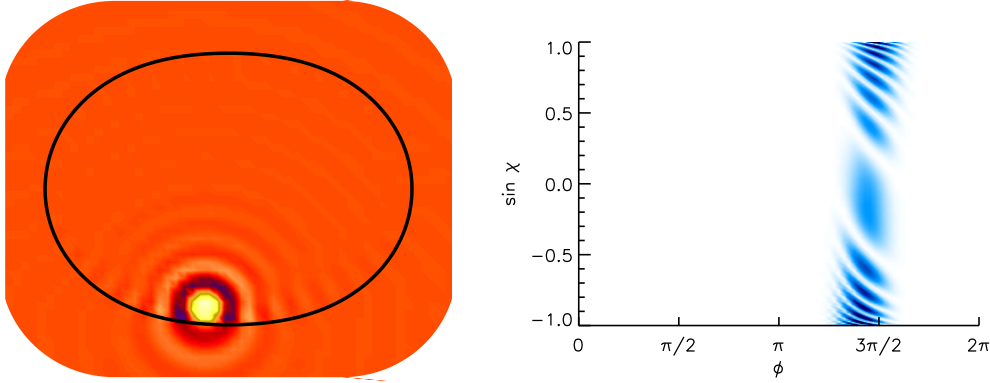
Figure 5.9: Pulse at $t = 162\,\mathrm{ps}$ (top), and its Husimi distribution (bottom). The pulse is well localized in space, but spreading in every direction.

Figure 5.9(a) shows the measured pulse at $t = 162\,\mathrm{ps}$, when the microwaves just start to spread from the antenna. Its Husimi distribution shows the pulse at a well localized position, but spreading in every direction.

5.6 Pulse sequence

While in laser experiments the directionality of the emission pattern was obtained by measuring the light intensity in the far-field, we are going to extract this information from the field distribution in the near-field of the teflon disc.

To this end we have to calculate the Poynting vector $\vec{S}(\vec{r})$ which describes the energy flow of an electromagnetic wave. In our case of a quasi-two-dimensional microwave system the Poynting vector reduces to

$$\vec{S}(\vec{r}) = \frac{c}{8\pi k} \left(E_z^*(\vec{r}) \nabla E_z(\vec{r}) \right) \ . \tag{5.9}$$

The Poynting vector is equivalent to the probability density current in quantum mechanics

$$\vec{j}(\vec{r}) = \frac{\hbar}{m} \mathrm{Im} \left(\psi^*(\vec{r}) \nabla \psi(\vec{r}) \right) \ . \tag{5.10}$$

A more detailed description of the Poynting vector in microwave systems is provided in references [Bar01, Vra02].

We are now going to take a closer look at later times of the pulse propagation, when only the two wave packets are remaining which are supported by the whispering gallery modes.

In figure 5.10 we present a sequence of the pulse at times $t = 4935$, 5097, 5744 and 6067 ps. In the left column the absolute square of the pulse is plotted with the Poynting vector in the near-field of the teflon disc. The right column shows the corresponding Husimi distributions. In addition the unstable manifold of the rectangular orbit is plotted.

The wave packet circulating counter-clockwise is always located in the upper part of the Husimi plot, corresponding to positive values of $\sin \chi$, while the other wave packet is located in the lower part. Even when the two wave packets interfere in position space, they are well separated in momentum space (see third row of figure 5.10).

The plot of the pulse at $t = 4935$ ps shows the point of strongest emission for the wave packet moving counter-clockwise. This is evident from the Poynting vector indicating a strong transport out of the teflon, tangentially to the disc's boundary. Also the intensity of the pulse gives an indication, accordingly. The corresponding Husimi plot gives even more insight into the emission behavior as it shows clearly that the transport to the outside happens along the unstable manifold of the rectangular orbit. Only at these points the pulse reaches far beyond the critical line of $\sin \chi = 0.69$, allowing an escape of the wave according to Fresnel's law. The plot for $t = 5097$ ps shows the wave packet on the left at the point of highest curvature. At this point the emission is rather weak. The Husimi plot shows that the wave packet stays well over the critical line at this position.

The last plot of figure 5.10 shows a point of strong emission for the clockwise moving wave packet. Again the corresponding Husimi plot indicates the importance of the unstable manifold.

In figure 5.11 we present for both billiards a histogram of the angle α of the Poynting vectors, weighted with their absolute value. This yields directly the directionality of the energy flow escaping the teflon disc. Horizontal vectors correspond to $\alpha = 0$ or $\alpha = \pm\pi$, while vertical vectors correspond to $\alpha = \pm\pi/2$. A tangential emission at the points of highest curvature would correspond to vertical Poynting vectors, but the histograms clearly show that the vertical directions are suppressed. Instead the highest emission is found at angles corresponding to the emission pattern shown in figure 5.1.
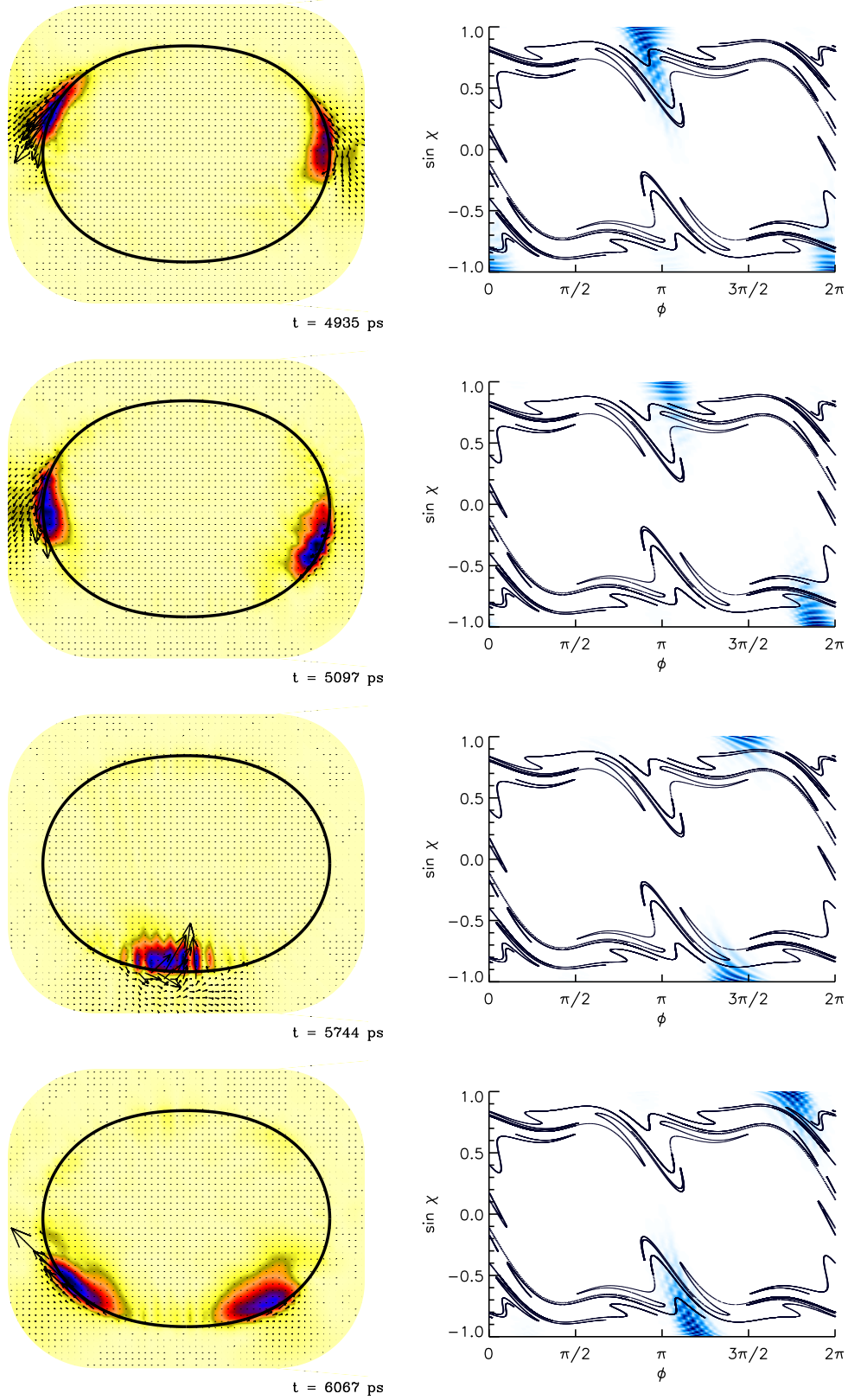
Figure 5.10: (left column) Absolute square of the pulse at $t = 4935$, 5097, 5744 and 6067 ps. In addition the Poynting vector is shown outside the teflon. (right column) Husimi distribution of the pulse at the same time steps. In addition the unstable manifold of the rectangular orbit is shown.
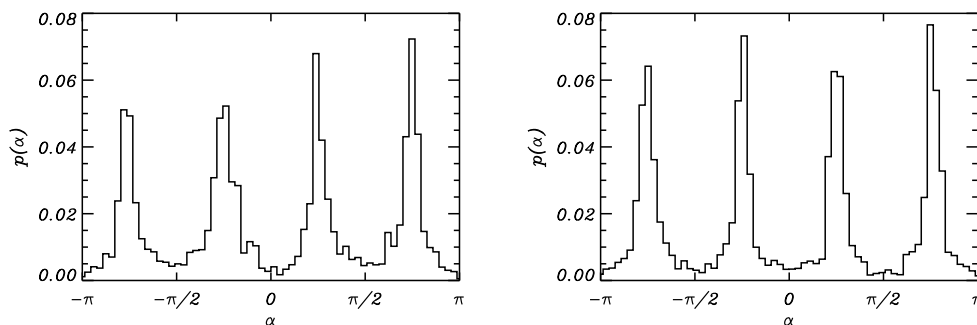
Figure 5.11: Histograms of the energy flow in dependence of the emission angle α. The histograms were averaged over four periods of the revolving wave packets. The deformation of the billiard was $\epsilon = 0.08$ (left), and $\epsilon = 0.13$ (right).

The histograms were averaged over four periods of the revolving wave packets, corresponding to the long-time average discussed in section 5.7. Only the Poynting vectors close to the boundary were taken into account, more precisely those between $1.02\,r(\phi)$ and $1.08\,r(\phi)$.

We observe a very high directionality of the Poynting vector for both geometries of the billiard. This is in accordance with measurements of the far-field intensities of micro-disc lasers [Sch04c].

5.7   Long-time dynamics

To simulate the microwave experiment in the ray-optical limit, we applied initial conditions matching those in the experiment. The rays are started at the position of the antenna and spread uniformly in every direction (see figure 5.12). Each ray i is associated with an amplitude a_i, which decreases with every reflection at the boundary according to Fresnel's law

$$a_{i,m+1} = a_{i,m}\, R(\chi_{i,m}) \qquad (5.11)$$

starting with an initial amplitude $a_{i,0} = 1$. For the reflection coefficient R the curvature corrections for curved dielectric interfaces [Hen02] were taken

into account, leading to

$$R = \left| \frac{\cos \chi + \mathrm{i}\mathcal{F}}{\cos \chi - \mathrm{i}\mathcal{F}} \right|^2 , \tag{5.12}$$

where

$$\mathcal{F} = \frac{\mathrm{i} \cos \eta}{n} \left[1 + \frac{1}{n^2 \sin^2 \chi} \left(\frac{K_{2/3}(z)}{K_{1/3}(z)} - 1 \right) \right] , \quad z = -\mathrm{i}kr_c \frac{\cos^3 \eta}{3 \sin^2 \eta} . \tag{5.13}$$

In this expression K_q are modified Bessel functions, $\eta = \arcsin(n \sin \chi)$ is the angle of refraction, r_c is the radius of curvature, and k is the wavenumber.

After a few iterations only those rays with a large angle of incidence still have high amplitudes. In figure 5.13 we show the Poincaré sections of the rays with amplitudes $a_{i,m} > 10^{-8}$ for $m > 30$. For the billiard with $\epsilon = 0.08$ all the rays remaining after 30 iterations are concentrated just above the unstable manifold. The escape due to small values of $|\sin \chi|$ then happens exclusively along this unstable manifold. It can barely be seen in the plot that the lighter dots for the simulation are also scattered on the lower part of the manifold. In the phase space of this billiard there is a separatrix preventing the rays from reaching larger values of $|\sin \chi|$.

The situation is similar for the billiard with $\epsilon = 0.13$. Here the separatrix is very close to $|\sin \chi| = 1$ and the unstable manifold has a rather complex structure. But still the ray simulation reproduces all its details and the escape clearly follows this manifold.

The classical ray-simulations are compared with the long-time dynamics of the microwave system. To this end the Husimi distributions of the pulses were averaged over four periods of the circulating wave packets. The results are presented in figure 5.14. The averaging greatly enhances the quality of the Husimi plots and we find a compelling agreement with the results of the classical simulation, both showing the importance of the unstable manifold of the rectangular orbit. However, there are differences due to the finite wave lengths in the microwave measurement. While in the classical simulations the separatrix prevented the rays from reaching larger values of $|\sin \chi|$, the waves can reach this region by dynamical tunneling. And for the same reason the wave dynamics can penetrate the stability islands, as seen in figure 5.14(top) for $\epsilon = 0.08$.
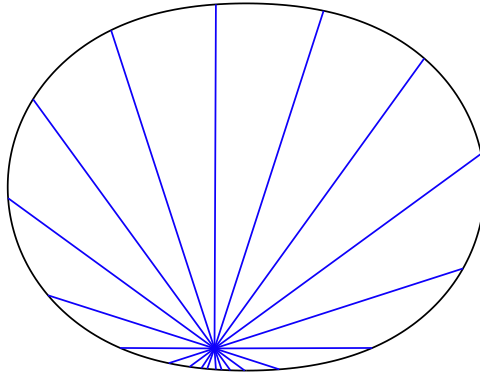
Figure 5.12: Initial conditions for the ray-simulations, starting at the position of the fixed antenna and spreading uniformly in every direction.

5.8   Conclusions

In our microwave experiments on dielectric quadrupole billiards we were able to reproduce the characteristic emission behavior found in the far-field intensities of microdisc lasers. We studied the Poynting vector close to the boundary of the teflon disc to obtain the directionality of the microwave emission.

We obtained the pulse propagation by a Fourier transfrom of the transmission spectra, and thus were able to concentrate on the long-time behavior.

The Husimi distributions of the pulse propagation provided a visualization of the internal dynamics of the system. By averaging the Husimi distributions over four periods of the circulating wave-packets, we achieve a very clear phase-space picture. The experimental results agree very well with classical simulations for the long-time dynamics, and clearly illustrate that the characteristic emission behavior is caused by the unstable manifold of the rectangular orbit.
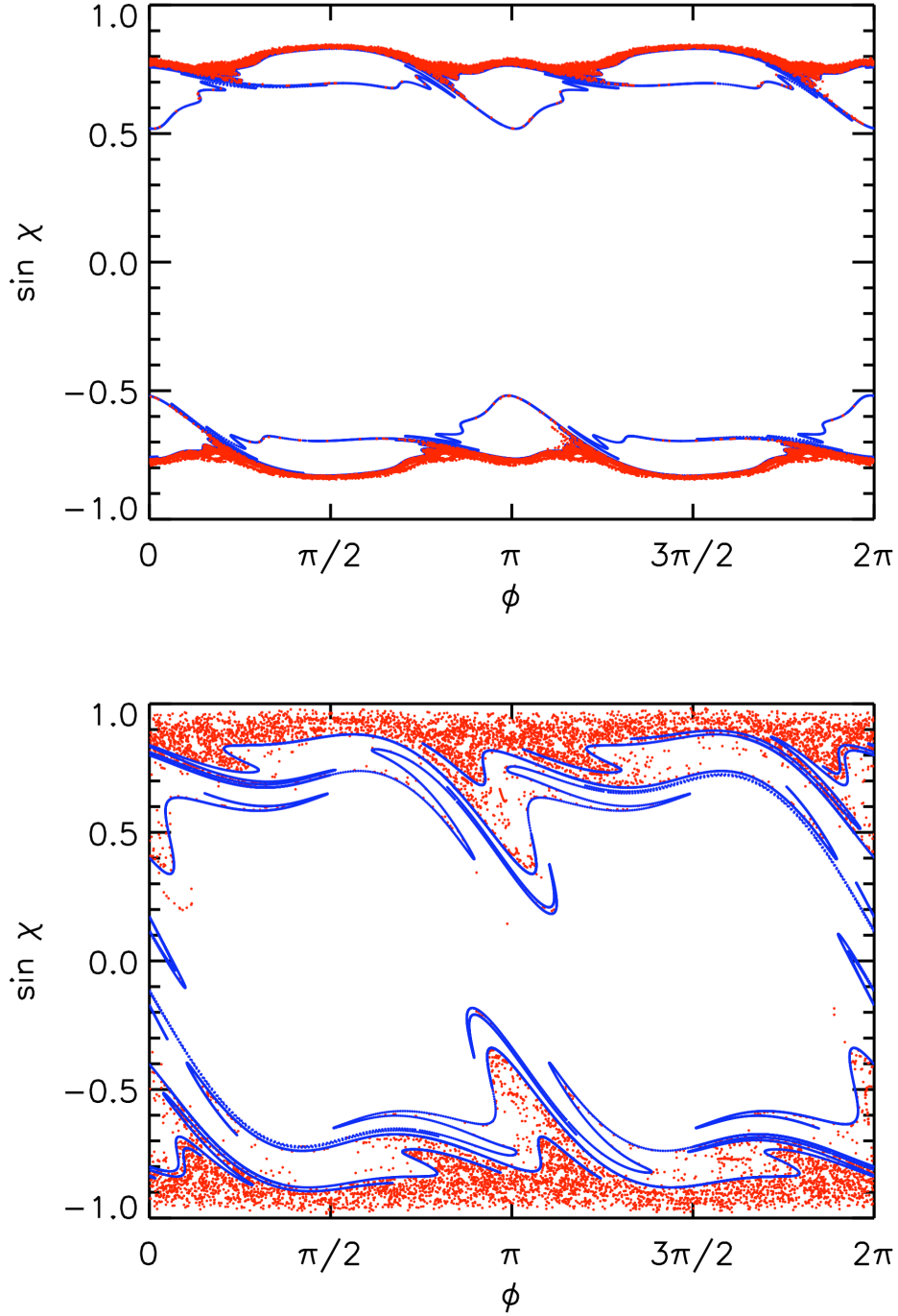
Figure 5.13: Poincaré sections of the ray-simulations for $\epsilon = 0.08$ (top), and $\epsilon = 0.13$ (bottom). Only rays with amplitudes $a_i(k) > 10^{-8}$ are plotted; the first 30 iterations have been omitted. For comparison, the unstable manifold of the rectangular orbit is plotted.
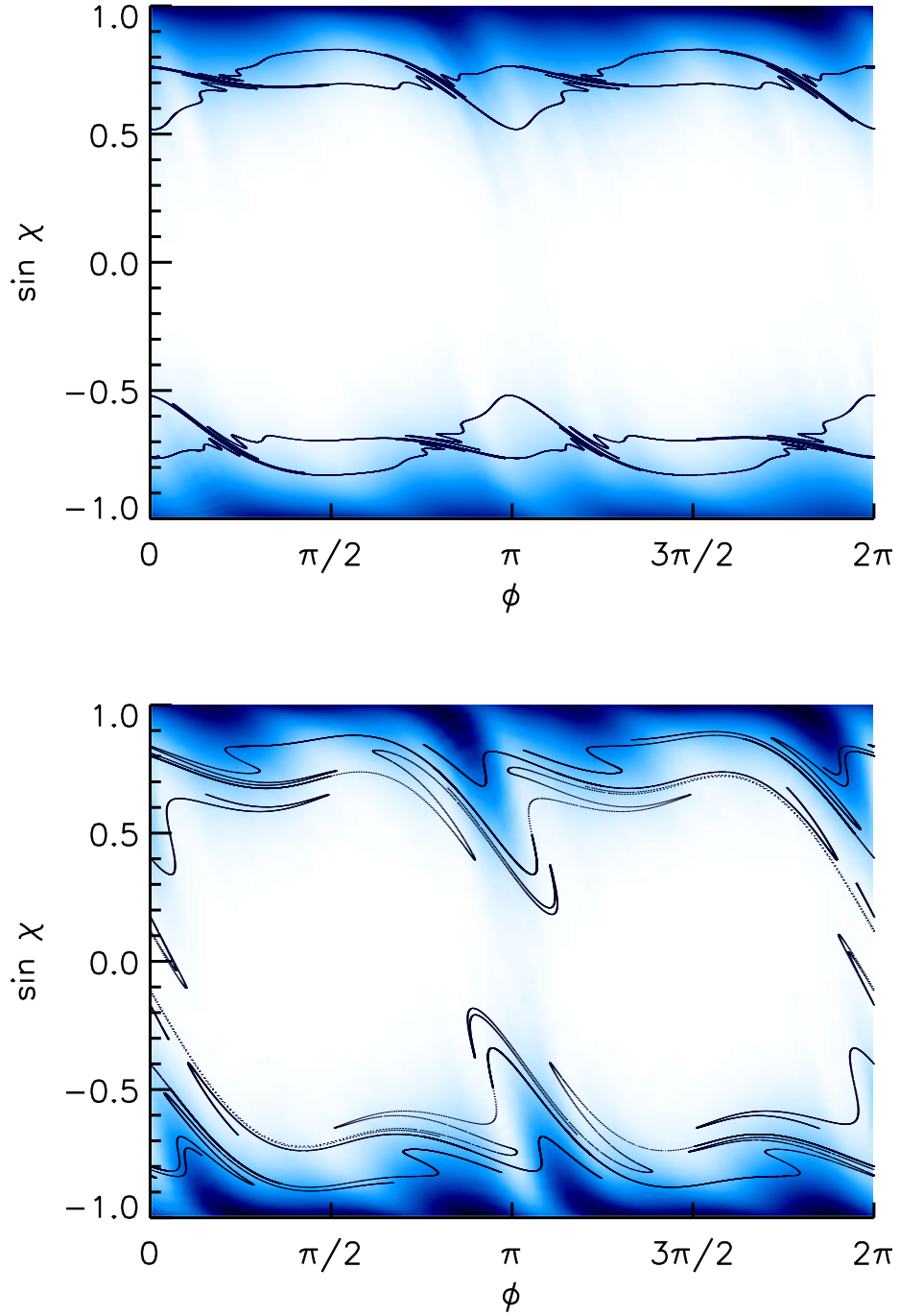
Figure 5.14: Average of the Husimi distributions over four periods of the circulating wave packets; for the quadrupole billiard with $\epsilon = 0.08$ (top), and with $\epsilon = 0.13$ (bottom). For comparison, the unstable manifold of the rectangular orbit is plotted.

Bibliography

[Abr61]   A. Abragam. *The Principles of Nuclear Magnetism.* University Press Oxford (1961).

[Alh98]   Y. Alhassid and Y. V. Fyodorov. The spectral autocorrelation function in weakly open chaotic systems: Indirect photodissociation of molecules. *J. Phys. Chem. A* **102**, 9577 (1998).

[Alt95]   H. Alt, H.-D. Gräf, H. L. Harney, R. Hofferbert, H. Lengeler, A. Richter, P. Schardt, and H. A. Weidenmüller. Gaussian orthogonal ensemble statistics in a microwave stadium billiard with chaotic dynamics: Porter-Thomas distribution and algebraic decay of time correlations. *Phys. Rev. Lett.* **74**, 62 (1995).

[Alt97]   H. Alt, H.-D. Gräf, T. Guhr, H. L. Harney, R. Hofferbert, H. Rehfeld, A. Richter, and P. Schardt. Correlation-hole method for the spectra of superconducting microwave billiards. *Phys. Rev. E* **55**, 6674 (1997).

[And03]   M. F. Andersen, A. Kaplan, and N. Davidson. Echo spectroscopy and quantum stability of trapped atoms. *Phys. Rev. Lett.* **90**, 023001 (2003).

[Bäc04]   A. Bäcker, S. Fürstberger, and R. Schubert. Poincaré Husimi representation of eigenstates in quantum billiards. *Phys. Rev. E* **70**, 036204 (2004).

[Bar01]   M. Barth. *Mikrowellen-Experimente zu Leveldynamik und Wirbelbildung.* Dissertation Philipps-Universität Marburg (2001).

[Ber77a] M. V. Berry. Regular and irregular semiclassical wavefunctions. *J. Phys. A* **10**, 2083 (1977).

[Ber77b] M. V. Berry and M. Tabor. Level clustering in the regular spectrum. *Proc. R. Soc. Lond. A* **356**, 375 (1977).

[Ber86] M. V. Berry and M. Robnik. Statistics of energy levels without time-reversal symmetrie: Aharonov-Bohm chaotic billards. *J. Phys. A* **19**, 649 (1986).

[Boh84] O. Bohigas, M. J. Giannoni, and C. Schmit. Characterization of chaotic spectra and universality of level fluctuation laws. *Phys. Rev. Lett.* **52**, 1 (1984).

[Bro81] T. A. Brody, J. Flores, J. B. French, P. A. Mello, A. Pandey, and S. S. M. Wong. Random-matrix physics: spectrum and strength fluctuations. *Rev. Mod. Phys.* **53**, 385 (1981).

[Car54] H. Y. Carr and E. M. Purcell. Effects of diffusion on free precession in nuclear magnetic resonance experiments. *Phys. Rev.* **94**, 680 (1954).

[Cas80] G. Casati, F. Valz-Gris, and I. Guarneri. *Lett. Nuov. Cim.* **28**, 279 (1980).

[Cas86] G. Casati, B. V. Chirikov, I. Guarneri, and D. L. Shepelyansky. Dynamical stability of quantum "chaotic" motion in a hydrogen atom. *Phys. Rev. Lett.* **56**, 2437 (1986).

[Cer02] N. R. Cerruti and S. Tomsovic. Sensitivity of wave field evolution and manifold stability in chaotic systems. *Phys. Rev. Lett.* **88**, 054103 (2002).

[Cha96] R. K. Chang and A. K. Campillo, editors. *Optical Processes in Microcavities*. World Scientific Singapore (1996).

[Der95] A. Derode, P. Roux, and M. Fink. Robust acoustic time reversal with high-order multiple scattering. *Phys. Rev. Lett.* **75**, 4206 (1995).

[Din02] J. Dingjan, E. Altewischer, M. P. van Exter, and J. P. Woerdman. Experimental observation of wave chaos in a conventional optical resonator. *Phys. Rev. Lett.* **88**, 064101 (2002).

[Dit91] F. M. Dittes, I. Rotter, and T. H. Seligman. Chaotic behaviour of scattering induced by strong external coupling. *Phys. Lett. A* **158**, 14 (1991).

[Dor90] E. Doron, U. Smilansky, and A. Frenkel. Experimental demonstration of chaotic scattering of microwaves. *Phys. Rev. Lett.* **65**, 3072 (1990).

[Dul01] H. R. Dullin and A. Bäcker. About ergodicity in the family of limaçon billiards. *Nonlinearity* **14**, 1673 (2001).

[Dys62] F. J. Dyson. A Brownian-motion model for the eigenvalues of a random matrix. *J. Math. Phys.* **3**, 1191 (1962).

[Eri66] T. Ericson and T. Mayer-Kuckuk. Fluctuations in nuclear reactions. *Ann. Rev. Nucl. Sci.* **16**, 183 (1966).

[Fra04] K. M. Frahm, R. Fleckinger, and D. L. Shepelyansky. Quantum chaos and random matrix theory for fidelity decay in quantum computations with static imperfections. *Eur. Phys. J. D* **29**, 139 (2004).

[Gar97] S. A. Gardiner, J. I. Cirac, and P. Zoller. Quantum chaos in an ion trap: The delta-kicked harmonic oscillator. *Phys. Rev. Lett.* **79**, 4790 (1997).

[Gor02] T. Gorin and T. H. Seligman. Signatures of the correlation hole in total and partial cross sections. *Phys. Rev. E* **65**, 026214 (2002).

[Gor04a] T. Gorin, T. Prosen, and T. H. Seligman. A random matrix formulation of fidelity decay. *New J. of Physics* **6**, 20 (2004).

[Gor04b] T. Gorin, T. Prosen, T. H. Seligman, and W. T. Strunz. Decoherence alias Loschmidt echo of the environment. Phys Rev A in press (2004). quant-ph/0405011.

[Guh98] T. Guhr, A. Müller-Groeling, and H. A. Weidenmüller. Random matrix theories in quantum physics: common concepts. *Phys. Rep.* **299**, 189 (1998).

[Haa01] F. Haake. *Quantum Signatures of Chaos. 2nd edition.* Springer Berlin (2001).

[Hah50] E. L. Hahn. Spin echoes. *Phys. Rev.* **80**, 580 (1950).

[Hen02] M. Hentschel and H. Schomerus. Fresnel laws at curved dielectric interfaces of microresonators. *Phys. Rev. E* **65**, 045603 (2002).

[Hen03] M. Hentschel, H. Schomerus, and R. Schubert. Husimi functions at dielectric interfaces: Inside-outside duality for optical systems and beyond (2003).

[Hus40]   K. Husimi. *Proc. Phys. Math. Soc. (Jpn.)* **22**, 246 (1940).

[Jac62]   J. D. Jackson. *Classical Electrodynamics*. Wiley New York (1962).

[Jal01]   R. A. Jalabert and H. M. Pastawski. Environment-independent decoherence rate in classically chaotic systems. *Phys. Rev. Lett.* **86**, 2490 (2001).

[Jos86]   R. Jost and M. Lombardi. Survey of correlation properties of polyatomic molecules vibrational energy levels using ft. analysis. In T. H. Seligman and H. Nishioka, editors, *Quantum Chaos and Statistical Nuclear Physics*. Lect. Notes Phys. 263. pp. 72–90. Springer Berlin (1986).

[Kit96]   C. Kittel. *Introduction to solid state physics*. Wiley New York (1996).

[Kuh00]   U. Kuhl, E. Persson, M. Barth, and H.-J. Stöckmann. Mixing of wavefunctions in rectangular microwave billiards. *Eur. Phys. J. B* **17**, 253 (2000).

[Kuh03]   S. Kuhr, W. Alt, D. Schrader, I. Dotsenko, Y. Miroshnychenko, W. Rosenfeld, M. Khudaverdyan, V. Gomer, A. Rauschenbeutel, and D. Meschede. Coherence properties and quantum state transportation in an optical conveyor belt. *Phys. Rev. Lett.* **91**, 213002 (2003).

[Leb99]   P. Lebœuf and M. Sieber. Universality in quantum parametric correlations. *Phys. Rev. E* **60**, 3969 (1999).

[Ler04]   G. Lerosey, J. de Rosny, A. Tourin, A. Derode, G. Montaldo, and M. Fink. Time reversal of electromagnetic waves. *Phys. Rev. Lett.* **92**, 193904 (2004).

[Lev86]   L. Leviandier, M. Lombardi, R. Jost, and J. P. Pique. Fourier transform: A tool to measure statistical level properties in very complex spectra. *Phys. Rev. Lett.* **56**, 2449 (1986).

[Lev98]   P. R. Levstein, G. Usaj, and H. M. Pastawski). Attenuation of polarization echoes in nuclear magnetic resonance: A study of the emergence of dynamical irreversibility in many-body quantum systems. *J. Chem. Phys.* **108**, 2718 (1998).

[Lew92]   C. H. Lewenkopf, A. Müller, and E. Doron. Microwave scattering in an irregular shaped cavity: random-matrix analysis. *Phys. Rev. A* **45**, 2635 (1992).

[Lom91]   M. Lombardi, J. P. Pique, P. Labastie, M. Broyer, and T. H. Seligman. Chaos in molecules by statistical Fourier transform spectroscopy. *Comments on Atomic and Molecular Physics* **25**, 345 (1991).

[Lom93]   M. Lombardi and T. H. Seligman. Universal and nonuniversal statistical properties of levels and intensities for chaotic rydberg molecules. *Phys. Rev. A* **47**, 3571 (1993).

[Lom94]   M. Lombardi, O. Bohigas, and T. H. Seligman. New evidence of GOE statistics for compound nuclear resonances. *Phys. Lett. B* **324**, 263 (1994).

[Los70]   J. Loschmidt. Private communication to Boltzmann, 1870. In C. Cercignani, editor, *Ludwig Boltzmann: The man who trusted atoms.* University Press New York (1970).

[Mah69]   C. Mahaux and H. A. Weidenmüller. *Shell-Model Approach to Nuclear Reactions.* North-Holland Amsterdam (1969).

[Man01]   C. Manderfeld, J. Weber, and F. Haake. Classical versus quantum time evolution of (quasi-) probability densities at limited phase-space resolution (2001).

[MB02]   J. A. Méndez-Bermúdez, G. A. Luna-Acosta, P. Šeba, and K. N. Pichugin. Understanding quantum scattering properties in terms of purely classical dynamics. two-dimensional open chaotic billiards (2002).

[Meh67]   M. L. Mehta. *Random Matrices, Statistical Theory of Energy Levels.* Academic Press New York (1967).

[Meh91]   M. L. Mehta. *Random Matrices. 2nd edition.* Academic Press San Diego (1991).

[Mel85]   P. A. Mello, P. Pereyra, and T. H. Seligman. Information theory and statistical nuclear reactions. I. general theory and applications to few-channel problems. *Ann. Phys. (N.Y.)* **161**, 254 (1985).

[Nöc94]   J. U. Nöckel, A. D. Stone, and R. K. Chang. Q-spoiling and directionality in deformed ring cavities. *Opt. Lett.* **19**, 1693 (1994).

[Nöc96]   J. U. Nöckel, A. D. Stone, G. Chen, H. L. Grossmann, and R. K. Chang. Directional emission from asymmetric resonant cavities. *Opt. Lett.* **21**, 1609 (1996).

[Nöc97]   J. U. Nöckel and A. D. Stone. Ray and wave chaos in asymmetric resonant cavities. *Nature* **385**, 45 (1997).

[Nöc00]   J. U. Nöckel. Laser aus dem Quantenchaos. *Physik in unserer Zeit* **31**, 79 (2000).

[Pas95]   H. M. Pastawski, P. R. Levstein, and G. Usaj. Quantum dynamical echoes in the spin diffusion in mesoscopic systems. *Phys. Rev. Lett.* **75**, 4310 (1995).

[Per84]   A. Peres. Stability of quantum motion in chaotic and regular systems. *Phys. Rev. A* **30**, 1610 (1984).

[Pin]   C. Pineda, R. Schäfer, T. Prosen, and T. H. Seligman. to be published.

[Por65]   C. E. Porter. *Statistical Theory of Spectra: Fluctuations.* Academic Press New York (1965).

[Pro02a] T. Prosen and T. H. Seligman. Decoherence of spin echoes. *J. Phys. A* **35**, 4707 (2002).

[Pro02b] T. Prosen and M. Žnidarič. Stability of quantum motion and correlation decay. *J. Phys. A* **35**, 1455 (2002).

[Pro03]   T. Prosen, T. H. Seligman, and M. Žnidarič. Theory of quantum Loschmidt echoes. *Prog. Theor. Phys. Suppl.* **150**, 200 (2003).

[Rob83]   M. Robnik. Classical dynamics of a family of billiards with analytic boundaries. *J. Phys. A* **16**, 3971 (1983).

[Sch]   W. P. Schleich and T. H. Seligman. to be published.

[Sch84]   H. G. Schuster. *Deterministic Chaos: An Introduction.* Physik Verlag Weinheim (1984).

[Sch01]   R. Schäfer, U. Kuhl, M. Barth, and H.-J. Stöckmann. Spectra and wavefunctions in a ray-splitting Sinai microwave billiard and their semiclassical interpretaion. *Foundations of Physics* **31**, 475 (2001).

[Sch02]   R. Schäfer, M. Barth, F. Leyvraz, M. Müller, T. H. Seligman, and
          H.-J. Stöckmann. Transition from gaussian-orthogonal to gaussian-
          unitary ensemble in a microwave billiard with threefold symmetry.
          Phys. Rev. E **66**, 016202 (2002).

[Sch03]   R. Schäfer, T. Gorin, T. H. Seligman, and H.-J. Stöckmann. Corre-
          lation functions of scattering matrix elements in microwave cavities
          with strong absorption. *J. Phys. A* **36**, 3289 (2003).

[Sch04a] R. Schäfer, T. Gorin, T. H. Seligman, and H.-J. Stöckmann. Fi-
          delity amplitude of the scattering matrix in microwave cavities
          (2004). To be published.

[Sch04b] H. Schanz. Numerical calculations for the sinai billiard: variance
          of level velocities at low energies. Private communication (2004).

[Sch04c] H. G. L. Schwefel, N. B. Rex, H. E. Tureci, R. K. Chang, A. D.
          Stone, T. Ben-Messaoud, and J. Zyss. Dramatic shape sensitivity
          of directional emission patterns from similarly deformed cylindrical
          polymer lasers. *J. Opt. Soc. Am. B* **21**, 923 (2004).

[Stö90]   H.-J. Stöckmann and J. Stein. "Quantum" chaos in billiards stud-
          ied by microwave absorption. *Phys. Rev. Lett.* **64**, 2215 (1990).

[Stö99]   H.-J. Stöckmann. *Quantum Chaos - An Introduction.* University
          Press Cambridge (1999).

[Stö02]   H.-J. Stöckmann, E. Persson, Y.-H. Kim, M. Barth, U. Kuhl, and
          I. Rotter. Effective Hamiltonian for a microwave billiard with at-
          tached waveguide. *Phys. Rev. E* **65**, 066211 (2002).

[Stö04a] H.-J. Stöckmann and R. Schäfer. Fidelity recovery in
          chaotic systems and the Debye-Waller factor. Preprint (2004).
          nlin.CD/0409021.

[Stö04b] H.-J. Stöckmann and R. Schäfer. Recovery of the fidelity amplitude
          for the gaussian ensembles. Preprint (2004). math-ph/0409058.

[Van03]   J. Vaníček and E. J. Heller. Semiclassical evaluation of quantum
          fidelity. *Phys. Rev. E* **68**, 056208 (2003).

[Ver85]   J. J. M. Verbaarschot, H. A. Weidenmüller, and M. R. Zirnbauer.
          Grassmann integration in stochastic quantum physics: The case of
          compound-nucleus scattering. *Phys. Rep.* **129**, 367 (1985).

[Vra02] M. Vraničar, M. Barth, G. Veble, M. Robnik, and H.-J. Stöckmann. 'Persistent currents' and eigenfunctions in microwave resonators with broken time reversal symmetry. *J. Phys. A* **35**, 4929 (2002).

[Žni04] M. Žnidarič. *Stability of quantum dynamics*. Dissertation University of Ljubljana (2004).

[Zha92] S. Zhang, B. H. Meier, and R. R. Ernst. Polarization echoes in NMR. *Phys. Rev. Lett.* **69**, 2149 (1992).

[Zim79] J. M. Ziman. *Models of Disorder*. University Press Cambridge (1979).

Acknowledgements

Lebenslauf

Name	Schäfer
Vorname	Rudi
Geburtsdatum	14.07.1975
Geburtsort	Lauterbach (Hessen)
Familienstand	ledig
Schulbesuch	Eichberg-Grundschule Lauterbach 1982-1986
	Förderstufe der Haupt- und Realschule Lauterbach 1986-1988
	Alexander-von-Humboldt Schule Lauterbach 1988-1995
	Allgemeine Hochschulreife am 12.06.1995
Studium der Physik	Philipps-Universität Marburg, 1995 - 2000
	- Vordiplom am 31.10.1997
	- Diplom am 28.09.2000
Berufstätigkeit	Wissenschaftliche Hilfskraft 2000 - 2001,
	Wissenschaftlicher Angestellter 2001 - 2004
	am Fachbereich Physik
	der Philipps-Universität Marburg